Internal Load Modelling of Tapered-Roller Main Bearings in Wind Turbines

PhD Thesis

James Stirling

Wind and Marine Energy Systems CDT

University of Strathclyde, Glasgow

July 16, 2023

This thesis is the result of the author's original research. It has been composed by the author and has not been previously submitted for examination which has led to the award of a degree.

Acknowledgements

I would like to express my sincere gratitude to my supervisors, Dr. Edward Hart and Dr. Abbas Mehrad Kazemi Amiri, for their continued support throughout this research project, with a special thank you to Dr. Hart for going above and beyond his duties as an advisor. I would also like to thank everyone at the Wind and Marine Energy Systems CDT for making this project possible.

Finally, I would like to extend a special thank you to my partner, Sharifa, for her unwavering love and support, ninkukunda munonga.

Abstract

The replacement of double-row spherical roller bearings with double-row tapered roller bearings as the main shaft support in wind turbines has been proposed as one of the solutions to the premature failures affecting the industry. In order to improve our scientific knowledge of tapered roller bearing loading in wind turbine main shafts, this thesis sets out to explore how these components may be modelled, how such models can be utilised to improve the understanding of their operational characteristics in relation to the inflow wind, and to compare their behaviour with that of spherical roller bearings. Novel drivetrain models with tapered roller main bearings are developed in this thesis with capabilities of evaluating internal component loading while accounting for variations in system stiffness at different operating points. The findings demonstrate that modelling the moment reaction behaviour of tapered-roller bearings is crucial for even simplistic representations, since moment loads at the wind turbine hub are key drivers of bearing displacement. The models developed here are used in an extensive analysis to determine characteristics and sensitivities regarding operational conditions experienced by double-row tapered roller bearings under realistic turbulent inflow conditions, while properly accounting for the system load-response behaviour, roller load distributions and impacts on bearing fatigue life ratings. The presence of "looped" loading structures and evidence of consistent roller edge-loading throughout normal operation is demonstrated, and load response was also found to be largely shared between the two roller rows, this contrasts strongly with the conditions known to hold for spherical-roller main bearings. High levels of fatigue life sensitivity to both operational and lubrication conditions are documented, and shear effects in the wind were found to

have opposite effects depending on the bearing type in use, with increased shear exponents drastically reducing the fatigue life rating of the tapered roller bearing. Crucially, this work demonstrates the uniqueness of load conditions experienced by tapered roller bearings in wind turbines, indicating that experience developed in more conventional rolling bearing applications should not be reapplied blindly without first determining its validity in this application space.

Contents

List of Figures

List of Tables

Chapter 1

Introduction

This thesis details the development of multiple wind turbine drivetrain models and their employment to advance the understanding of internal operational conditions of tapered roller main shaft bearings. There is a focus on computational efficiency when developing the models to allow for fast analyses of large numbers of complex and realistic hub loading data, offering the potential use case in operational analysis of wind turbines.

This chapter will briefly summarise the contents of this thesis, as well as outlining its principal contributions to the field and associated publications.

1.1 Thesis Overview

Chapter 1 provides a brief overview of the thesis and its contributions to knowledge.

Chapter 2 discusses the background and motivation for this work, outlining common turbine configurations and the role which the main bearing plays in supporting the rotor. Different types of roller bearing are then discussed before a detailed review of the existing literature in this area is presented. The most common main bearing modelling methods and the strengths and weaknesses of existing studies are discussed prior to a description of the problem statement. The specific research questions to be tackled are then posed.

Two quasistatic, 3-dimensional finite element models of a 3-point mounted drivetrain design are developed in Chapter 3 and compared to a pre-existing analytical model of a similar drivetrain set-up. The two finite element models have different moment reacting capabilities at the main bearing, one representative of a double row spherical roller bearing (DSRB) and one representative of a double row tapered roller bearing (DTRB). The fast acting analytical model is found to produce very similar results to the finite element model representative of a DSRB but proves to be ineffective in modelling DTRB behaviour. The analytical model is then developed further by the addition of torsional springs to include moment reaction capabilities, characteristic of DTRB behaviour. The stiffnesses of the torsional springs were estimated using the FE model and the load results were compared and found to be a good match. The existing analytical model representative of a DSRB and the new analytical model representative of a DTRB were then used to analyse a large number of load cases and the results were discussed. The DTRB analytical model was then used to visually inspect bearing loading.

An internal load distribution model for a DTRB is then derived in Chapter 4; designed to be computationally efficient and used in conjunction with the analytical model developed in the previous chapter. The internal load model has inherent non-linear stiffness characteristics. Since this model is used in conjunction with the aforementioned analytical model which has constant torsional stiffness assumptions, the effects of these assumptions are analysed and a method for incorporating varying stiffness capabilities into the analytical model is proposed. The load effects of constant torsional stiffness assumptions are then explored. A study is then undertaken to explore the wind field and rotor interactions which drive the displacement on internal bearing components. Finally, the model is used to explore load structures present during normal turbine operation and the findings are discussed.

The models are simulated operating in a large number of complex wind conditions with varying wind field characteristics, the results of which are analysed in Chapter 5. The effects of varying the inflow wind conditions on main bearing loading is explored in

two different ways; 1. The minimum, mean and maximum bearing unit loading and mean and maximum roller loading are analysed as wind speed, turbulence intensity and shear exponent is varied. 2. A fatigue life sensitivity study is completed using the model to assess impacts from operational temperatures, lubricant type, turbulence intensity, wind shear exponent and mean wind speeds. The results of the analyses are then discussed.

Chapter 6 summarises the results of the thesis, draws conclusions and discusses future work with respect to wind turbine main bearing modelling in the context of DTRBs.

Figure 1.1 displays an info-graphic depicting the work completed in each of the analytical chapters and Table 1.1 outlines the similarities and key differences between the model developed here and other models presented in the literature.

1.2 Key contributions to knowledge

The key contributions to knowledge generated by this research are:

- The development of novel drivetrain models representative of double-row tapered roller bearings supporting the main shaft in wind turbines. These models can determine load responses at the roller level within the bearing, while also accounting for variations in system stiffness at different operating points.
- Extensive analysis of representative operational conditions experienced by tapered roller main bearings under realistic turbulent inflow conditions. This includes system load characteristics, roller load distributions and variations over time, as well as impacts on the bearing fatigue rating life (including effects from loads, grease selection, contamination levels and bearing temperature).
- Comparative analysis with similar results in the literature for main shafts supported by spherical roller bearings. Thesis results conclusively demonstrate that load behaviour and wind-load relationships for tapered roller bearings are fundamentally different to those reported for spherical roller bearings.

Table 1.1: Comparison of the model developed in this thesis with model types available in the literature.

Feature	**Presented Model**	**Analytical Models**	**Multi-Body Models**	**FEM Models**
Computation time	low	very low	low-medium	high-very high
Cross-Coupled Stiffness	yes	no	yes	yes
Internal Loading	yes	no	yes	yes
Contact stresses	with extension	no	yes	yes
Integration to other applications	yes	yes	no	impractical
Open Access	yes	yes	no	no

1.3 Publications

Kenworthy, J., Hart, E., Stirling, J. Stock, A., Keller, J., Guo, Y., Brasseur, J. and Evans, R.: Wind turbine main bearing rating-lives as determined by IEC 61400-1:2019 and ISO 281:2007. Paper submitted to Wiley Wind Energy and currently under review. J.Stirling developed part of the code utilised to generate the findings in the paper.

Stirling, J., Hart, E., and Kazemi Amiri, A.: Constructing fast and representative analytical models of wind turbine main bearings, Wind Energ. Sci., 6, 1531, https://doi.org/10.5194/wes-6-15-2021, 2021.
J. Stirling performed the analysis and was the main author. The work presented in this paper is expanded in Chapter 3.

Hart, E., Clarke, B., Nicholas, G., Kazemi Amiri, A., Stirling, J., Carroll, J., Dwyer-Joyce, R., McDonald, A., and Long, H.: A review of wind turbine main bearings: design, operation, modelling, damage mechanisms and fault detection, Wind Energ. Sci., 5, 105124, https://doi.org/10.5194/wes-5-105-2020, 2020.
J. Stirling reviewed literature focusing on modelling methods of wind turbine main bearings. A summary of the literature review conclusions and prominent findings is included in the paper and the full literature review is presented here in Chapter 2.

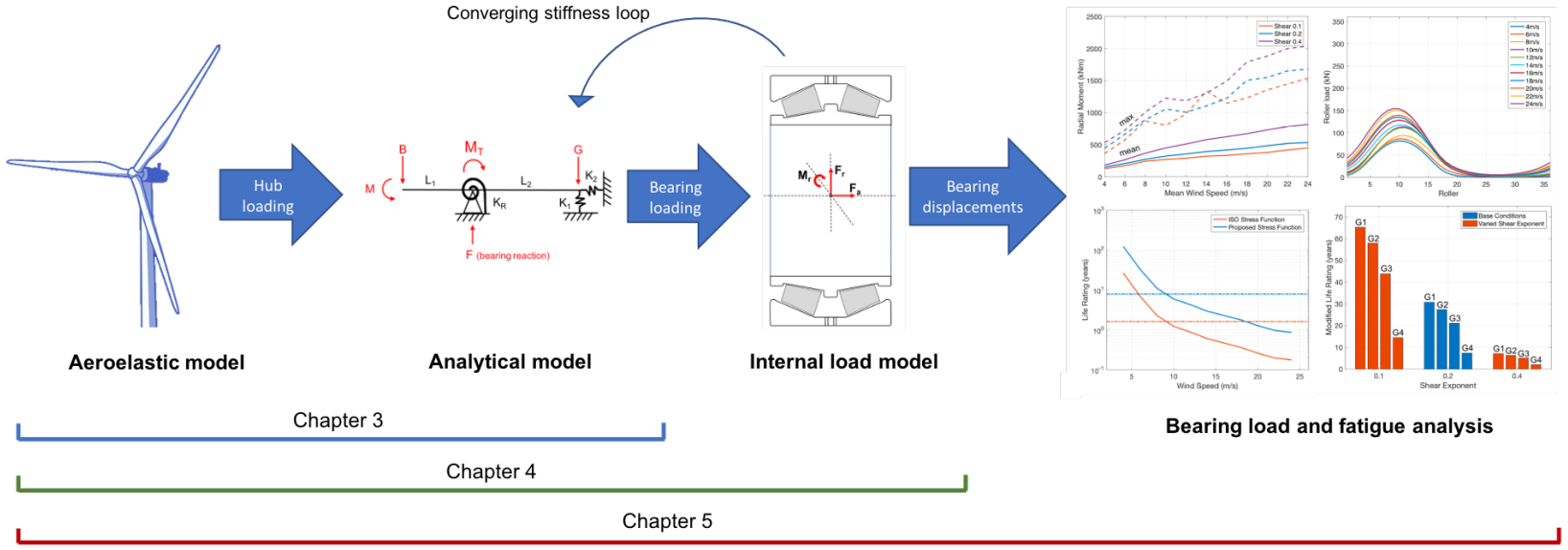

Figure 1.1: Caption in landscape to a figure in landscape.

Chapter 2

Background, Motivation and Problem Statement

The current climate crisis will require immense international efforts to prevent the average global temperatures from rising any further. This was echoed in the actions of world leaders in 2015 when they signed the Paris Agreement, promising to make an attempt to mitigate greenhouse gas emissions and help combat global warming. The world's current reliance on coal, oil and gas for electricity generation contributes to a significant proportion of total carbon emissions and must be drastically reduced and replaced with forms of 'green' and renewable energy in the hope to create a sustainable society.

The transition from fossil fuels to renewable energy sources is already well underway with renewable energy setting a new record for growth in 2020 despite the COVID-19 pandemic [55]. Similar to renewable energy as a whole, the wind energy market continues to grow at rapids rates and yearly installed capacity records were broken in 2020. A record year for onshore installations in both the United States and China helped push global new installations past 90GW with 86.9GW of onshore and 6.1GW of new offshore wind capacity being installed [46]. This record year for wind energy growth brings the total installed capacity to 743GW, growing the global operational wind fleet by 14% compared to the previous year [46].

While onshore remains a significant majority of new installed wind, the large land area required for wind farms and the increasing demand for wind energy has resulted in large competition for land use. In some countries, such as the United Kingdom (UK), development efforts have moved offshore where high energy wind conditions and vast available space for construction can be found [8]. As new offshore wind farms and turbines continue to grow in size and move further offshore, the cost of generation continues to drop - with the latest round in the UK's contract for difference auctions seeing record low strike prices of £39.65/MWh [19]; down from £57.50/MWh in round two and £114.39/MWh in round one.

Greater serviceability and robustness demands associated with offshore wind farms combined with the need for continuing reductions in energy generating costs increases the pressure on wind turbine original equipment manufacturers (OEMs) and wind farm operators (WFOs) to produce and maintain highly reliable machines. It is, thus, essential for further innovative wind turbine development to both reduce the cost of electricity production and improve the reliability of components.

2.1 Wind Turbines

Humans have recognised and harnessed the energy in the wind for thousands of years. Wind energy was used to propel boats millennia ago and then to mill grains and pump water some several centuries ago. It was not until fairly recently, in the past few decades, that technology was developed to transform the energy in the wind to electrical energy. Modern wind turbines operate in similar ways to the windmills and water pumps, transferring the kinetic energy of the wind into rotational energy in a shaft.

Wind turbine technology has now standardised and predominantly consists of horizontal axis machines with a three-bladed rotor [10], displayed in Figure 2.1. The operational method of wind turbines has tended towards variable speed, pitch regulated machines. Variable speed machines must be decoupled from the grid with power electronics but provide greater aerodynamic efficiencies throughout the operational range of the turbine

Figure 2.1: A typical modern 3 bladed wind turbine

[27]. The turbine operates in variable speed mode when the oncoming wind velocity is below rated power levels to track the maximum attainable power from the wind. The blade angles will remain fixed throughout this operational region until wind speeds surpass the rated value. The blades are then pitched when wind speeds are such that rated power is achieved, this reduces the aerodynamic efficiency and prevents overpowering and overloading the machine.

2.2 Wind Turbine Drivetrains

A wind turbine drivetrain converts mechanical to electrical power and transmits the non-torque rotor loads to the bedplate and tower [50]. Drivetrain designs have not yet converged to an optimal configuration and many manufacturers have chosen to continue developing their preferred layouts based on factors which align with company goals. Drivetrain designs have great influence on the future success of turbines and the most prominent variation in design is which gearbox, if any, is utilised [12]. Turbine OEMs are typically focused on driving down the capital costs associated with the drivetrain which has historically lead to a majority of onshore turbines utilising doubly fed induction

generators and high speed gearboxes [52]. However, gearboxes exhibit relatively large failure rates [65] and many OEMs have made the switch to more expensive direct drive or medium speed gearbox configurations for their larger offshore turbines, reducing warranty and O&M costs for the end user [12]. The current trend in the offshore market is the compacting of nacelles and mechanical integration of drivetrain components [50]. Lower failure rates make turbines more desirable and reducing nacelle mass decreases the cost and strength requirements of the tower and foundations. This is especially true offshore where site access restrictions and harsher environments can result in high capital and repair costs. While turbines can be distinguished by their choice of geared or direct drive drivetrains, variations of layout also exist within these two categories.

2.2.1 Geared drivetrains

Geared drivetrains can be categorised based on the rotor support and main bearing configuration. The most common geared turbine layouts are three point suspension and four point suspension systems which refer to turbines with either a single main bearing (SMB) or double main bearing (DMB) configuration, respectively [20]. Both of these configurations use a cantilevered main shaft to transmit the driving torque from the rotor to the gearbox and transfer non-torque loads to the nacelle structure [10]. The cantilevered main shaft in these designs are subject to significant moments arising from the aerodynamic loads on the blades and large fluctuating moments incurred by the weight of the rotor as it revolves [10]. The main shaft in the SMB system is supported at the rotor end by the main bearing and at the gearbox end by two gearbox trunnions, resulting in a total of three mounting points of support. The shaft is supported at the upwind end of the gearbox by an integrated main bearing which also acts as the planetary carrier bearing [21]. The SMB configurations are sensitive to non-torque loads and have been utilised in commercial wind turbines by Vestas, GE, Siemens and Nordex with rated powers between 1.5 and 3MW [20]. An image of the SMB layout is displayed in Figure 2.2a).

The DMB configuration includes a second main shaft bearing with the intent of isolating

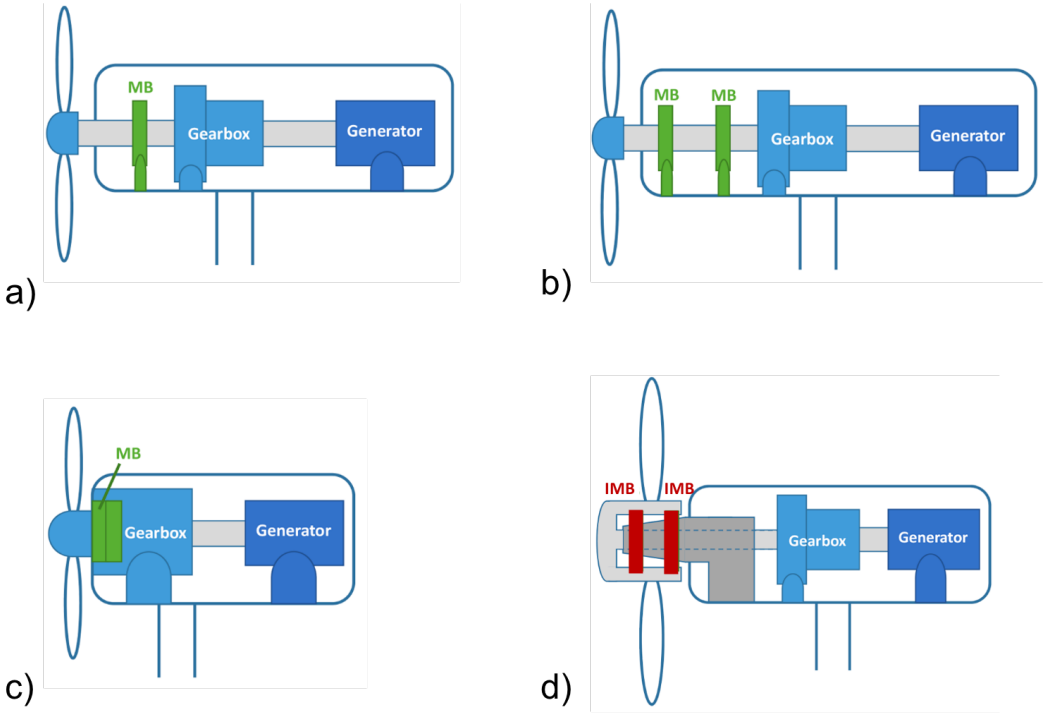

Figure 2.2: Depictions of the existing drivetrain layouts for geared turbines. In alphabetical order these are single main bearing, double main bearing, gearbox-integrated main bearing and inverted main bearing design. MB denotes a conventional main bearing with a fixed outer race and rotating inner race, IMB denotes an inverted main bearing with a fixed inner race and rotating outer race. [30]

non-torque loads from being transmitted to the gearbox [20]. Non-torque loads develop from the rotors interaction with gravity and the wind field and have been shown to have significant effects on gearbox reliability in [20]. The second main-bearing acts to shield the gearbox from such loading but inadvertently increases the sensitivity to misalignment and increases the mass of the nacelle which is associated with higher capital costs. The rotor-end main bearing is typically placed as close to the hub as possible to reduce the cantilever length and thus minimise the moment load caused by the rotor mass [10]. Either the upwind or downwind main bearing can be assigned as the locating bearing which is axially fixed and expected to carry all of the axial and moment loads, the other bearing must be assigned as a floating bearing which is not axially fixed and will share radial loads [67]. The use of two axially fixed main bearings are avoided to prevent added stresses caused when the shaft expands and contracts

with heat. The DMB configuration has been implemented in commercial wind turbines by Vestas, GE and Gamesa for turbines rated between 2 and 2.5MW [20]. An image of the DMB layout is displayed in Figure 2.2b).

The selection between one or two MBs is a critical design choice which has a direct effect on total nacelle mass through the influence on sizing of other components. As the nacelle mass impacts the dynamic and structural requirements of the tower and foundation system, the resultant effect on nacelle component size and turbine dynamic and structural requirements leads to the selection of one or two MBs having a great effect on the overall cost of a wind turbine [20]. The results of the analysis in [20] give a good first order estimate of component sizing and showed that a three-point suspension drivetrain, on average, reduced the nacelle mass by 16.7% and reduced the capital cost by 3.5%.

Other geared drivetrain designs also exist such as medium-speed systems, inverted bearing systems and integrated systems. Medium speed drivetrains remove the high speed gearbox stage without the need to include expensive rare earth magnets [12] and the integration of the main bearings into the gearbox removes the need for an extended main shaft, reducing nacelle mass and footprint. Vestas have developed and implemented medium-speed drivetrains in many of their larger offshore turbines including the V164 and V236 ranges spanning from 9.5MW to 15MW. They have also implemented this drivetrain design in their commercial 5.6MW onshore turbines. All the rotor loads in the integrated design enter the gearbox due to the main bearings direct integration which can lead to early failures for downstream components [67]. An image of the medium stage integrated drivetrain layout is displayed in Figure 2.2c).

Inverted bearing designs are another commercially available geared drivetrain design. In this configuration the bed plate is extended through the hub of the rotor creating a stationary main shaft. The bearings are inverted and, in two bearing systems, one is placed on the upwind and one on the downwind side of the hub to help eliminate rotor overhanging moments. The stationary main shaft acts as a structural component and elastic shaft couplings mean all non-torque loads are transmitted through the main

bearings to the bedplate and tower, isolating the gearbox and generator from them [6]. Alstom used this configuration in a range of their turbines including a 3MW size and claimed to have experimentally shown measured non-torque loads in their drivetrain design are two orders of magnitude lower than the rated torque and that failure rates are an order of magnitude lower than in other manufacturers [6, 21]. Inverting the main bearings has also become a popular trend for direct drive designs. An image of the inverted MB drivetrain design is displayed in Figure 2.2d).

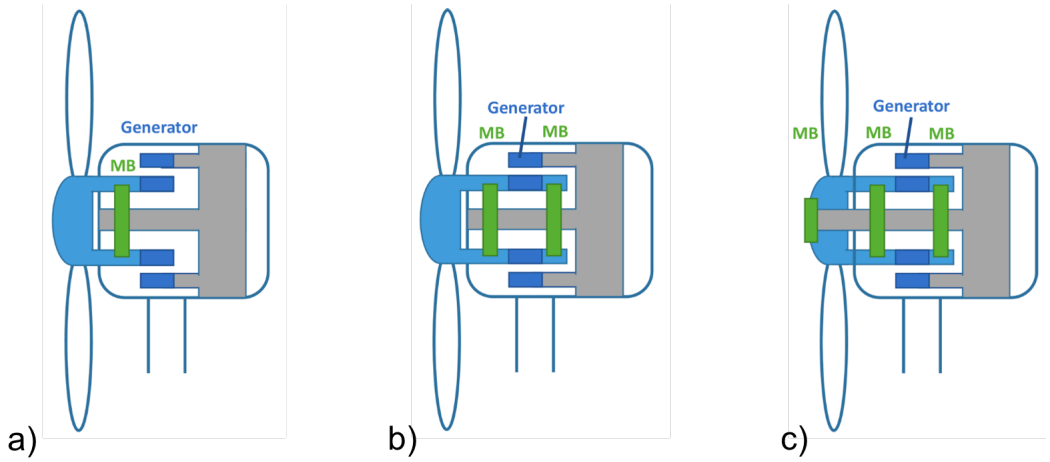

Figure 2.3: Depictions of some existing drivetrain layouts for direct drive systems. In alphabetical order these are single main bearing, double main bearing, and triple main bearing designs. [30]

2.2.2 Direct Drive

The main shaft in direct drive systems connects the hub directly to the rotor of the generator. A number of modern direct drive systems use the "floating" drivetrain configuration where the hollow main shaft is mounted on a fixed support shaft using one or more inverted main bearings [49]. GE, having acquired Alstom in 2014, use this configuration for all their larger offshore turbines, including the Haliade-X rated at 12MW or 14MW. Direct drive configurations typically use single, double or triple main bearing configurations with the generator rotor downwind of the hub rotor. Example layouts of such systems are displayed in Figure 2.3. However, a number of new conceptual de-

signs situate the generator upwind of the rotor and positioned freely from the structural components of the rotor and nacelle [64]. This would allow for generator replacement without the need for rotor removal, saving considerable time and maintenance costs. Main bearings within direct drive systems must also act as generator bearings and have the additional task of maintaining minimum air-gap clearances along with supporting the weight of the turbine rotor, generator rotor and hub loads [17, 63].

2.3 Rolling element bearings

All commercial wind turbines, regardless of drivetrain configuration, use rolling element bearings for the support of the main shaft due to their large load-supporting capabilities. Rolling element bearings on wind turbine main shafts have two important roles:

- Translating the mechanical torque from the rotor to the gearbox (if present) and generator.
- Structurally supporting the entirety of the weight of the turbine rotor, hub and main shaft while enduring significant and stochastic non-torque loads operating under slow rotational speeds (normally less than 30 revolutions per minute) [67]. In the case of direct drive machines, this extends to maintaining generator air gaps of millimeters in height for several meters in diameter [4].

Due to the complex and extreme nature of main bearing operational environments, turbine manufacturers have used a variety of different bearings in a variety of different configurations as outlined above to try and achieve the optimal design. Wind turbine OEMs typically employ one of (or a combination of) the following rolling element bearings as the main bearing(s): spherical roller bearing (SRB), tapered roller bearing (TRB) and cylindrical roller bearing (CRB).

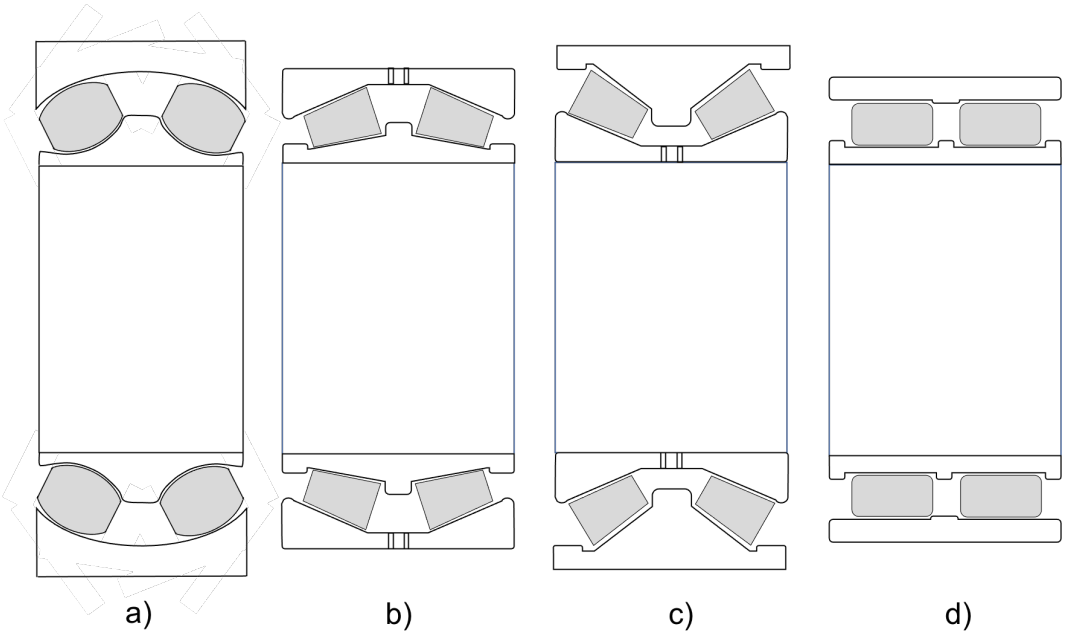

Figure 2.4: Depictions of double row roller bearing types. In alphabetical order these are double row spherical roller bearing (DSRB), double inner tapered roller bearing (DITRB), double outer tapered roller bearing (DOTRB) and double row cylindrical roller bearing (DCRB).

2.3.1 Spherical Roller Bearings

SRBs lend their name from the outer races having constant radii, representing a portion of a sphere. The rollers tend to be barrel shaped and conform closely to the curvature of the races, providing high radial load carrying capacity and the ability for self-aligning [26]. Rollers are usually crowned to reduce high stress edge loading from occurring. Double row spherical roller bearings (DSRB) increase the radial load capacity and also provide some thrust load capabilities but cannot support moment loading. An example DSRB layout is displayed in Figure 2.4. The close conformity of roller and raceways increases the friction of SRBs compared to CRBs and can cause sliding to occur between the roller and raceway contacts. DSRBs can have a variety of contact angles but tend to be shallower than that seen by TRBs.

Grease lubricated DSRBs are commonly used in SMB geared drivetrain systems and normal operation is causing them to typically fail in less than 10 years, incurring high

costs to operators [59, 70]. Common failures in this set up are micropitting, edge loading or cage damage which can subsequently contaminate the grease lubricant and lead to the damage of other components through surface fatigue and wear [11, 70]. At least two factors generally contribute to these premature failures; high thrust loads and inadequate lubrication [62, 79]. The slow rotational speeds of wind turbine main shafts are not ideal for adequate lubricant film formation and film thickness can be insufficient for the separation of roller and contact surfaces leading to wear [62]. The failures are extremely difficult to prevent as they are inherent in the design of the components, but increasing the quantity and frequency of lubrication and frequently purging the lubricant system may aid in reducing failure occurrences as suggested in [70].

The common method to determine if thrust loads will lead to premature DSRB failure is to determine the thrust-to-load ratio. Ratios of between 0.15 and 0.35 are generally considered as acceptable [3, 11, 59, 62]. However, various studies have displayed that DSRBs in SMB drivetrain configurations experience mean thrust-to-radial load ratios outwith this acceptable range [3, 11, 29], some suggesting values of up to 0.6 [37]. Loading the DSRBs beyond acceptable levels causes large axial displacements of the races and results in unloaded upwind rows leaving the downwind row to support the total load [28, 37]. Larger axial displacements also increase the risk of roller sliding and poor lubrication film thickness, exacerbating the problems which lead to micropitting [59]. The authors in [70] and [59] suggest surface finishing the contact surfaces to reduce asperities or coating them in a diamond-like coating to help reduce wear from sliding or poor lubricant film thicknesses. Alternatively, DSRBs could be replaced with DTRBs to improve thrust support capabilities which could not only improve the main bearing lifetime but also reduce the thrust loading reaching the gearbox by up to 65%, subsequently increasing potential gearbox lifetime [11, 70].

2.3.2 Tapered Roller Bearings

TRBs are different to other rolling bearings in that their inner and outer races have different contact angles and the rollers are tapered such that the roller diameters are

different at each end. This configuration allows TRBs to support large radial, thrust and moment loading, where the contact angle can be increased to account for greater thrust. Like other rolling element bearings, the rollers and raceways in TRBs can be crowned to reduce high stress loading at the roller edges. TRBs are separable due to the contact angle difference of the races and tend to be mounted in pairs along a shaft with one bearing being adjusted to the other [26]. Likewise, TRBs can be grouped together with two or more rows to increase the radial load carrying capabilities and reduce any axial adjustment problems due to being mounted at a distance. TRBs can also be manufactured or installed with preload which increases the number of rollers under load around the bearing circumference, reducing the stresses on any one roller. The drawbacks of the TRB geometry is that they are very sensitive to misalignment which can result in large edge loading of rollers. Double row tapered roller bearings (DTRB) can be arranged such that the two inner raceways are one piece of material, called a double inner tapered roller bearing (DITRB) or double cone assembly, or arranged such that the two outer races are made from one block of material, called a double outer tapered roller bearing (DOTRB) or double cup assembly. The differences between these two bearing layouts are displayed in Figure 2.4.

The inclusion of preloaded DTRBs can improve the drivetrain performance by helping ensure system rigidity, cope with high thrust-to-radial load ratios and ensuring the load is shared between the rows [11, 62]. Steep contact angles can provide the DTRBs with large rotational stiffnesses to counteract the overhanging moment and other non-torque loads from the hub. DTRBs have a greater sensitivity to misalignment than DSRBs but have more tolerance than TRBs spaced apart [62]. TRBs are widely used to support the main shaft in direct drive turbines as well as being employed in DMB systems as either two TRBs or a DTRB and CRB pair [30]. Recent SMB designs have now replaced DSRBs with DTRBs to improve drivetrain reliability and industry trends show turbine OEMs are changing from DSRBs to DTRBs as turbines scale. Replacing the DSRB with a DTRB reduces wear and load/deflection transmission to the gearbox [11].

2.3.3 Cylindrical Roller Bearings

CRBs consist of cylindrical rollers arranged with a contact angle of 0 (perpendicular to the rotational shaft), leading to extremely low friction torque and a high radial load carrying capacity [26]. They are typically axially unconstrained, hence commonly employed as the non-locating main bearing in DMB drivetrain systems. Like the other rolling element bearings, CRBs can be grouped together in rows to increase the radial load carrying capacity and the rollers can be crowned to prevent edge loading. The crowning of rollers also improves the self-aligning capabilities of the bearing, leading to slight protection against the effects of misalignment [26]. As CRBs cannot support axial loads they can only be used as non-locating bearings and as such will be typically only be found as a main bearing in DMB configuration wind turbine drivetrains. An example double row cylindrical roller bearing (DCRB) is displayed in Figure 2.4.

2.3.4 Roller Profiles

As alluded to in the previous sections, roller profiles can be crowned to reduce high contact stresses at roller edges. Roller crowning essentially introduces curvature to the edges of roller profiles in an attempt to combat stress peak phenomena that occurs when surfaces of finite length make contact with surfaces of greater length. In order to understand this behaviour, one must consider the ideal and realistic contact between roller and raceway. The hypothetical contact between an unloaded tapered roller bearing and raceway is a line contact with zero width. In ideal line contacts, where the roller and raceway are the same length, the contact area expands to a rectangle under load, and the compressive stress distribution remains equal across the length of the contact area. However, when a tapered roller contacts a raceway of greater length, material tension occurs in the raceway due to displacement at the roller edges. This results in a more elliptical contact area and, hence, greater compressive stresses at the roller edges where the contact area has reduced but load magnitude remains constant [26]. Figure 2.5 shows the stress peaks at the edge of a straight profiled roller under load.

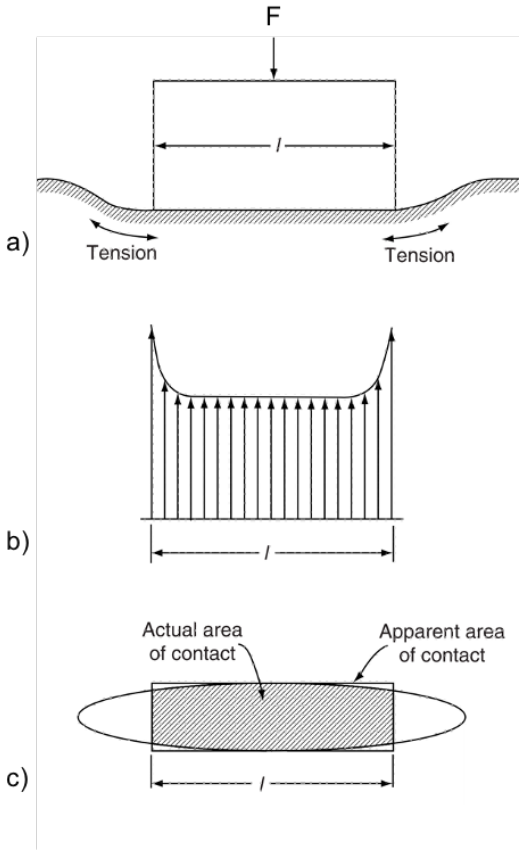

Figure 2.5: a) line contact of straight profiled roller contacting a surface of infinite length. b) roller-raceway compressive stress distribution from contact in a). c) contact ellipse and actual area of contact. Images modified from [26].

Crowning of rollers changes the contact relationship and reduces the edge loading of rollers, although typically results in higher stresses at the roller centre. Different levels and types of crowning exist and their benefits and drawbacks are discussed in [26]. The contact stiffness between roller and raceway is non-linear and thus, contact pressure distributions and stress concentration locations are non-linearly dependant on the roller load [74]. Optimal crowning profiles therefore vary with the load on the roller and the crown must be ideally designed for only one condition of loading [26, 74].

Complex and intricate mathematical, numerical and FE models have been developed to determine surface stress distributions for rollers and raceways with varying degrees of crowning [33, 41, 48, 68, 74, 80] and to optimise roller profiles for specific applica-

tions [66, 73]. It has been found that logarithmic profiles can produce fairly uniform stress distributions over a wide range of loading and soften the significant edge stresses produced by other profiles [26, 48]. A Single contact stress calculation requires digital computation, and considering that a roller and raceway contact area will require multiple contact stress solutions, and roller bearings have a considerable number of rollers, contact stress relationships for roller bearings can quickly become computationally intensive.

2.4 Other bearing types proposed for wind turbine main bearings

Novel main bearing design solutions have also been proposed and are in very early stages of development. The use of an asymmetric spherical roller bearing is proposed in [47] to improve the axial load capacities and limit thrust loads from impacting downstream components. Finite element modelling also indicated increased fatigue life ratings for the asymmetric design. Modular plain bearings are presented in [56, 57, 58] which have conical sliding surfaces connected to the housing via doubly flexible supports. These flexible supports help maintain bearing alignment and prevent edge loading. The modular design also provides maintenance advantages, allowing for segments to be individually replaced uptower.

2.5 Literature review of main bearing research and findings

Having introduced the relevant background material for this work above, the following section will review findings in the literature specifically relating to main bearings in wind turbines and explore existing bearing models. Section 2.5.1 collates relevant literature that involves main bearing reliability and failure mechanism studies. Section 2.5.2 discusses literature that analyses main bearing configuration and operational loads and

Section 2.5.3 discusses the literature where detailed main bearing models are presented. Section 2.5.4 then discusses bearing models in the literature outwith the wind industry and Section 2.5.5 discusses the common methods for modelling wind turbine main bearings.

2.5.1 Main bearing failures

Failure data from 77 600kW wind turbines from 27 different wind farms was analysed in [1]. The study included failure data for the main bearing (in this case DSRB) and showed that the bearing exhibits a random failure pattern, concluding there are no optimum inspection intervals and costs for a successful preventative maintenance strategy. The probability density function plot of main bearing failures shows that most failures will occur before 1300 days or approx 3.5years. The results also show that main bearing reliability falls from 0.93 in the first year to around 0.53 in the 7th year of operation and falls further to 0.13 after the 20 year life-cycle. The study also found that the lower limit of this calculation saw the reliability fall from 0.86 in the first year to 0 after the 15th year of operation [1].

Kotzalas and Doll provide an overview of the tribological challenges that limit the reliability of double row spherical roller bearings in use as the main shaft bearing of three-point suspension drivetrain systems in [45]. They discuss how main bearings are not predominantly failing by rolling contact fatigue but by micropitting wear initiated by the combination of sliding and inadequate lubrication. The radial and thrust forces experienced by main bearings in the three-point suspension configurations lead to the entirety of the load being supported by the downwind race, increasing the number of rollers loaded in this race. This, in combination with the slow rotational speeds, results in more stress cycles, higher loads and poorer lubrication of the rollers and raceways, increasing the risk of micropitting. The response seen in industry to correct this problem was to retrofit SRBs with higher fatigue load ratings. Higher fatigue load rated bearings however, tend to have longer rollers which would exacerbate the problem

due to even greater Heathcoat slip [1]. The authors instead suggest that preloaded tapered roller bearings could be used in place of the SRB to reduce sliding and the likelihood of micropitting. In applications where an SRB must be used, they advise engineering the surfaces of the rolling elements and raceways to reduce asperities.

A report detailing the findings, outcomes and recommendations of the Wind Turbine Drivetrain Reliability Collaborative Workshop in 2016 is presented in [42]. Main bearing failures were determined to be a critical issue within industry due to the frequency of failures occurring prematurely to design life and the associated cost of replacement. It was reported that main bearings are predominantly failing with failure modes that are not well-understood or accounted for in turbine design standards. The design standards are geared towards preventing rolling contact fatigue failures but do not address common failure modes where failures initiate as micropitting, adhesive wear or false brinelling which have unknown root causes. It is thought that these failures are initiated by sliding contact of the rollers and raceways due to inadequate bearing lubrication. The recommendation from the workshop to tackle main bearing failures was for a significant research and development push to investigate and generate an understanding of the operational conditions and bearing loads which could be leading to the off-design failure modes. This task would involve, but not be limited to, conducting analyses to determine root causes, developing tests that can represent contact conditions and lubrication quality, and creating drivetrain models to improve the understanding of bearing operational conditions which lead to the initiation of damage.

A method to consider the importance of misalignment on the load distribution in single tapered roller bearings is presented in [2] and the numerical results indicate that the load distribution is significantly effected from small levels of misalignment, reducing the bearings rated life. Life reduction caused by misalignment is considerably worse for uncrowned rollers and raceways. A failure analysis of a tapered roller bearing is presented in [24] and the authors conclude that failure was predominantly due to misalignment

[1] Heathcoat slip is experienced by all spherical roller bearings due to the geometry resulting in different surface velocities at different radii of the roller. Heathcoat slip alone will not cause micropitting. (Heathcote slip plus poor lubrication will)

which caused high stress edge loading on the rollers. They state that crowning can help accommodate minor bearing misalignment but will not prevent damage when the bearing is subject to considerable misalignment.

2.5.2 Drivetrain and main bearing load modelling

Hart et al. investigate the relationship between main bearing loading and wind characteristics for a range of geared drivetrain configurations in [29] using the two-step decoupled method[2]. Realistic 3-dimensional turbulent wind fields are generated and then a global load analysis simulation is performed in Bladed software. The hub loads are then extracted and used as inputs to three decoupled simple analytical drivetrain models where bearings are modelled as simple supports. The results showed that three-point mount systems have the largest axial-to-radial load ratios and are the most sensitive to wind field conditions. The four-point mount systems were shown to have increased radial loading with high sensitivities to wind shear. The results of this work displayed a strong link between wind field characteristics and main bearing loading and between bearing loading and drivetrain configuration.

In [76] the MB is modelled within an overall numerical model of the drivetrain using SIMPACK software. The drivetrain is a four-point mounting system for a 10MW offshore turbine and the model consists of both rigid and flexible bodies, with bearings modelled as force elements with linear force-deflection relationships. The study uses a two-step decoupled analysis approach where the global response is first determined using an aero-hydro-servo-elastic software SIMA. Hub loads and nacelle motions are then extracted and input to a detailed drivetrain model where high fidelity FE models of the critical components are developed in ANSYS before modal reduction is used to minimise degrees of freedom for reduced FE bodies in the system. The paper sought to determine 20-year drivetrain fatigue damage and found that the highest fatigue damage

[2]The two-step decoupled method refers to the process of performing an analysis using two completely decoupled models. In terms of drivetrain analysis, this usually involves using an aero-elastic code to model the full turbine system under operation in 3-dimensional simulated wind fields. The hub loading is determined and extracted from this first simulation and then injected into a separate, more detailed model of the drivetrain as an input to determine the loads on drivetrain components.

is experienced by the upwind MB.

Wang et al. determine MB loading in a four-point suspension drivetrain for the case where a flexible bedplate is included in modelling in [75]. The study uses a decoupled analysis approach to compare drivetrain loads on a 10MW spar type floating turbine and compare results depending on rigid or flexible modelling of the bedplate. SIMO-REFLEX software is utilised to simulate the global behaviour and determine aerodynamic loads and the dynamic response of the drivetrain before the dynamic loads are input to a separate multibody drivetrain model in SIMPACK. The drivetrain is represented by a single degree of freedom spring-damper system in SIMO and the main bearings are modelled by a linear diagonal stiffness matrix with off-diagonal terms equal to zero as cross-coupling was not considered. The study concludes that modelling flexibility in the bedplate leads to a slight reduction in loading and fatigue experienced by MBs when compared to the rigid case.

Guo et al. use field testing, a computational model and an analytical model in [21] to analyse Alstom's Pure Torque drivetrain system. The computational model was created in SAMCEF software which "incorporates an implicit nonlinear dynamic finite element approach with multibody system functionalities" [21]. Major turbine components such as the blades, hub, main shaft, gearbox, bedplate, tower and foundation were modelled with flexibilities of the structural components modelled as either non-linear beams or super elements. The Craig-Bampton condensation technique was used to improve the computational efficiency by decreasing the degrees of freedom of some components. However, main bearings remained as super elements and were modelled by nonlinear stiffness functions with radial and axial clearance, considering only the diagonal terms in the stiffness matrix. The reduced-order analytical model is derived by balancing the forces and moments of the system in each plane and then making a series of assumptions to reduce terms. The model provided an understanding of how non-torque loads affect the Pure Torque drivetrain. The field results, computational model and analytical model are compared under various situational evaluations including normal operation and extreme load cases and show good agreement throughout. The findings show that

almost all non-torque loads are diverted through the main bearings to the turbine structure and not transmitted through the downwind drivetrain components.

Sethuraman et al. seek to determine the dynamic drivetrain load effects of a direct drive system for a floating turbine rated 5MW in [60]. The direct drive machine consists of a two main bearing system using an upwind double row inner tapered roller bearing and a downwind cylindrical roller bearing to support the hub and permanent magnet radial flux generator rotors. The authors use the multibody simulation software HAWC2 to determine the aero-hydro-servo-elastic behaviour of the turbine and extract drivetrain loads before inputting them to a more detailed multibody drivetrain model in SIMPACK. The bearings were modelled as visco-elastic force elements and spring-damper elements, allowing the definitions of full stiffness matrices provided by the bearing manufacturer in the more detailed drivetrain model. The results were then compared with that of a similar land-based model over the turbines full normal operational points. The upwind TRB bearing sees an increase in mean and maximum axial loads in the floating turbine design. The tilting moment on the upwind bearing in the floating system is on average 7% greater than that of the mean and standard deviations on the land-based turbine and the maximum moment is as high as 22% greater. Minimal differences are seen in the radial loading of the two main bearings between the floating and land-based turbines.

Sethuraman et al. use an aero-elastic code to determine hub loads and then use a detailed multibody model of the drivetrain in SIMPACK to analyse three case studies of a three point mount 1.5MW turbine in [59]. Eleven sets of load cases were used for each case study which represent the turbine's normal operation and SIMPACK yielded time series loading of the main bearing for each case. The model was validated against field measurement and shown to have good correlation. The base model consisted of a 230/600 DSRB as the main bearing and a CRB as the integrated planet carrier bearing. The axial-to-radial load ratio, axial displacement and dynamic-load-rating-to-dynamic-equivalent-load ratio (C/P ratio) was determined for every load case and used comparatively with the three case study designs. A C/P ratio between 4 and 10

suggests high loads and reduced grease service life. The C/P ratio for the 230/600 DSRB remained between 4 and 10 across all the operating ranges and the axial-to-radial load ratio peaked at 0.47 at the rated speed and remained above 0.22 for the majority of the operational range. Axial displacement also peaked at rated speeds, remaining above 0.5mm and peaking at 1.78mm. The authors suggest that the large load ratio and axial displacement seen will likely cause excessive sliding of rollers. Case Study 1 involved using larger envelope bearings, Case Study 2 analysed a variation of internal radial clearances and Case Study 3 replaced the CRB planet carrier bearings with TRBs. The replacement of the 230/600 bearing with a 231/600 and 240/600 increased the C/P ratio outside the high load region and significantly reduced axial displacement across all load regions but the axial-to-radial load ratio did not improve. Axial displacements improved with tighter clearances but axial-to-radial load ratios did not improve. Replacing the CRBs with TRBs reduced DSRB raceway displacement by an average of 23% and the axial-to-radial load ratio by 40%.

Nejad et al. investigate the drivetrain load effects in a high-speed, four-point suspension, offshore wind turbine rated at 5MW when subjected to a blade-pitch fault condition and emergency shutdown in [51]. A two-step decoupled approach was used where aeroelastic simulations were first performed in HAWC2 to determine main shaft torque and non-torque loads then the loads were input to a detailed multibody simulation model of the gearbox in SIMPACK. The main focus of the study is on the gearbox loads but results are also presented for the two main bearings which are modelled by force elements and force-deflection relations. The results show that the there is a considerable torque reversal and a dramatic peak in the moment load on the main shaft. The dramatic peak in the main shaft moment results in a peak in the first main bearing radial load by approximately 1.5 times the mean value. The second main bearing is subject to significant axial forces during the shutdown procedure due to the changes in thrust force. The two main bearings were seen to be the most effected components during this analysis and the authors recommend such extreme loads be design drivers for main bearing life estimation due to the effect on fatigue life calculations. The authors also recommend inspection of bearings after these faults occur.

A specially instrumented General Electric (GE) turbine was installed at a National Renewable Energy Laboratory (NREL) site with the goal of increasing the understanding of operational conditions of main bearings and exploring the possible effects relating to their premature failures. The turbine was rated at 1.5MW and hosted a commercial DSRB main bearing fitted with a multitude of different sensors and lubricated with LGWM2 grease. 3 years of operational data have been collected and multiple analyses have been published. The relationship between the axial motion of the main bearing and the expected lubrication characteristics have been examined in [22] where the axial velocity of rollers was found to be negligible in comparison to their rolling speed, thus, they are expected not to influence the lubricant film thickness. Additional measurements related to the lubricant film were also analysed in [23] where the authors examined the characteristics of acoustic emissions and temperature of the main bearing, correlating readings with turbine operating conditions (wind speed, rotor speed, axial loads, active power). Acoustic emission characteristics were found to be uniformly low below the rated rotor speed and the highest when the turbine was operating at 14m/s (above rated) and under warmer conditions of over 25 degrees Celsius. Some acoustic emissions were expected to have sources from other turbine components. However, the majority of emissions were expected to be related to surface asperity contacts, resulting from the breakdown of the lubricant film separation layer.

2.5.3 Detailed wind turbine main bearing modelling

Sensor data from the same main bearing and wind turbine detailed in [23] was also used in [3] where main bearing loads and resulting roller-load-induced strain of the bearing were examined for evidence of cage slip. Bearing models were also created to predict roller loads and contact stresses. The measurement of roller load induced strain was used to determine actual ball pass frequencies of the outer race for two operating conditions. The measured ball pass frequencies were then compared to theoretically derived ball pass frequencies for pure rolling conditions to determine if the cage was slipping (measured would be lower speed than theoretical if so). This analysis could

only determine if the bearing cage was slipping but not if individual rollers were slipping. The measured bearing cage speed was found to be very closely aligned with the theoretical value and the authors conclude that no evidence of main bearing cage slipping was found in any of the measured conditions. Two models were created in the study to determine roller loads and contact stresses. Firstly, an analytical model of the drivetrain set up was created to statically determine axial and radial loads at the main bearing during typical rated conditions. Aero-servo-elastic simulations in OpenFAST were used to determine thrust, radial and moment loads at the hub for two operating conditions. These values were passed to the analytical drivetrain model and the bearing loads were determined. These loads were then fed into a second, more detailed Finite Element/contact mechanics model of the DSRB where the roller loads and contact stresses were determined. The Transmission3D software was used to create the detailed contact-mechanics bearing model. Detailed roller and raceway geometries and bearing clearances were included in the model along with the bearing housing. The bolt holes on the housing arms were constrained as the boundary condition. Bearing contacts and piece-wise clearance non-linearities were modelled with a hybrid of finite elements to predict far-field displacements and the displacements in the contact region were determined by a Green's function model [3]. Flexible joints were used to connect the bearing rings with the housing and main shaft. The detailed model determines the bearing contact relationships quasi-statically as the rollers move around the race. Two load cases were simulated for 10 time steps; above cut-in and rated speed bearing loads determined by the aeroelastic simulations and analytical drivetrain model were applied to the contact model. The model outputs roller loads, deflections, contact stresses and predicts stresses in the bearing rings and housing. The analytical model determined that the thrust and radial loads on the bearing resulted in an axial-to-radial load ratio of 0.46 at rated wind speed, much greater than the bearing's e rating of 0.3. The contact model analysis found that there are significant differences in the loading behaviour between the upwind and downwind rows of the DSRB, with the downwind row always supporting more load and subsequently having larger loading regions due to rotor thrust. At rated conditions all rollers in the downwind race and no rollers

in the upwind race were found to be loaded. The load was more reasonably shared amongst the rows at above cut-in speeds. The highest roller load recorded was 81kN which resulted in a maximum contact stress of 2GPa. The downwind row will consume its rating life much faster than the upwind row and will likely be the point of bearing failure.

Zheng et al. present a highly detailed quasi-static mathematical model of a DTRB used as a main bearing in a floating direct drive turbine in [81] and [82]. The model has five degrees of freedom (the inner ring was allowed to rotate freely as not to consider torque loads) and each roller is also modelled individually. The iterative Newton-Raphson method is used to find the bearing equilibrium utilising two main iterative loops; one for the radial and one for the axial displacement. The 3D elastic contact approach is then used to calculate the contact pressure distributions using the force and displacement values output from the newton-Raphson method. The bearing components were assumed to be made of homogenous material where only elastic deformation occurs in local contact areas. The bearing structural deformation was ignored and the rolling elements are distributed uniformly in space. The effects of forces from the cages and roller skewing were neglected and no pre-load is assumed. The model considers coulomb friction and crowned roller profiles where Hertzian theory is used to calculate the flange contact force at the large end of the roller, the roller slicing technique is also employed.

Displacement, roller forces and contact pressures are determined in [81] while the bearing is under constant radial load and a linearly increasing axial load. Findings show that loads on race 2 become increasingly larger than loads on race 1 as the axial load on the bearing is increased. The effects of misalignment are then studied under constant radial and axial loads for both crowned and flat roller types. They found that an increase in misalignment angle can significantly change the contact load distribution on the rollers where the load on the highest loaded rollers increased rapidly with misalignment angle. They also found that the effect of the roller profile was insignificant. The contact pressure was also determined for crowned and flat rollers with and without misalignment where downwind roller pressures were found to be larger for both types

of roller. Pressure concentration happens at the end of rollers so crowning therefore reduces peak contact pressures seen. Increased misalignment leads to sharp increases in peak contact pressure at the end of both types of rollers. The effects of friction were also considered and found to alter the contact pressure distributions of rollers.

The same model was employed by Zheng et al. in [82] where an oscillating factor representing a basic sinusoidal is used to modify the reference rating life equation from the relevant standard to calculate fatigue life rating of the bearing under oscillating loads. The oscillating load was used to represent waves affecting the floating structure and the simulations were carried out under constant rotational speed. The fatigue life ratings were calculated with varying misalignment angles and varying axial and radial clearances to represent preload while under constant axial and radial loads. Misalignment was shown to decrease life rating throughout all scenarios and a certain amount of axial preload was shown to increase bearing life - but too much can reduce the lifetime. Like in [81], the contact pressure distribution analysis showed that misalignment changes leads to higher localised pressures.

Kock et al. use the two-step decoupled method to determine main bearing load distributions of a 6MW four-point mounted system during the start-up operation in [44]. The drivetrain has an SRB as the upwind bearing and CRB as the downwind support. The paper discusses the simulation results of the CRB only. A multibody simulation is first used to determine global loads and then hub loads are injected to a detailed finite element model to determine the bearing load distribution, roller element load distribution and contact pressure. Three different roller modelling methods are used for each output; the roller elements are represented by one spring stiffness to determine bearing load distributions, the roller elements are represented as a number of spring stiffness using the slicing technique to determine load distributions along the roller length and 3-dimensional geometries of the roller elements are used to determine the pressure distribution. The inclusion of elastic surroundings, bearing clearance, rolling element profiles and hub loads is varied during the analysis to determine their effect on the results. The results showed the importance of modelling elastic surroundings as

they impacted load magnitudes and distributions, with an increased number of bearings under load and reduced maximum load values seen when more elastic bodies were included in simulations. The direction of load can affect the bearing load distribution due to the differences in stiffness around the circumference of the housing and higher loads result in more rolling elements in contact and higher element loads. A reduction in roller clearance is also shown to increase the number of elements loaded and reduce maximum element loading.

Hart uses a three-step decoupled approach in [28] to analyse time varying loads on a DSRB main bearing in a three-point mount system. The Bladed software is used for global loads and then a simplified analytical drivetrain model presented in [29] is used to determine bearing loads. The bearing loads from the analytical model are first studied and used to show that loop structures with large load and directional fluctuations over short periods of time are present throughout much of the operational loading. Methodologies are presented to identify and categorise these loop structures before a third model is derived to determine how these structures may be effecting the internal loading of the bearing. The third model is a detailed numerical model of a DSRB with capabilities of determining the distributed load around the bearing. The loop structures were found to exist in approximately 50% of the operational time centered around the 3Ω frequency and have considerable impacts on roller loading.

2.5.4 General bearing models

Houpert proposes an analytical TRB model in [35] and claims it can be integrated into FEA packages to allow quick predictions of bearing performance without the need for complex numerical calculations. The model assumes circular races, flat rollers (ignoring crowning, roller edge radii or special profiles) and a line contact between the rollers and raceways. This analytical approach solves for bearing forces in the axial, horizontal and vertical directions and tilting moments about the horizontal and vertical axes giving the model 5 degrees of freedom to allow for these displacements. The model considers

a full coupling between the forces and displacements and the slicing technique[3] is used to split roller-race contact areas into slices along the roller. A new stiffness relationship is also proposed to allow for the inclusion of roller diameter effects and then used to produce load results which are compared with Harris [26] and Eschmann [7] methods, showing small variations in results. Misalignment is also considered and shown not to contribute to the final roller load but cause a moment on each roller.

The load distribution between roller and raceway of a TRB is analysed in [33] when the rollers have a straight profile, circular crowned profile and logarithmic crowned profile. They assume a preset rectangular contact area and divide it into a number of elements using the influence coefficient method. A uniform pressure distribution is then assumed so that a set of linear algebraic equations containing the deformation and stress relationships can be derived and iteratively solved using the Newton-Raphson method. The model was compared to Palmgren's empirical formulas (presented in [26]) with straight roller profiles and results show that the maximum error between load distributions is 0.3% and between contact deformations is 6.6%. Load and contact deformation results for the different roller profiles were then compared using the numerical model where the load distributions remained similar but contact deformation deviated significantly between the profiles. The study concludes that while roller crowning affects contact deformation, and hence, contact pressures, it does not effect roller loads and that the Palmgren method could be used for crowned rollers approximately to reduce iterative time and improve analysis efficiency.

The contact stresses in a DTRB are determined using the FE method, an analytical model and experimental analysis in [48]. The FE model considered the inner raceway, outer raceway, rollers and hub and simulations were run assuming no rotation of the bearing. Lubrication and hydrodynamic effects were also neglected and mesh sizing was minimised until convergence of the results. The analytical model was based on Palmgren's method (presented in [26]) and treats the double row bearing as two one-

[3]The slicing technique involves slicing the roller into several laminae across its length to consider misalignment in contact problems. Each roller laminae contributes to the roller stiffness and is usually treated independently, having no contribution to load or deflections of neighbouring lamina [68][39]. The ISO standards state that a roller must be sliced into a minimum of 30 lamina [39].

row bearings. Once the load distribution was determined using the analytical method, the authors used the semi-cylindrical contact area approach to determine the normal contact stress. The experimental analysis utilised comparator pencils to measure the relative displacement between inner and outer raceways and pressure sensors were used to determine the contact stresses. The three analysis methods considered a radial load of 2kN and varied preloads of 300,400,500 and 600N; torque and axial loads were neglected. The results concluded that higher preloads increase the mechanical contact stiffness of the bearing and result in minimum displacements. The FE results also showed increased stress at the roller edges of the straight profiled roller. The FE model required extremely fine mesh sizes for result convergence, resulting in increased computational requirements, yet contact stresses are similar to those obtained by the analytical model.

The authors in [16] created a highly detailed 3D FE model of a DTRB to use machine learning techniques in an attempt to optimise preloading conditions for optimum bearing performance. As the bearing is symmetrical, the authors modelled only half of the bearing to reduce computational costs. This included the modelling of the tapered rollers, inner raceways, outer raceways and a hub to mount them on. The mesh size around the contact areas was refined until FE model results aligned with theoretical and experimental results. A segment-to-segment contact detection algorithm was then employed to reduce the error in calculating contact stresses using the smaller mesh density. The model consisted of 73,484 elements, 84,009 nodes and 3289 degrees of freedom and took approximately 200 hours to run a single simulation on a high powered machine. 8 high powered computers were used to simulate the 81 combinations of load possibilities for data mining. The authors found that the flexible discriminant analysis method produced the most accurate results and conclude that combining FEM and machine learning techniques can be used to successfully determine a TRB's operating conditions.

Xu et al. extend the mechanical model (analytical model) of a DTRB to analyse friction torque while considering misalignment, radial clearance and axial pre-load [78]. The

authors determine the total friction torque by summing the effects of elastic hysteresis, ElastoHydrodynamic Lubrication rolling friction, sliding friction at rib-roller end contact and the viscous drag friction caused by the lubricant across the two rows of rollers. The friction torque was analysed under fixed loads and varying rotational speeds and found to initially decrease with rotational speed until around 250rpm where it began to increase again as rotational speed increased. The friction torque was then determined for various cases of axial pre-load where the results displayed increased friction torque with increasing pre-load. The effects of radial clearance on the friction torque was also analysed and results showed a reduction in torque with increased clearance. Finally, the friction torque was analysed under various misalignment conditions where increased misalignment angles were shown to increase friction torque.

A new, faster method for analysing roller-raceway contact stresses of cylindrical roller bearings was presented in [68] where the authors propose a new slicing technique and load-deflection relationship. Existing load-deflection approximations are first compared before the authors create a simpler load-deflection relationship by curve-fitting one of the implicit expressions to eliminate the need for time-consuming iterations. Instead, the slicing technique was extended to consider the effect of each slice on neighbouring slices. Weighting factors where then introduced to consider the effect of a force in one slice on the deflection of another, creating a set of linear equations solved by Gaussian elimination procedure. The results of the new relationship were compared to that of a simplified FE model of a roller contacting a flat plate and showed good agreement but a slightly more barreled shape of the pressure distribution. The study found that the optimal roller profile depends on the load but also the thicknesses of the contacting bodies, meaning that half-space theory holds only partly in practical situations.

Tong and Hong develop a 5 degree of freedom numerical model of a TRB in [71] to analyse combined axial and radial loads under high rotational speeds. The model employs an integration technique instead of the slicing technique to determine displacements/loads along the rollers and raceways, considering flange contacts and centrifugal and gyroscopic effects. The Newton-Raphson method is used to solve the non-linear

equations and to determine bearing equilibriums, the roller coordinates are then translated to the global coordinate system to find bearing equilibrium and Newton-Raphson method is employed again to determine total bearing displacement. Bearing displacement and load effects were studied under varying rotational speeds and the results found that the axial displacement decreased and the radial and angular displacements increased with increasing rotational speeds. Increasing speeds also reduced the axial, radial and angular stiffness coefficients but increased the coupling stiffness. The study also found that increasing rotational speeds reduces contact forces between the roller and raceway but increases roller-flange contact forces. Tong and Hong then adapted the model in [72] to consider the effect of misalignment on contact pressure distribution and fatigue life rating. This time they use the slicing technique and consider a logarithmic roller profile. An iterative technique is used to solve the non-Hertzian contact pressures where a discretization technique is employed to divide the assumed contact area into smaller segments. Increasing the number of segments in the contact area improves the accuracy of results but requires more computational power. 2091 segments are used here to discretize both the inner and outer contact areas for each roller. Fatigue life is then calculated under axial and radial loads while the rotational speed is kept constant and the misalignment angle is varied. The results showed that small amounts of misalignment (angular displacement) leads to a substantial reduction in fatigue life regardless of the axial and radial load conditions. The model is used again in [73] to optimise roller profiles for maximum life rating.

2.5.5 Discussion of main bearing modelling methods

It is clear from the studies described above that the two-step decoupled model method is common for the analysis of drivetrain loading. The majority of analyses utilise standard aero-elastic codes certified for wind turbine design such as Bladed, FAST and HAWC2 to determine the global behaviour of the turbine in question. The global analysis software packages mainly focus on aerodynamic loads and the dynamic behaviour of structural components. Therefore, the drivetrain is typically represented as a sim-

ple one degree of freedom system, neglecting specific drivetrain components. The hub loads acquired from this global model are then extracted and injected into a separate, more detailed drivetrain model to study the effects of loading on drivetrain components. This approach is accepted in industry as drivetrain designs have classically had natural frequencies significantly higher than the external excitations on the turbine [54]. However, as turbines scale and their drivetrains increase in size, the natural frequencies of the drivetrain decreases. Thus, when analysing larger turbines, care must be taken to ensure their are no coupled dynamic effects between the drivetrain and other turbine components, which the decoupled modelling method would fail to capture.

The second models in the decoupled approach tend to be dynamic multibody models in SIMPACK; created by developing high fidelity finite element models of the components and then using a reduction technique to simplify them and reduce the number of degrees of freedom. Main bearings are modelled by force elements in these systems with linear stiffness matrices used to calculate the bearing deflections and natural frequencies. Other model types, although less frequent, are also used as the second model in the two-step decoupled method including simple analytical drivetrain representations as in [29] which allow fast analysis of significant numbers of load cases, and highly detailed finite element models as in [44] which can determine internal loading but requires significant computational power and time. The two-step method is very useful for determining bearing behaviours throughout large ranges of operational conditions when computationally efficient bearing models are utilised. However, these are limited to bearing unit loads in the case of analytical models or hidden behind paywalls in the case of multi-body simulation packages such as SIMPACK. The highly detailed finite element models remain too computationally expensive and cannot simulate large ranges of operational conditions, they are instead run under static conditions or a small number of time steps.

Hart extended this method to a three-step decoupled approach in [28], utilising a third model of a DSRB which could determine the bearings distributed loading throughout full time histories. Archeli et al. also extended this method to a three-step decoupled

approach in [3], using a detailed FE/contact mechanic model of a DSRB to determine roller loads on each row. A small number of time-steps (10) were simulated with the FE model due to model complexity. Zheng et al. present a detailed numerical model of a DTRB in [81] and [82] which similarly investigates internal loading. However, this model is complex and bearing behaviours are investigated under simplified, unrealistic load conditions. Therefore, to date, there is limited analyses in the literature which focuses on the characteristics of loading in a tapered roller main bearing which investigates internal load characteristics under realistic wind loading.

2.6 Problem Statement and Research Questions

Designing wind turbines is a complex and difficult task that requires an integrated design process to ensure proper functionality between all components. Various integrated models are therefore necessary in the design process where models can include all turbine components or all components within turbine sub-assemblies such as the drivetrain. The integration of models is a challenging task where the complexity and detail of individual components must be balanced with the modelling efficiency, computational expense and value of information gained from simulations. Related to this, a trend amongst OEMs and WFOs for developing wind turbine digital twin models has emerged in recent years where virtual versions of turbines are created for the purposes of ongoing life assessment of turbine components during the operational phase. Digital twin models are supplied with operational data and used to run behavioural and load studies under the real conditions seen by the turbine. There is also an increasing desire to monitor the condition of entire wind farms. As digital twin models and models for entire wind farm analysis are required to capture key parameters in near real time, the modelling of turbine components must remain simple to remain computationally inexpensive. There is therefore an increasing need for efficient simplified representations of turbine components that allow for load, design and life analyses while providing insight into operational conditions, ideally without requiring complex commercial software.

The above aspirations apply equally to the main bearing and other drivetrain components. However, significant uncertainty remains with regards to their true conditions and appropriate modelling, as laid out in the the literature review provided earlier. More specifically, DSRBs (which have typically been used to support the main shaft) are failing prematurely to their design life with failure modes not considered in the design standards. Their inherent geometry does not lend itself well in the use case of a main shaft bearing as rotor thrust loads are causing axial displacements of the bearing and slow operational speeds lead to insufficient lubrication of the contact surfaces. This results in the downwind row supporting the entire loads of the system, sliding of the overloaded rollers, and surface to surface contact of the rollers and raceway, ultimately leading to premature failure. A common solution put forward by wind turbine OEMs and bearing manufacturers alike is to replace these DSRBs with DTRBs, DITRBs to be precise. While significant efforts are currently being undertaken (in both industry and academia) to increase the understanding of how DSRBs are responding to the complex loading imparted by the rotors interaction with the wind, the potential effects of replacing DSRBs with DTRBs remains less explored. As previously discussed, there are limited analyses of DTRB load characteristics in the literature and a lack of open-sourced models which have the computational efficiency to explore internal loading behaviour throughout vast ranges of operational conditions. As DTRBs are being marketed as a potential solution to premature main bearing failures, there is a clear need to better understand how characteristics in the inflow wind field effect the load and life of DTRBs. One cannot assume that the relationships between the inflow wind field and DSRB load behaviours remains the same in the case of DTRBs due to the intrinsic differences in their geometry and load reaction capabilities. There is, therefore, a clear knowledge gap regarding key DTRB load drivers in the wind field, their impacts on fatigue life, and how DTRB behaviour compares to that of DSRBs.

Therefore, in the case of a double-row tapered main bearing, based on the previous discussion and the literature review of existing models and capabilities, there is clear value in the development of open-source tapered roller main bearing models with capabilities of efficiently analysing internal loading to aid in the study and understanding of the

operational loading of these components. Furthermore, real world conditions and effects, and their impacts on component life need to be better understood. Finally, there is additional value in comparative analyses between tapered roller bearing response and spherical roller bearing response in the context of supporting a wind turbine main shaft. In order to contribute to solving these outlined engineering research problems, this PhD sought to answer the following questions:

1) How may tapered-roller main bearings in wind turbines be modelled simply and efficiently while retaining key aspects of their load response, both moment and force reaction capabilities, and stiffness characteristics?

2) Applying such models, what may be concluded about the operating conditions of such components, their load drivers in turbulent wind fields, and their sensitivities in relation to fatigue life ratings?

3) How do load behaviours and sensitivities in tapered-roller main bearings compare to those of spherical-roller main bearings?

Chapter 3

Drivetrain load response using analytical models

As previously outlined in Chapter 2, there is clear value in simple, fast acting drivetrain models in the context of wind turbine main bearings. Such models are developed in this chapter and compared with higher fidelity finite element models before being applied to study force and moment loads on wind turbine main bearings during typical operational conditions. The simplicity and speed of such models allows for large numbers of load cases to be analysed rapidly in order to seek possible identifiable trends or recurring off-design load events which may require more detailed scrutiny. The demand for them is also growing as they'll be required for integration into digital twin models and farm-wide modelling tools. While practical for such analyses, it is important to consider the uncertainty of these models given their inherent simplifying assumptions and the existence of different load reaction behaviours for different bearing types. These uncertainty considerations form part of this chapter. The simplifying assumptions and use case for different bearings with different behaviours is analysed with comparisons to finite element (FE) models. The SMB model and turbulent wind field simulations from [29] will be used here and so both will be described below in more detail.

3.1 Background

The simple analytical representations built on in the current work were first presented in [29] where they were used to study the general characteristics of main bearing loads and their relationship to the incident wind field. While three drivetrain configurations were presented in [29] consisting of a SMB and two DMB representations, the SMB system was used for further study in [28] where repeating structures in time-varying main bearing loading were identified and characterised. The SMB system will also be considered here.

The two-step decoupled method was utilised in [29] where hub loading time series were generated using Bladed software and then extracted and input to the analytical models to determine main bearing reaction loads. The same method and hub loading data will also be applied in this work. 3-Dimensional turbulent wind fields were first generated in Bladed software using a Kaimal spectrum to describe the second order wind field statistics. 6 different wind fields were generated for each combination of these second order statistics using different initial random number seeds as required for design certification and three parameters were used to characterise the wind fields [36]. These were hub-height mean wind speeds (10, 12, 16, 20m/s), turbulence intensity (TI) (low, medium and high as specified in turbine design standards [36]) and shear profile (power law shear exponents of 0.2 and 0.6). The combination of 6 different wind fields for each set of combination of parameters created 144 realistic 3D turbulent wind fields spanning a significant range of typical operational conditions. The 6 wind fields associated with each combination of the parameters will be referred to as common parameter load sets (CPLS).

A multi-body model of a 2MW rated wind turbine was then simulated operating in each of these 10 minute wind fields using the fully-aeroelastic Bladed software. Hub loading time series were extracted, providing 144 realistic 10-minute hub loading (in six degrees of freedom) time series for the 2MW turbine. This hub load data set was then used as inputs to the analytical drivetrain representations in order to study the

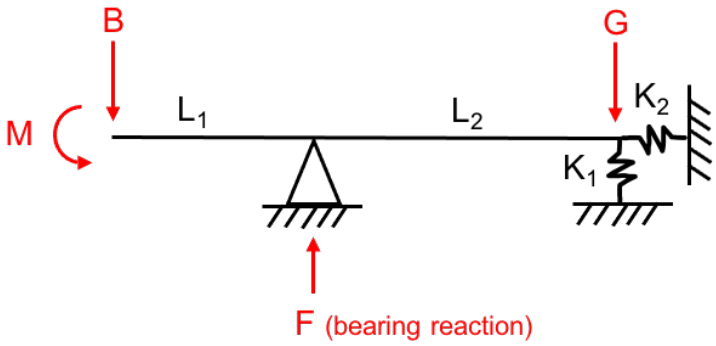

Figure 3.1: Analytic model for single main-bearing set-up in one plane. The full model consists of two such representations, one in each of the horizontal and vertical planes [29].

main bearing load characteristics. These hub load data sets will also be used as the input loads in this work. As mentioned previously, the SMB model from [29] will be considered here and is displayed in Figure 3.1.

The drivetrain details were provided by Onyx Insight, including the gearbox connections as radial and axial linear springs. Appropriate equivalent stiffness values of the low speed shaft to gearbox connections were determined with the use of Romax Technology FEM software. It is important to note that the overall model consists of two of the type shown in Figure 3.1, one in the horizontal plane and one in the vertical plane, with the resultant force being a vector combination of the two reaction forces at the main bearing. B and M represent force and moment loads at the hub and L_1 and L_2 represent the distances between the hub and main bearing, and main bearing and gearbox respectively. The axial and radial springs to the right of the model (K_1 and K_2) represent the connection between the shaft and gearbox as stiffness values, while G represents the gearbox weight in the vertical plane and is zero in the horizontal plane. F is the main bearing reaction force. All model parameters can be found in Table 3.1. The equation system for the SMB drivetrain set-up is statically determinate and can be solved by balancing the moments about the gearbox giving:

$$F = \frac{M + (L_1 + L_2)B}{L_2}. \tag{3.1}$$

While models and results in [29] demonstrate potentially important findings, the utilised models are simple, and hence come with limitations and uncertainties. The bearings are modelled as single point fixed supports, meaning that bearing clearance is ignored and all loading is reacted as forces at the main bearing - with no moment reactions present. The model is solved quasistatically by balancing the forces and moments on the system and, therefore, dynamic behaviours and gyroscopic effects are also ignored. Lubrication and friction effects are also not considered. The model also assumes the independence of loading and reaction behaviour in the horizontal and vertical planes and ignores 3-dimensional effects. As previously outlined, two common bearings used for wind turbine main bearings are DSRBs, which cannot support moment loads, and DTRBs, which can support both forces and moments [30, 62, 79]. Therefore, the validity and uncertainty of existing models when representing the different reaction behaviours of both DSRBs and DTRBS must necessarily be considered.

Table 3.1: Parameters for all models.

Model Parameters	
L_1	2.145m
L_2	2.615m
K_1	8E07N/m
K_2	4E06N/m
G	392280N
Shaft Diameter	0.4m

3.2 Finite Element Models

In order to assess the uncertainties of the simple analytical model used in previous work, two FE models were created in ANSYS to test the simplifying assumptions and application for DSRB and DTRB SMB systems. The FE models were designed to be general and do not seek to represent any particular bearing specifically, but rather the global behaviour of different bearing types; one designed to behave like a DSRB

(non-moment reacting) and the other to behave like a DTRB (does support moment loads). Likewise, the rest of the drivetrain system such as the shaft and gearbox connections remain both general and similar for the two different bearing types to create a like for like study. The models were subjected to the same hub loading as the analytical models, outlined in the previous section, with bearing support reaction forces outputted and compared with those from the analytical model. Both FE models share dimensions with the SMB analytical model. The FE models themselves still remain relatively simple, with relevant behaviours captured without the modelling of individual rolling elements - as described below. The 3-dimensional flexible bodies and different reactional capabilities of the FE models will test the orthogonality and simple support assumptions in the analytical model.

The FE models are simulated in a quasi-static environment and the models are designed such that the main bearing loads are isolated from the gearbox. Therefore, only the dynamic effects from the rotor end of the turbine are considered and shaft and bearing rotation is ignored. As dynamic effects from the rotor mass and inertia have already been captured in the aeroelastic simulations they do not need to be modelled here. The mass and inertia of the main shaft could have dynamic effects on bearing loading but are not modelled here due to their negligible effect in comparison to the mass and inertia of the rotor.

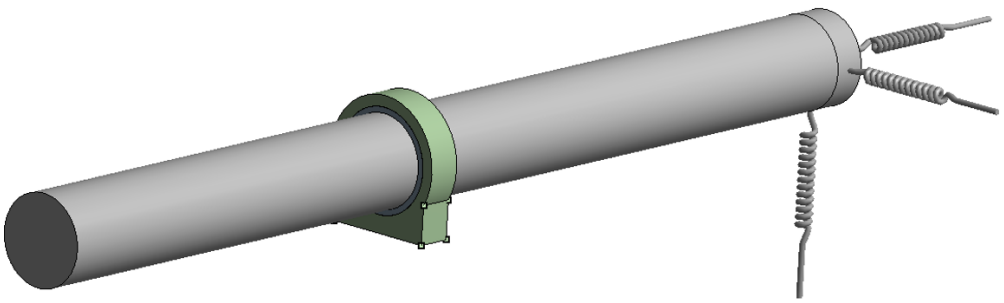

Figure 3.2: The 3-dimensional finite element model with double row spherical roller bearing type reaction behaviour.

DSRB FE Model - The DSRB FE model was created with 3 separate flexible bodies; referred to here as the shaft, the bearing and the bearing housing (see Figure 3.3a). The bearing was connected to the shaft using a bonded type contact and the convex outer face of the bearing was connected to the concave inner face of the bearing housing with a spherical joint. This type of connection allows the bearing housing to deformably react forces in the horizontal, vertical and axial axes while being able to move freely in the rotational degrees of freedom, allowing the non-moment reacting behaviour of a DSRB to be captured without the complex modelling of individual rollers. The spherical joint connection type is modelled without clearance between the two contact surfaces, and so bearing clearance is neglected here. The influence of material and lubrication damping is not expected to be large due to the significantly stiff design of the bearing unit and drivetrain system, therefore, damping is also neglected. The full model is displayed in Figure 3.2 and a sliced view of the bearing, housing and shaft can be seen in Figure 3.3a) side-by-side with SRB elements overlaid on the same image to demonstrate the interface type being represented. Bearing clearance is assumed to be zero since this parameter most directly influences the internal load distribution, rather than overall reaction force. The bedplate is assumed to be rigid in this model which, from previous work [44, 75], might result in conservatively higher bearing unit reaction force results than if bedplate flexibility were included. A fixed support was added to the base of the bearing housing to represent the connection to the bed plate and the connection between the low speed shaft and the gearbox was modelled by three body-to-ground spring connections in the horizontal, vertical and axial directions. Appropriate equivalent stiffness values of the low speed shaft to gearbox connections were determined with the use of Romax Technology software. The stiffness values, along with model dimensions, can be found in Table 3.1. The shaft, along with the rest of the model, was designed to be general and is modelled as a solid piece of material. Actual wind turbine main shafts tend to be a mostly solid piece of material, although a small bore hole will run throughout the centre to allow for wiring to pass to the hub. A shaft sensitivity analysis was therefore undertaken to determine the effect shaft thickness, and hence stiffness, has on results. Thicknesses of 100%, 75% and 50% were compared

to conservatively cover typical main shaft thicknesses and ensure the solid-shaft assumption does not impact the results of this work. Results are plotted in Figure 3.4 for the FE DSRB and FE DTRB models respectively. These results, in which only very small deviations can be seen for the DTRB model, indicate that shaft thickness appears to have a minimal effect on model accuracy. A convergence study was undertaken to determine appropriate mesh densities, resulting in smaller elements on the bearing and housing bodies and larger elements on the shaft. Input hub loading was applied to the front face of the shaft, the gearbox weight was applied to the rear of the shaft in the vertical axis and main bearing reaction forces extracted from the fixed support at the base of the housing.

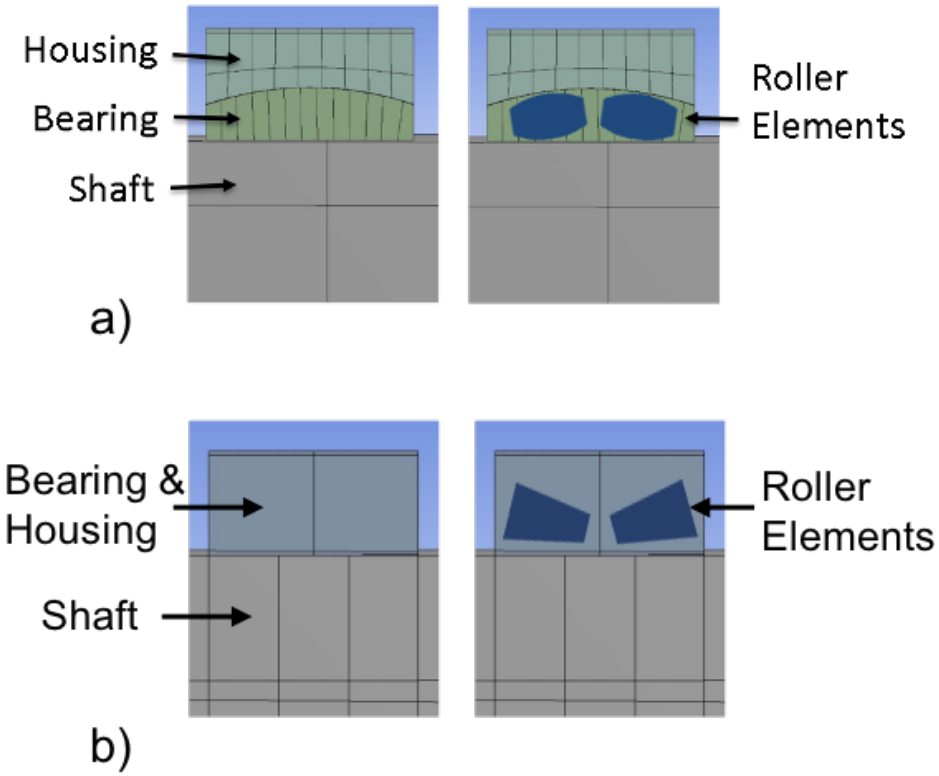

Figure 3.3: (a) A split view of the DSRB FE model displaying the geometries of the bearing and housing. (b) A split view of the DTRB FE model displaying the geometries of the bearing and housing. Note: The roller elements and mesh displayed in these images are for illustrative purposes only, a finer mesh was used for the simulations and rollers were not modelled.

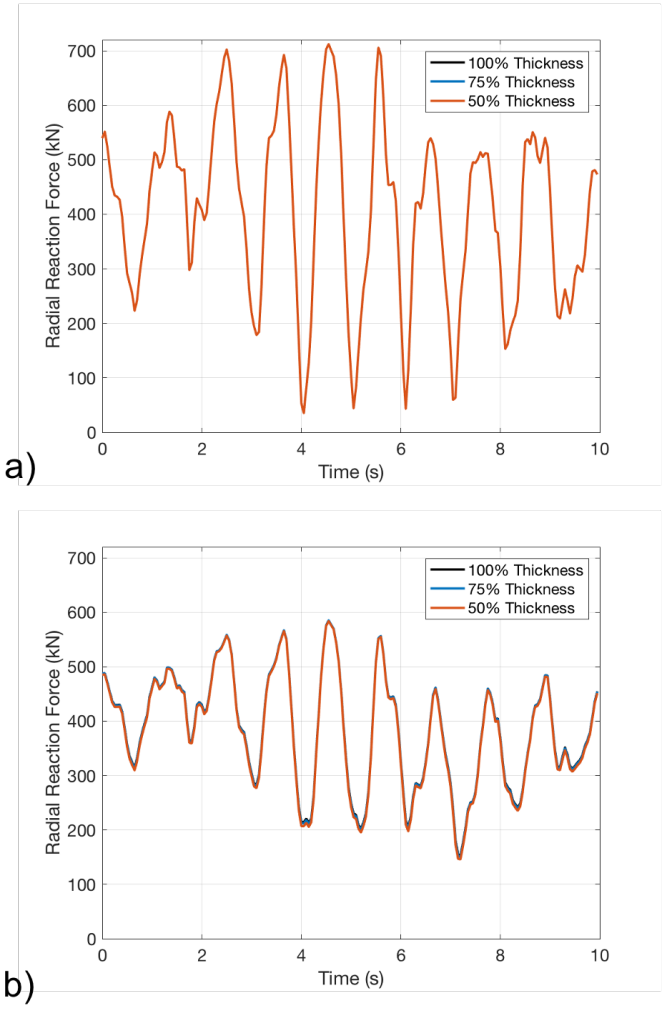

Figure 3.4: (a) 10 second time series of radial reaction force results of the finite element double row spherical roller bearing model with varying degrees of shaft thickness. (b) 10 second time series of radial reaction force results of the finite element double row tapered roller bearing model with varying degrees of shaft thickness.

DTRB FE Model - The DTRB FE model was created with two separate flexible bodies; referred to here as the shaft and the bearing/bearing housing (see Figure 3.3b). The bearing/bearing housing was modelled as one piece of material and connected to the shaft using a bonded type contact. This assumes zero clearance between the rollers and housing (typically found in pre-loaded DTRBs) and allows the bearing unit to emulate the force and moment reaction properties of a DTRB. The dimensions of the model, assumptions of a rigid bedplate and fixed support connection from the base of

the bearing/bearing housing to the bedplate are the same as that outlined above in the DSRB description. The low speed shaft equivalent connection to the gearbox and applications of hub and gearbox loading are also the same as described above. The full model is displayed in Figure 3.5 and a sliced view of the bearing/bearing housing and shaft can be seen in Figure 3.3b side-by-side with TRB elements overlaid on the same image to demonstrate the interface type being represented. Model parameters can be found in Table 3.1. The shaft was again modelled as a solid piece of material as the sensitivity analysis results showed insignificant differences between results. A convergence study was again undertaken to determine appropriate mesh densities. The DTRB main bearing reaction forces were extracted from the fixed support at the base of the housing.

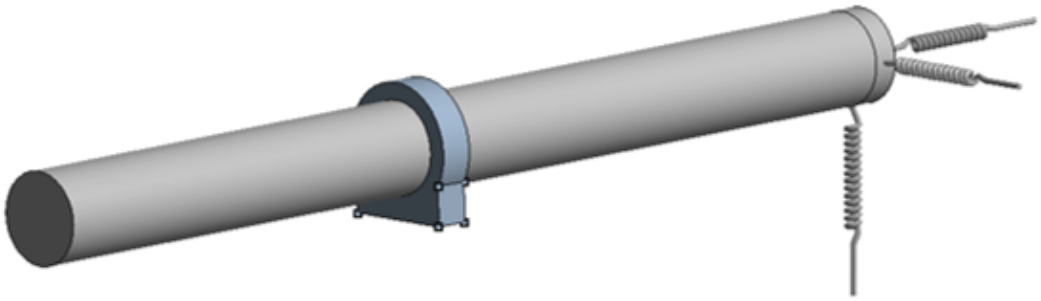

Figure 3.5: The 3-dimensional finite element model with double row tapered roller bearing type reaction behaviour.

Bearing contact assumptions - Internal contact conditions and load distributions around the bearing circumference are important (and non-linear) aspects of bearing behaviour. However, the SMB analytical model being studied is not designed to go to this level of detail - instead outputting the reaction forces at (or equivalently the loads applied to) the main bearing unit as a whole. As such, the simplified FE representations for DSRB and DTRB bearings outlined above are considered reasonable for the following reasons: DSRB case - DSRBs are self-aligning and hence provide force but not moment reactions across the bearing, as such, the reaction force required to balance the system should remain the same irrespective of the spring properties, with only displacement magnitudes effected, since the system is determinate. DTRB case -

in the DTRB case the system supports moments through opposite force reactions over the two bearing rows in addition to providing an overall force reaction. Consequently, nonlinear contact properties of the rollers will influence the share between force and moment reactions at the MB. However, the non-linearity present in line contact rollers[1] is only slight, with an exponent of 1.11 [26], and so they are reasonably approximated as linear [15, 69]. Considering the FE models developed here are for the evaluation of effective load reactions from simple analytical representations, it is therefore argued that the FE DTRB model presented here sensibly recreates load reaction behaviours of the desired types under quasi-static conditions.

3.2.1 Comparison results

The analytical model presented in Section 3.1 was compared with the FE models described in Section 3.2 to determine its validity when the 2D orthogonality and simply-supported reaction assumptions are removed. The models were compared by performing a root mean squared error (RMSE) analysis between the reaction force results for the models across the whole range of turbulent wind field load time histories. Plots of RMSE between the analytical and two FE models are shown in Figures 3.6 and 3.8, along with example time series plots of main bearing reaction forces in Figures 3.7 and 3.9. The RMSE plots present the mean and standard deviations within each CPLS (which each capture results from 6 wind files with parameters in common) with respect to mean wind speed, turbulence intensity and shear profile. Note that mean wind speed values are staggered for clarity.

Figure 3.6 displays RMSE results between the analytical model and the DSRB FE model in the horizontal and vertical planes. The accuracy of the analytical model in the horizontal axis appears to have slight sensitivities to wind speed and shear exponents, decreasing as their values increase. The RMSE results for the bearing reaction force in the vertical axis are more differentiated by the varying wind parameters than in the horizontal axis. The low shear results remain fairly constant with increasing wind

[1] Including tapered and cylindrical cases.

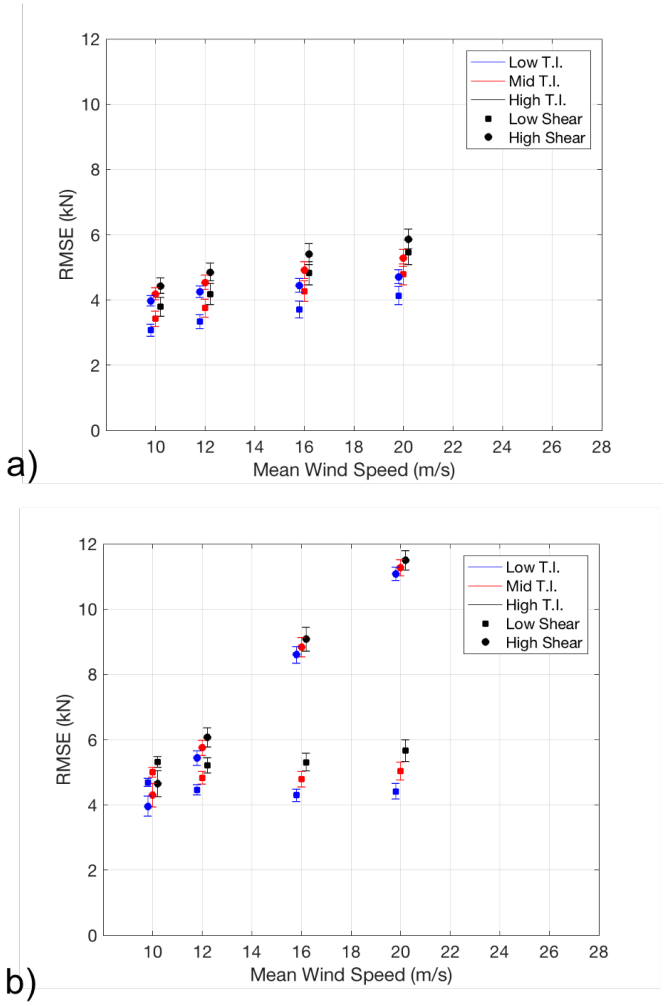

Figure 3.6: (a) RMSE between reaction forces from the analytical and DSRB FE model in the **horizontal plane**. The mean and standard deviations within each CPLS are plotted, staggered about mean wind speed for clarity. (b) RMSE reaction force results between the analytical and DSRB FE model in the **vertical plane**. The mean and standard deviations within each CPLS are plotted, staggered about mean wind speed for clarity.

speed, although increasing sensitivity to TI with increasing wind speed can be seen. The high shear exponent results are more sensitive to wind speed with RMSE values increasing with wind speed. To put these results into context, the mean percentage error between resultant force magnitudes for the two models across all wind files is 1.54%, with a mean correlation coefficient of 0.9996. These results indicate that the analytical model does in fact give good results across all tested wind profiles in both

planes when compared with 3D model outputs. This conclusion is reinforced when one considers time series of these loads, with examples shown in Figure 3.7.

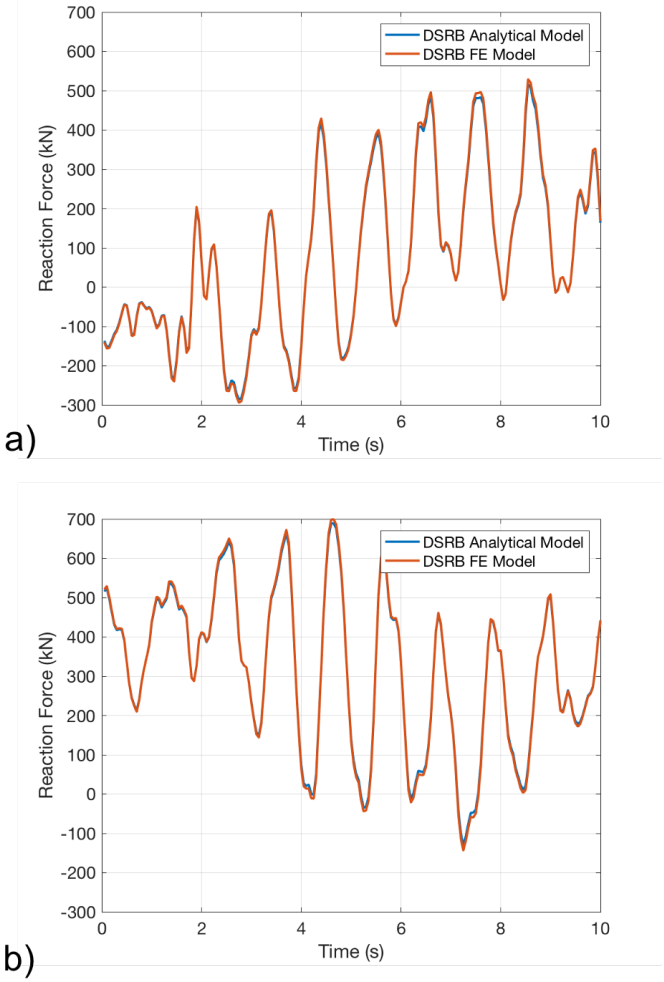

Figure 3.7: (a) Example time series of reaction force results in the **horizontal plane** from the analytical and DSRB FE models. (b) Example time series of reaction force results in the **vertical plane** from analytical and DSRB FE models.

The analytical model reaction force results were then compared with the DTRB FE model, with the results displayed in Figure 3.8. The analytical model shows a trend of decreasing accuracy with increasing wind speed and shear in the horizontal plane. Compared to the previous results, error values can be seen to have significantly increased by more than a factor of 10. The accuracy of the model in the vertical plane is highly sensitive to wind shear. Increasing mean wind speeds and TI slightly decreases

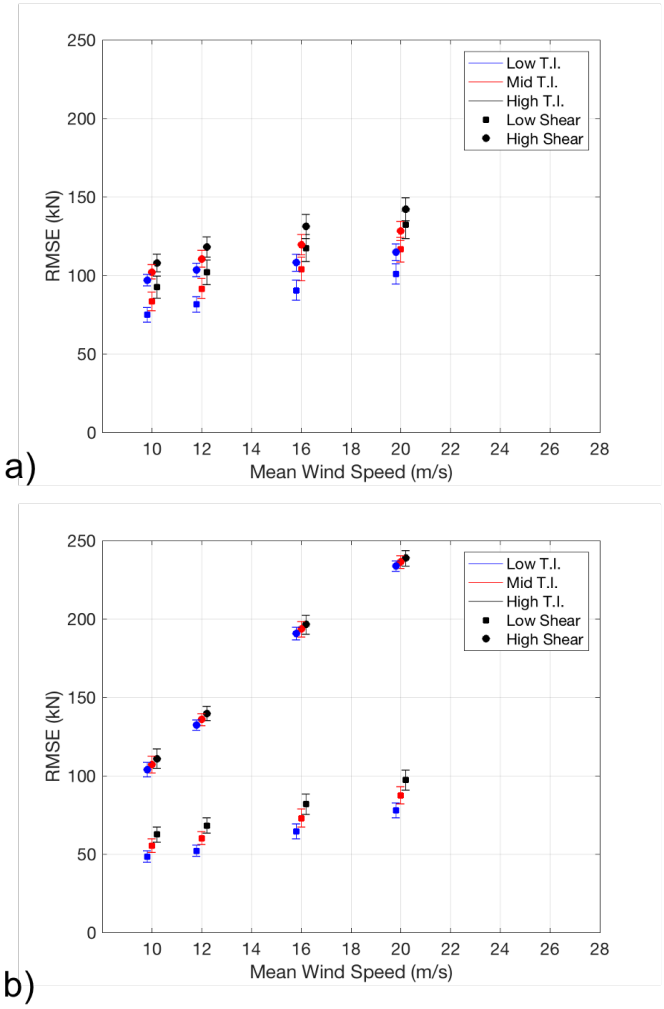

Figure 3.8: (a) RMSE between reaction forces from the analytical and DTRB FE model in the **horizontal plane**. The mean and standard deviations within each CPLS are plotted, staggered about mean wind speed for clarity. (b) RMSE reaction force results between the analytical and DTRB FE model in the **vertical plane**. The mean and standard deviations within each CPLS are plotted, staggered about mean wind speed for clarity.

the accuracy of the low shear results in the vertical plane. In contrast, the high shear exponent results in the vertical plane significantly decrease in accuracy with increasing mean wind speeds and show less sensitivity to TI. The mean percentage error and correlation coefficient were again considered between resultant force magnitudes across all wind cases. The mean error was found to be 22.74% and a mean correlation coefficient of 0.7781 was calculated, showing that the analytical model is noticeably less accurate

in the DTRB, moment-reacting, case. This conclusion is again reinforced by time series of model outputs, examples of which are shown in Figure 3.9.

The above comparisons suggest the orthogonal independence and simple support assumptions made in the analytical model allow for valid force outputs when representing a DSRB. However, the results also show that the analytical model has significantly overestimated the force reactions for the DTRB system. This motivates the derivation of a new analytical model to try and emulate the positive results seen in the DSRB case for moment reacting DTRBs. Such a model is developed in the following section.

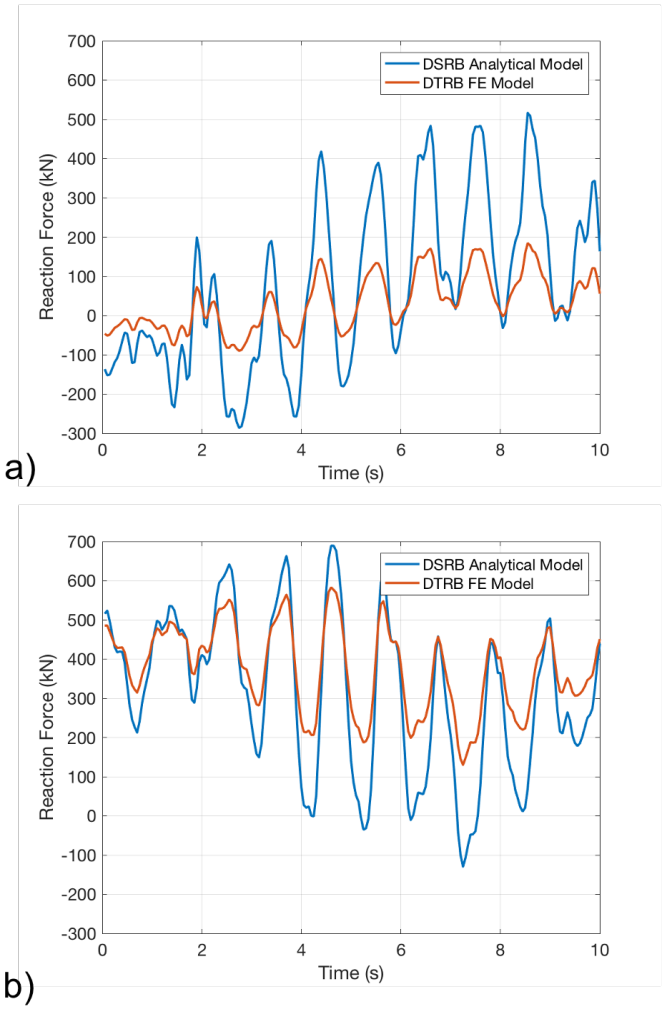

Figure 3.9: (a) Example time series of reaction force results in the **horizontal plane** from the analytical and DTRB FE models. (b) Example time series of reaction force results in the **vertical plane** from analytical and DTRB FE models.

3.3 Extending the Analytical Model to Include Moment Reactions

In order to extend the capabilities of the analytical model and allow moment reactions at the main bearing, torsional springs were added to the fixed bearing support in both planes. Thus, a new analytical model was created, displayed in Figure 3.10(a). The model will be simulated under the same load conditions above and results compared with that of the DTRB FE model to determine if torsional springs can emulate the moment reacting capabilities of the DTRB case. Firstly, the set of equations for the new model must be derived and sensible values of spring stiffness calculated. The set of equations for the new analytical model are statically indeterminate and so the model must be decoupled to find a solution [34, 40]. The model was first simplified by moving the location of the force applied by the rotor mass, B, and associated overturning moment, M, to be positioned at the bearing support mount as shown in Figure 3.10(b). The model was then decoupled into two deflection models; one which has the rotor weight and overturning moment acting on the structure (Figure 3.11(a)) and one which has the reaction moment from the torsional spring acting on the structure (Figure 3.11(e)).

The two deflection models can then be decoupled again to show the two mechanisms causing deflection in the shaft; bending of the beam due to the applied moment, and rotation about the MB support due to spring support (gearbox) compression/extension. The two deflection mechanisms for the decoupled models are shown in Figure 3.11. As the deflection mechanisms and equation derivation process is similar for the overturning moment and spring reaction moment on the system, only the equations for the overturning moment is presented here.

Calculating θ_{11} as seen in Figure 3.11(b) can be done by utilising the beam deflection formula shown in Equation 3.2 [53].

$$\theta_{11} = \frac{(M + BL_1)L_2}{3EI} \tag{3.2}$$

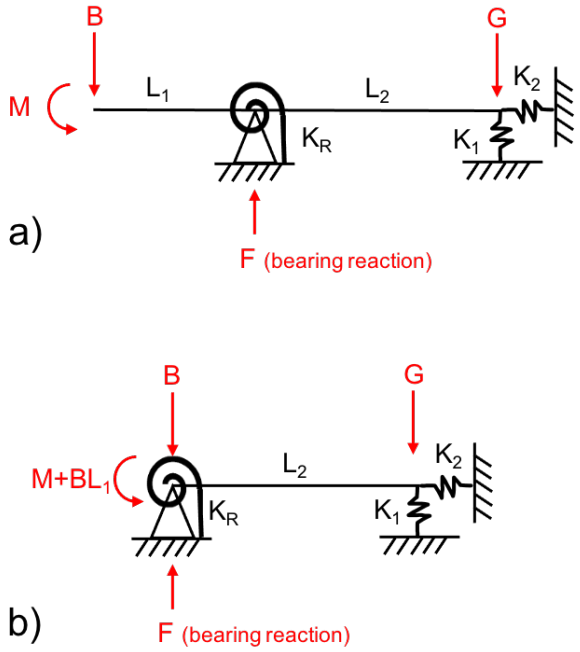

Figure 3.10: (a) Analytical model for single main-bearing setup with torsional spring to include moment reactions. The overall model consists of one in the horizontal and one in the vertical plane. (b) Simplified analytical model with torsional spring.

The compression/extension length, y, of the spring must first be found before calculating θ_{12}. For a loaded spring with stiffness, K_1, the distance stretched or compressed, y, is equal to the reaction force divided by the stiffness.

$$y = \frac{R_B}{K_1}, \tag{3.3}$$

Trigonometrically, the deflection angle is then,

$$\tan\theta_{12} = \frac{y}{L_2}, \tag{3.4}$$

and a small-angle approximation simplifies the equation to,

$$\theta_{12} = \frac{y}{L_2}, \tag{3.5}$$

and combining with Equation 3.3 for y gives,

$$\theta_{12} = \frac{R_B}{K_1 L_2}. \tag{3.6}$$

The second set of deflection equations with respect to the reaction moment of the torsional spring on the shaft are calculated using the same method, with the angles of rotation labelled θ_{21} and θ_{22} (as seen in Figures 3.11f) and g), respectively) and taking values of,

$$\theta_{21} = \frac{M_T L_2}{3EI}, \tag{3.7}$$

and,

$$\theta_{22} = \frac{R_T}{K_1 L_2}. \tag{3.8}$$

The rotation of the torsional spring, θ_{TS}, is given by,

$$\theta_{TS} = \frac{-M_T}{K_R}, \tag{3.9}$$

where K_R is the stiffness of the torsional spring and M_T the reaction moment. The rotation of the torsional spring is also equal to the sum of all deflection angles, with positive and negative signs indicating direction,

$$\theta_{TS} = -\theta_{11} - \theta_{12} + \theta_{21} + \theta_{22}. \tag{3.10}$$

The reaction forces R_B and R_T are still unknowns and the above equation cannot be solved until the forces are balanced on the decoupled models. Balancing the moments about the bearing support in Figure 3.11(d) gives,

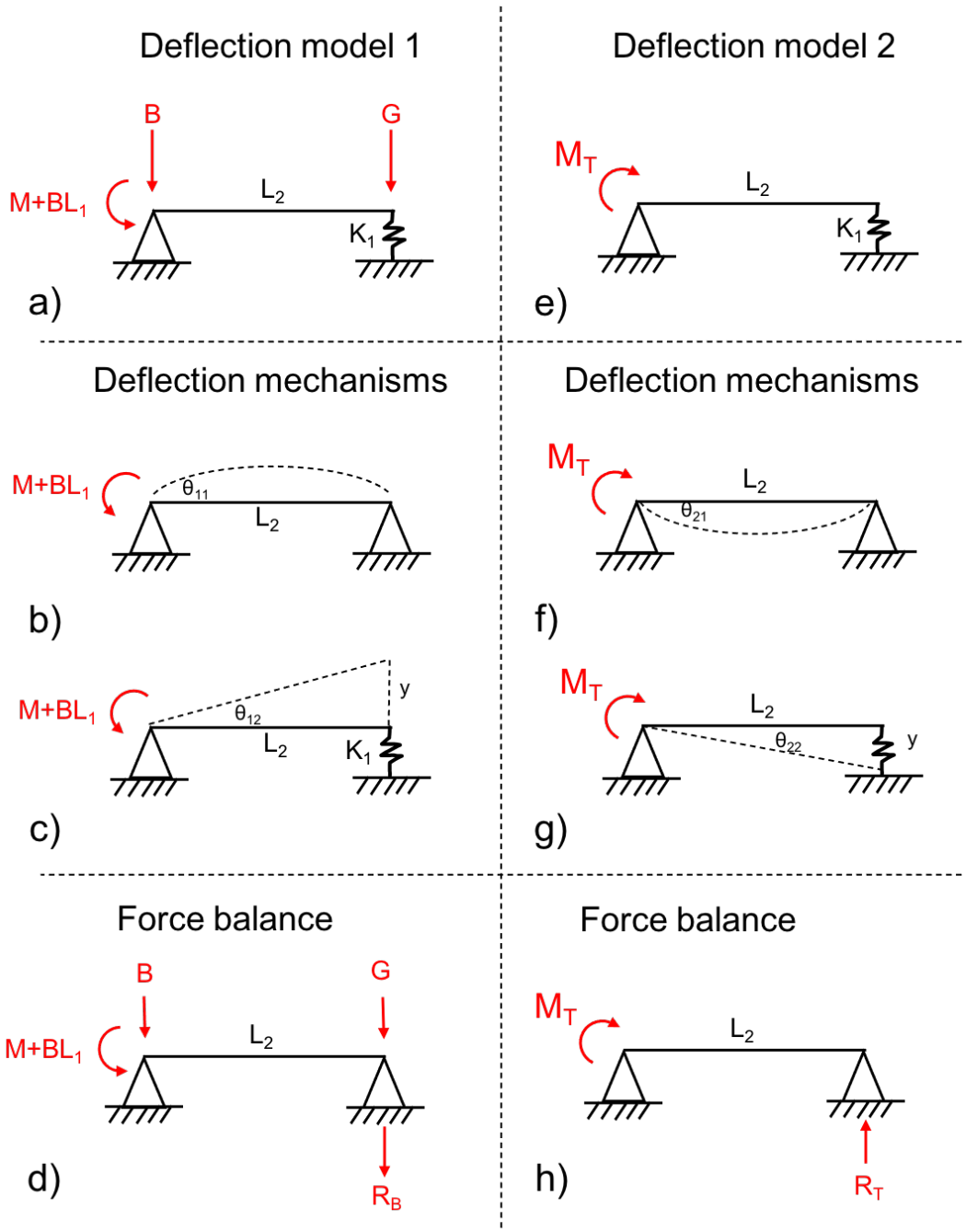

Figure 3.11: (a) Deflection model 1 (rotor weight and overturning moment). (b),(c) Deflection mechanisms for deflection model 1 under some applied moment $M + BL_1$. (d) Force balance corresponding to deflection model 1. (e) Deflection model 2 (torsional spring reaction force). (f),(g) Deflection mechanisms for deflection model 2. (h) Force balance corresponding to deflection model 2.

$$-(M + BL_1) + GL_2 + R_B L_2 = 0, \tag{3.11}$$

from which it follows,

$$R_B = \frac{(M + L_1 B) - GL_2}{L_2}. \tag{3.12}$$

Similarly, moments can be balanced about the bearing support for the decoupled model loaded with the reaction moment from the torsional spring displayed in Figure 3.11(h) giving,

$$M_T - R_T L_2 = 0, \tag{3.13}$$

and hence,

$$R_T = \frac{M_T}{L_2}. \tag{3.14}$$

These expressions for R_B and R_T can now be entered into Equations 3.6 and 3.8, respectively, resulting in solvable equations for θ_{12} and θ_{22}:

$$\theta_{12} = \frac{(M + L_1 B) - GL_2}{K_1 L_2^2}, \tag{3.15}$$

$$\theta_{22} = \frac{M_T}{K_1 L_2^2}. \tag{3.16}$$

Equation 3.10 can therefore be written in full in terms of known quantities as,

$$-\frac{M_T}{K_R} = -\frac{(M + BL_1)L_2}{3EI} - \frac{(M + BL_1) - GL_2}{K_1 L_2^2} + \frac{M_T L_2}{3EI} + \frac{M_T}{K_1 L_2^2}, \tag{3.17}$$

and rearranged for M_T as,

$$M_T = \left[\frac{(M + BL_1)L_2}{3EI} + \frac{(M + BL_1) - GL_2}{K_1 L_2^2}\right] \left[\frac{1}{\frac{1}{K_R} + \frac{1}{K_1 L_2^2} + \frac{L_2}{3EI}}\right]. \tag{3.18}$$

The equation for the reaction moment from the torsional spring, M_T, has been derived and, as such, the system is now statically determinate. A moment balance can be performed on the gearbox support over the whole system, as shown in Figure 3.12, to derive the reaction force at the bearing support, R_A,

$$R_A = \frac{M + B(L_1 + L_2) - M_T}{L_2}. \tag{3.19}$$

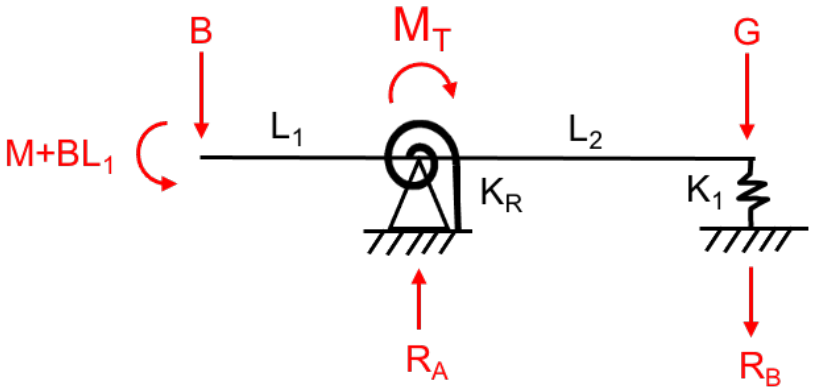

Figure 3.12: Force balance model for the whole system

3.3.1 Estimating Torsional Spring Stiffness

Having derived the relevant equations for a new analytical model with moment reaction capabilities, it is then necessary to determine appropriate spring-stiffness values in each plane. The following section details a developed methodology which utilises the FE DTRB model to estimate the torsional spring stiffness values. The body-to-ground springs representing the shaft connection to the gearbox were first removed from the FE model and then four nodes were selected: one at the bedplate connection and one at the

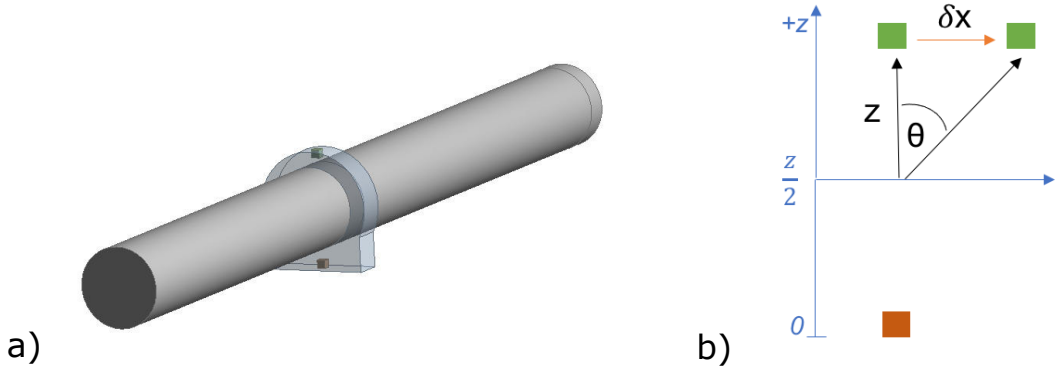

Figure 3.13: Node selection within the bearing housing for estimating torsional spring stiffness in the vertical plane.

top of the bearing housing for the vertical plane, and one on both sides of the bearing housing at points of mid height and mid thickness for the horizontal plane. Known moments were then applied about the horizontal and vertical axes separately and the displacement of the nodes recorded. The angle of rotation about the mid point of the vertical nodes was calculated and used to determine the vertical axis spring stiffness via the standard spring equation (Equation 3.20). Likewise, the angle of rotation about the centre of the housing between the pre and post-loaded nodal points was calculated and the torsional spring stiffness about the horizontal axis estimated. These steps are illustrated in Figures 3.13 and 3.14.

$$K = \frac{M}{\theta} \tag{3.20}$$

The two estimated spring stiffness values, approximately 392MNm/rad in the horizontal plane and 145MNm/rad in the vertical plane, were then applied in the analytical DTRB model and the reaction forces at the bearing calculated across the wind profiles. The results were again compared with the reaction force results of the FE DTRB model through an RMSE analysis, plotted alongside example time series plots in Figure 3.15.

It can be seen from the plots that the inclusion of the torsional springs greatly reduces the RMSE values, as well as variance within each CPLS, between the analytical and

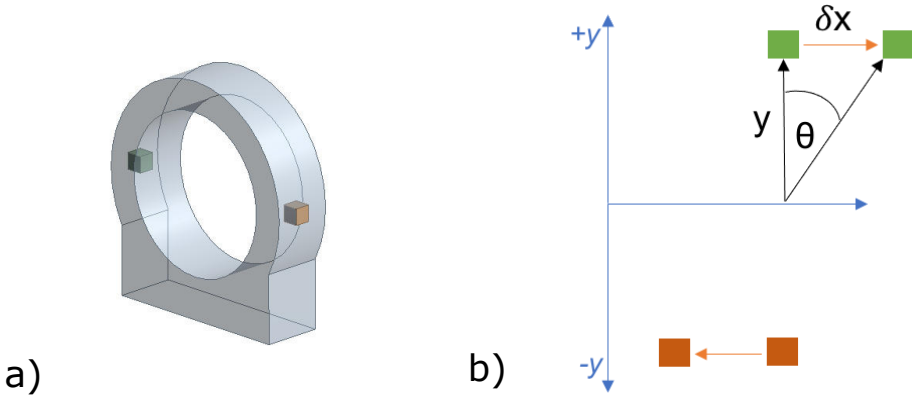

Figure 3.14: Node selection within the bearing housing for estimating torsional spring stiffness in the horizontal plane.

DTRB FE models in both the horizontal and vertical planes. The mean absolute error and mean correlation coefficients between resultant force magnitudes were calculated for the two models; mean percentage error in this case has dropped to 1.61% while the mean correlation coefficient has increased to 0.9996. The results in Figure 3.15 show shear profile to have the strongest effect on model accuracy in the vertical plane. It can also be seen that the low shear cases accuracy increases with increasing mean wind speed while high shear cases accuracy decreases with increasing mean wind speed. There is very little variation in the horizontal plane with increased T.I. and mean wind speed resulting in marginally less accurate results. Examining the time series plots of the reaction forces, the new analytical model appears to capture the loading seen by the FE DTRB model very closely in both planes.

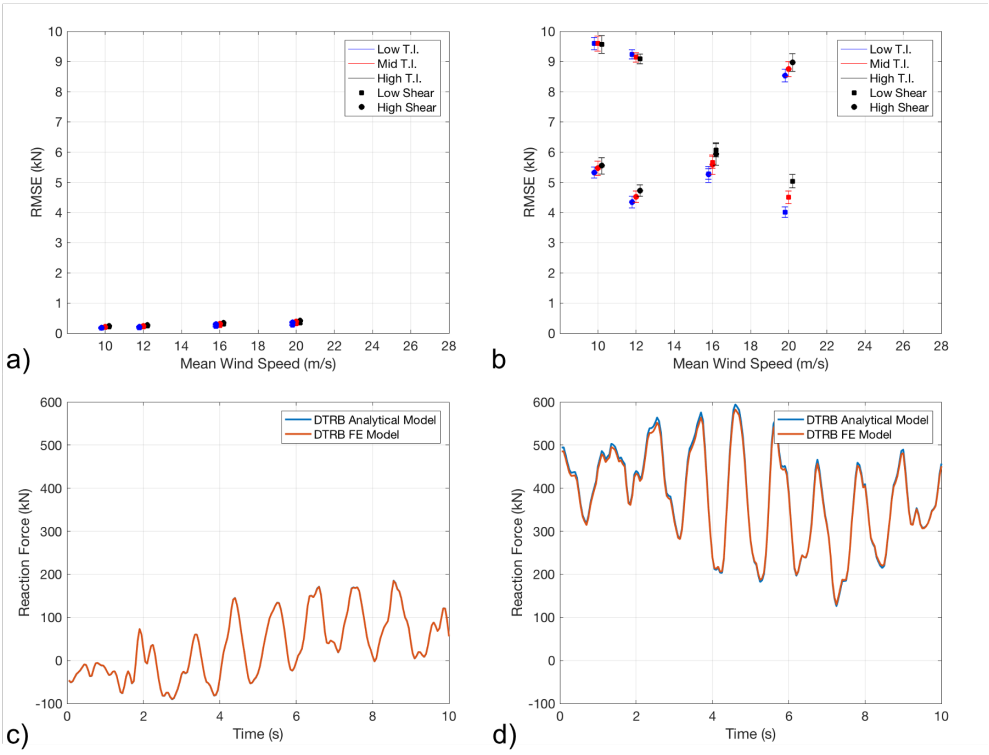

Figure 3.15: (a) RMSE between reaction forces from the analytical DTRB (with torsional springs) and DTRB FE model in the **horizontal plane**. The mean and standard deviations within each CPLS are plotted, staggered about mean wind speed for clarity. (b) RMSE reaction force results between the analytical DTRB (with torsional springs) and DTRB FE model in the **vertical plane**. The mean and standard deviations within each CPLS are plotted, staggered about mean wind speed for clarity. (c) Example time series of reaction force results in the **horizontal plane** from the analytical DTRB (with torsional springs) and DTRB FE models. (d) Example time series of reaction force results in the **vertical plane** from analytical DTRB (with torsional springs) and DTRB FE models.

3.4 Investigating mean and peak loads of a SMB with DSRB and DTRB supports

Presented results imply that the analytical SMB model used in [29] and the analytical moment reacting model developed here provide good representations of DSRB and DTRB type reaction forces (and moments in the latter case) respectively. As where in previous work the mean and peak loads across operating points were considered, here these same values will be investigated for the DTRB case using the analytical DTRB

model, with the original being referred to as the analytical DSRB model. The mean and standard deviation of the mean and peak radial loads for each set of 6 CPLS are plotted in Figure 3.16 with mean wind speeds staggered for clarity.

The mean radial loading for the analytical DSRB model (Figure 3.16(a)) shows high sensitivity to shear exponent with the low shear exponent wind files resulting in larger radial loading across the operating points. Plotted low shear mean loading results lay between 400kN and 500kN, similarly, high shear exponent plotted results were between around 200kN and 300kN. The mean loads within each CPLS remained fairly constant with small standard deviations. The variance seems to increase with increasing mean wind speed for both mean and peak loads and TI had some effect on the results, with higher TI resulting in slightly higher loading.

Mean radial force and moment results for the analytical DTRB model are shown in Figures 3.16(c) and 3.16(e) respectively. The inclusion of moment reacting capabilities appears to have minimal effect on mean force loading of the main bearing across all operating points. High sensitivities to wind shear are still present for the DTRB case with low shear wind conditions resulting in higher force loading. However, it can be seen that high shear profile wind fields result in higher moment loading. The mean force loads show less variation with mean wind speed and TI when compared to the DSRB results and the mean moment loads increase in magnitude with increasing mean wind speed. The mean moment loads also show slight sensitivity to TI in both shear exponent cases with high TI resulting in slightly higher mean loading.

The analytical DSRB peak radial loads are plotted in Figure 3.16(b) and show peak loads increasing in size and variability with increasing wind speeds. The peak loads see significant changes with TI but are most sensitive to shear exponent. The inclusion of moment-reacting capabilities in the DTRB model seems to reduce the mean peak force loading across the operating points as displayed in Figure 3.16(d), with the largest reduction seen in the low shear cases. Sensitivities remain for TI and the variation of mean peak force loads increases with increasing mean wind speed. The low shear wind conditions see increasing magnitudes and high shear conditions see reduced peak

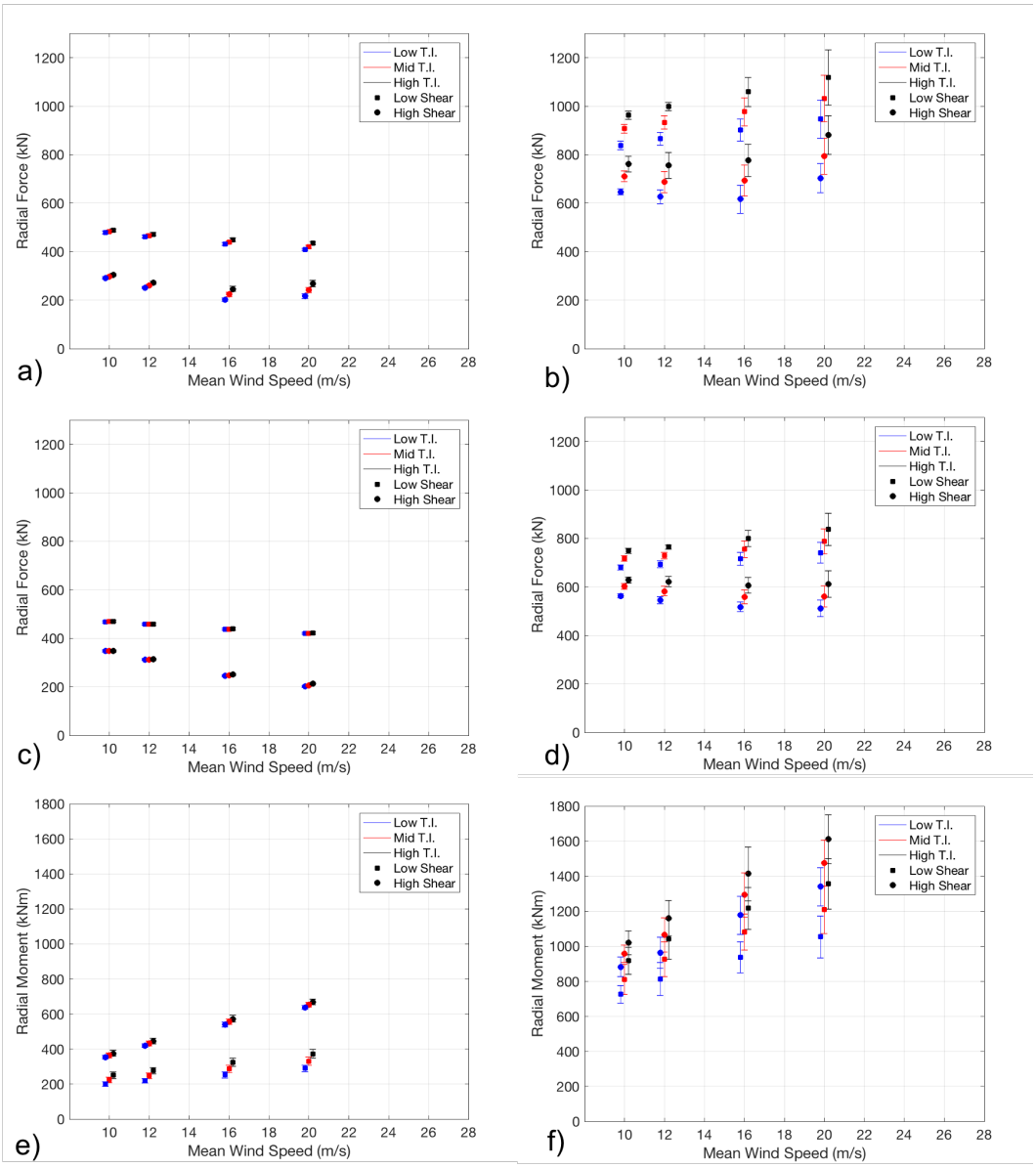

Figure 3.16: (a) **Mean** radial resultant **force magnitudes** from the analytical DSRB model. (b) **Peak** radial resultant **force magnitudes** from the analytical DSRB model. (c) **Mean** radial resultant **force magnitudes** from the analytical DTRB model. (d) **Peak** radial resultant **force magnitudes** from the analytical DTRB model. (e) **Mean** resultant **moment magnitudes** from the analytical DTRB model. (f) **Peak** resultant **moment magnitudes** from the analytical DTRB model. Mean and standard deviations within each CPLS are plotted in all graphs, staggered about mean wind speeds for clarity.

magnitudes with increasing wind speed. The peak moment loads displayed in Figure 3.16(f) show high overall sensitivity to shear exponent, TI and mean wind speed with increasing mean wind speed, TI and shear profile resulting in greater magnitudes and variations of peak moment loading. It is thought that the higher moment loading in high shear cases is somewhat uplifting the rotor weight, reducing the gravitational force loading hence the lower mean and peak force loads seen in the high shear wind files for the two reaction types.

3.5 Visual Inspection of Loads

Having examined the mean and peak loads for SMB systems with both bearing reaction types and determining that the inclusion of moment-reacting capabilities reduces the peak radial force loading in the system, the radial loading was then investigated visually. Figures 3.17 & 3.18 display polar plots of main bearing radial force and moment loading outputted from the analytical DTRB model. The results are generated from 10,12,16 and 20m/s mean wind speed data sets with low shear profile and medium TI as defined by IEC. The 10 and 12m/s results are displayed in Figure 3.17 and Figure 3.18 displays the 16 and 20m/s results. All results are plotted such that they show the magnitude and direction of loads from the perspective of looking downwind onto the main bearing. The force loads are concentrated downwards in the vertical direction due to the significant mass of the rotor and become less concentrated with larger fluctuations in magnitude and direction occurring with increasing mean wind speed. The moment loads also increase in magnitude with mean wind speed but are not concentrated at any particular direction, showing to load the bearing around it's full circumference.

The edges of the force and moment plots indicate the presence of additional dynamic structures as explored in [28]. Hart visually explored DSRB main bearing loads in [28] and found the occurrence of repeating loop patterns throughout much of the loading time histories which rapidly change the magnitude and direction of loads. A method was developed to identify and characterise the loop structures before suggesting they may be causing or exacerbating fatigue or non-fatigue failures of rollers. Shorter time

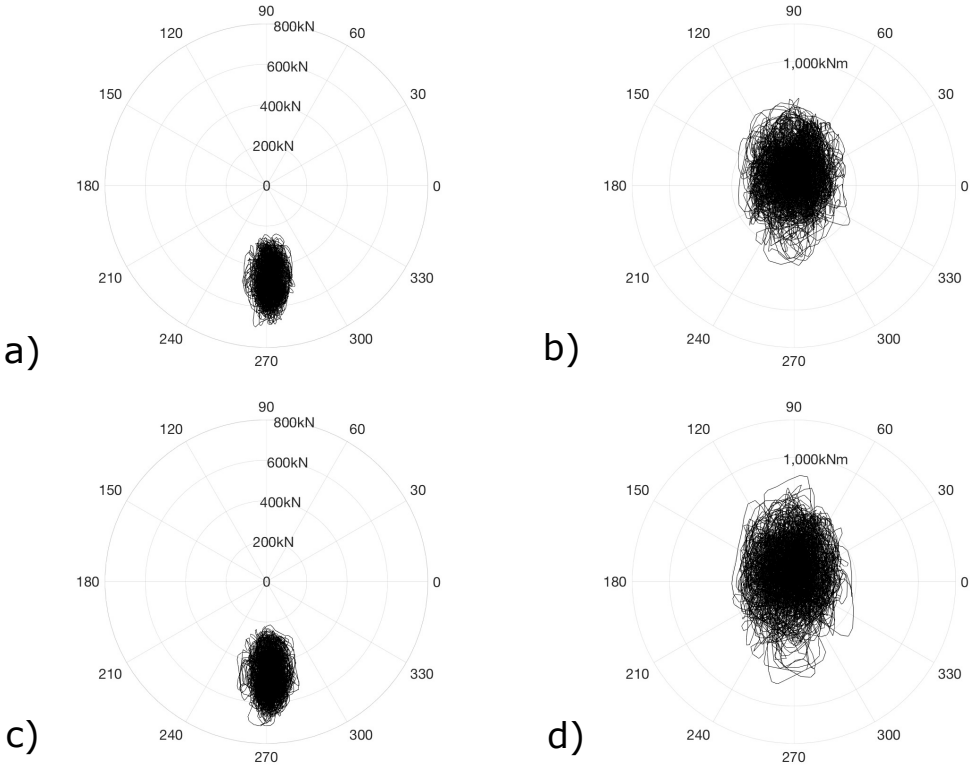

Figure 3.17: a) and b) show 10 minute time series plots of radial force and moment loads for a wind file with mean wind speed of 10m/s, medium turbulence intensity and low shear profile. c) and d) show 10 minute time series plots of radial force and moment loads for a wind file with mean wind speed of 12m/s, medium turbulence intensity and low shear profile.

samples were examined for the DTRB case to investigate the presence of loop structures and some examples are plotted in Figure 3.19.

Loop structures were found in both the force and moment loading time histories across the full envelope of normal turbine operational conditions. Examples of such from three different wind files with different second order parameters are displayed in Figure 3.19. The circle represents the start of the plot and the square the end for all plots in Figure 3.19. Figures 3.19a) and 3.19b) display loop structures spanning a period of 1.5 seconds from a 10m/s mean wind speed file with medium TI and low shear profile. The force load changes from approximately 500kN to 400kN and back again in this time period with small directional changes. The moment loads during this time period show

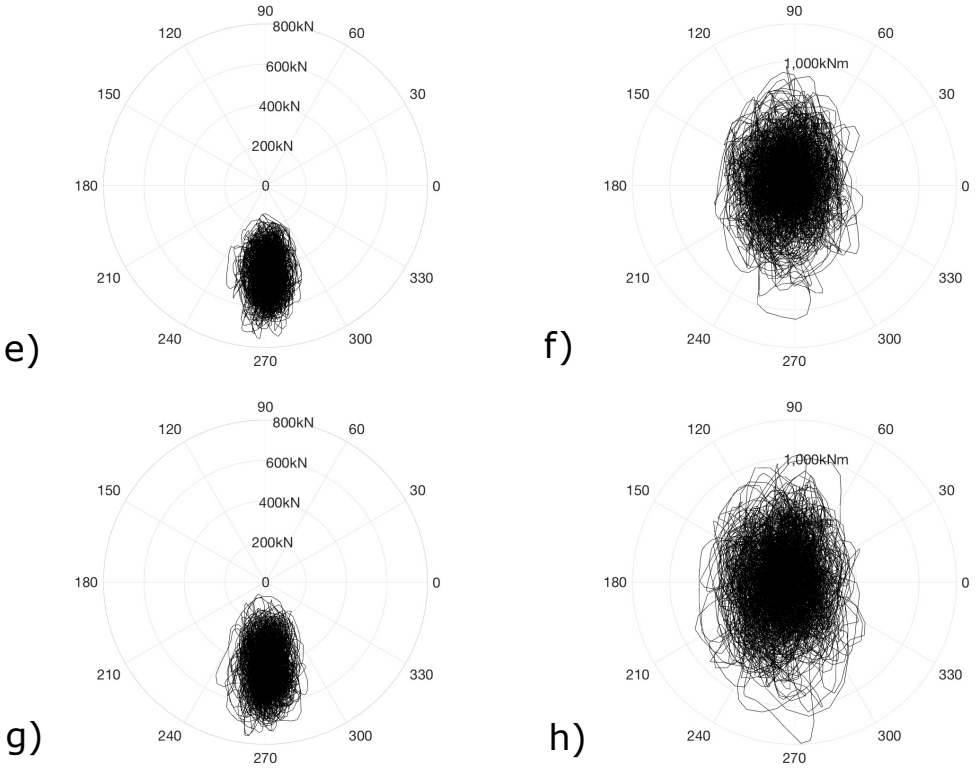

Figure 3.18: e) and f) show 10 minute time series plots of radial force and moment loads for a wind file with mean wind speed of 16m/s, medium turbulence intensity and low shear profile. g) and h) show 10 minute time series plots of radial force and moment loads for a wind file with mean wind speed of 20m/s, medium turbulence intensity and low shear profile.

to rapidly drop from 100kNm to 0 and then shoot to approximately 500kNm in the opposite direction. In this example the moment direction changes a full 360 degrees during the loop. Figures 3.19c) & 3.19d) show force and moment radial load plots, respectively, from a wind file with mean wind speed of 16m/s, low TI and high shear spanning a period of 1 second. Within this second of loading, loop structures appear in both plots with magnitudes of loading reducing by more than half the original value before increasing again. The direction of the loading in both plots also changes by at least 30 degrees. Figures 3.19e) & 3.19f) show force and moment radial load plots, respectively, from a wind file with mean wind speed of 20m/s, high TI and low shear spanning a period of 1.5 seconds. The force plot shows a loop with a rapid drop and rise in magnitude from over 500kN to almost completely unloaded and back to over 400kN

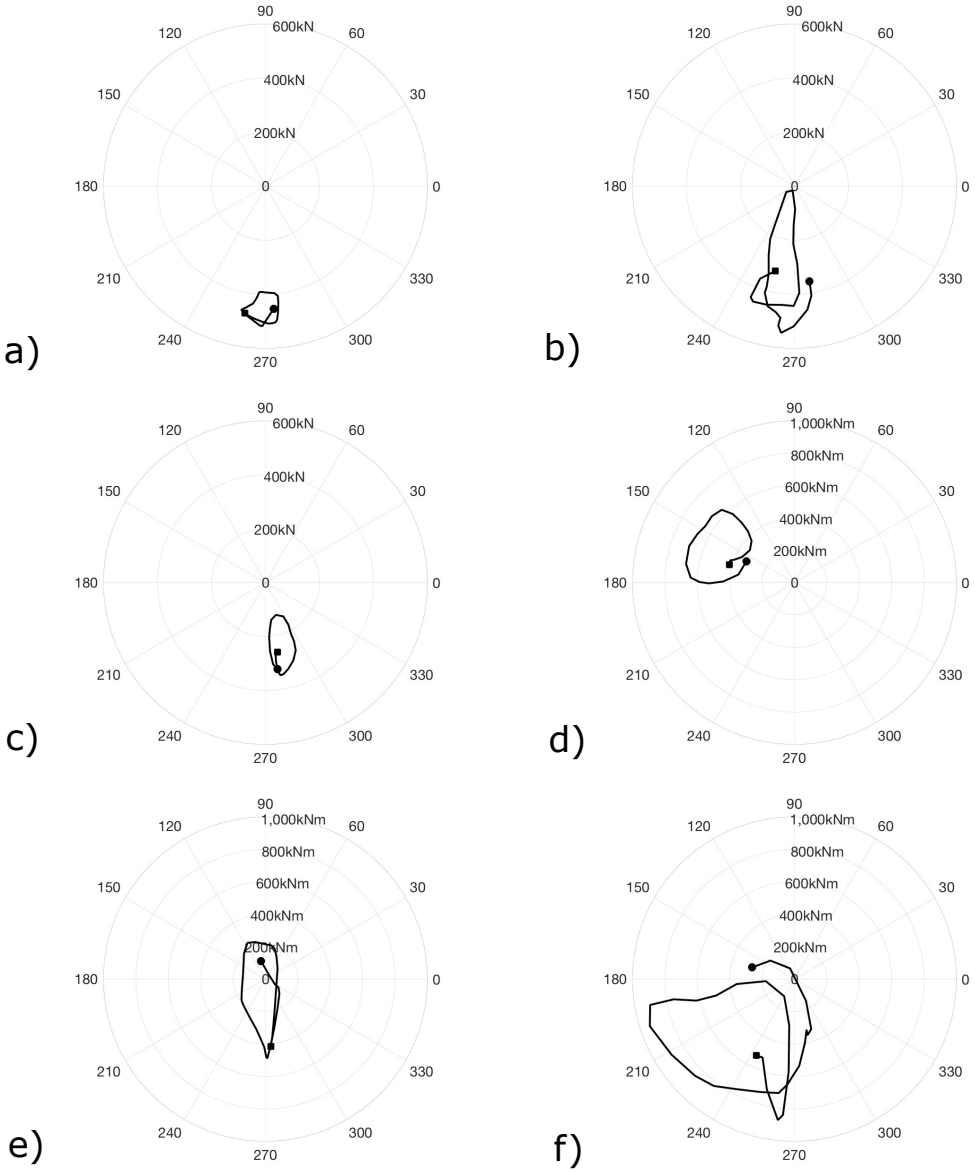

Figure 3.19: Circles represent the start and squares represent the end of all plots. a) and b) represent force and moment loop structures, respectively, spanning 1.5 seconds in a wind file with 10m/s mean wind speed, medium TI and low shear. c) and d) represent force and moment loop structures, respectively, spanning 1 second in a wind file with 16m/s mean wind speed, low TI and high shear. e) and f) represent force and moment loop structures, respectively, spanning 1.5 seconds in a wind file with 20m/s mean wind speed, high TI and low shear.

while slightly changing direction. The moment load plot shows a similar loop with the load increasing from 0 to almost 1000kNm, dropping to approximately 100kNm and

then sharply rising to over 800kNm again all while dramatically changing direction by 90 degrees three times.

The direction of the moment on the polar plot indicates the direction of the axes the moment is acting upon. In other words, a moment plot with a direction of 0 degrees indicates maximum displacement at 270 and 90 degrees with the moment causing rotation around an imaginary axes at 0 degrees. The example loop structures presented do not represent other loop structures within the specified wind profile types, but have instead been selected to show a variety of operating conditions that exist throughout the complete operational envelope of the turbine. It is important to consider the effect such rapid changes in magnitude and direction of both force and moment loads, including rapid loading, unloading and reloading events and complete 360 degree directional changes, have on individual roller loads and on bearing raceways.

3.6 Discussion

The previous sections have developed a simple and efficient model representing a DTRB main bearing in a wind turbine system, tested the main assumptions through a comparative analysis with a more detailed 3-dimensional FE model and developed a methodology to estimate the torsional spring stiffness values. However, it is worth considering the practicalities and remaining assumptions of this approach given that the determined torsional spring values have a constant value, where DTRB have intrinsically non-linear stiffness behaviours, and that the method requires access to an FE model. Three pertinent questions related to this are therefore: 1) If one requires an FE model in the first place, why cannot all analysis be undertaken using it instead of the simplified representations proposed here? 2) Is it practical to assume an FE model will be available in general? 3) What are the accuracy limitations of assuming constant torsional stiffness and does this hinder the use case of this model?

With respect to the first question there are two main considerations which imply simplified models will likely be necessary. First, as has been touched upon, analysis over large

numbers of load-cases and/or turbines becomes infeasible for high complexity models due to processing power requirements. In addition, any MB load model which might be embedded within existing aeroelastic software would likewise need to be computationally efficient (e.g. see [18]). Considering the second question, detailed FE models of the drivetrain will commonly be used as part of the wind turbine design process. However, such models may well not be owned by or accessible to the wind farm operator. Despite this, the required spring stiffness values for simplified representations could be requested from the designer/manufacturer given that required parameters are unlikely to be considered sensitive or proprietary. In addition, it may transpire that sensible spring stiffnesses can be identified which allow operators to select appropriate values based on drivetrain dimensions and geometry without requiring access to detailed models. To be clear, the detailed and high quality models used in existing work and outlined in Sections 2.5.2 & 2.5.3 will remain crucial to the study of MB loading and operational behaviour. Rather than seeking to compete with such models, it is instead suggested that there are important synergies. For example, broader studies using simplified models can be leveraged to identify specific load cases requiring more detailed investigation with higher complexity models. Similarly, the MB load outputs of simple representations, obtained from coupling with aeroleastic code, can be used as inputs to more detailed models of bearing internal and external structure, allowing detailed studies to take place while preserving a level of modularity. Therefore, with reference to the third question, it is assumed that a constant torsional stiffness estimation will provide adequate results for the identification of interesting load cases requiring further study with more detailed models. In either case, this assumption will be explored in the next chapter.

It is also important to consider the remaining uncertainties in this approach. The analytical models are evaluated against the more detailed FE models. However, the FE models have intrinsic uncertainties stemming from the assumptions surrounding the gearbox representations, the non-rotating shaft, the system damping, the bearing clearance and the quasi-static assumptions. It is critical to note that the main focus here is to develop fast-acting models which can retain key aspects of bearing load

characteristics to develop a greater understanding of wind turbine main shaft bearing load behaviours. As such, it is understood that these remaining uncertainties may change the exact load values output from the models, however, the general relationships (the main focus of this study) will remain the same.

This chapter has addressed the first research question by methodically deriving a simple and efficient model of a DTRB as a wind turbine main bearing. Throughout the development process the model assumptions were pragmatically assessed and behaviours were validated against a more sophisticated model. The model was then utilised to gain an insight into bearing loading conditions throughout a vast range of operational conditions, creating the initial building blocks towards an answer to the second research question. Finally, this chapter has provided insights into the third research question, since it was shown that the moment action of tapered roller main bearings is significant such that they require a different model representation from a DSRB. While mean force loading on the tapered bearing remained similar to DSRB, DTRB peak force loading was reduced as a result of the presence of moment reactions in addition to force reactions. The DTRB model also proved less sensitive to the turbulence level than DSRB.

Analyses in this chapter demonstrated the existence of large repeating looped structures during significant periods of normal operational conditions where extreme changes in both magnitude and direction of radial forces and moments can occur in short periods of time. It is important to discern the effects of such discovered load structures on internal bearing loading to help build a more complete picture of bearing operational conditions. It is expected that such rapid changes in moment magnitudes on the bearing unit could result in the edge loading of rollers; which in turn could initiate or accelerate failure mechanisms within the bearing. It is thus important to explore the internal loading of DTRBs throughout normal operation and in the presence of these loop structures to generate a greater understanding of the operating conditions of bearing components and detect any negative impacts such structures have on bearing health. This will be the focus of the following chapter.

Chapter 4

An internal load distribution model for tapered roller main-bearings

A new DTRB model with capabilities of outputting internal loading must first be developed before the type of load structures identified in Chapter 3 can be explored further. Keeping in line with the aims and theme of this work, that is, the development of efficient, fast-acting models - a new numerical contact model of a DTRB is developed in this chapter. Having addressed the first research question in Chapter 3, this Chapter will push beyond the aforementioned goals and aim to create a more intricate tapered roller bearing model with the capabilities of determining internal component conditions. As such, this chapter will further address all three research questions.

The extensive literature review in Section 2.5 explored the common modeling methods and existing DTRB models both within and outwith the context of wind turbine main bearings. It was clear from the literature that there are few studies exploring realistic load effects of DTRBs as wind turbine main bearings, and that two main modelling methods exist in this context; (i) the two-step decoupled method, where aeroelastic multi-body models are simulated operating in realistic wind conditions before the hub

loading is extracted and input to a decoupled drivetrain model. (ii) Highly detailed and complex numerical or FE models of DTRBs, including the modelling of internal components. Method (i) is useful for examining main bearing load effects under a variety of realistic load conditions or design load cases. Post processing of the hub loading can also be an efficient process given the decoupling of the drivetrain model from the aeroelastic simulations. The decoupled step also allows for a variety of model types to be used for post processing, depending on the parameters being studied.

The common methods found in the literature for modelling the main bearing in these two-step approaches involved the use of commercial multi-body simulation software such as SIMPACK. While such software packages have extensive functionalities surrounding bearing analysis, the main bearing is often modelled by more simple representations in the literature such as force elements with linear force-deflection relationships. They are also not readily available for use without a payed license and, as they are standalone packages, must always be fully decoupled and cannot be embedded within other software. Method (ii) involves the development of intrinsically complex models such as that created in [81], where the internal components are modelled in detail and bearing and roller load distributions can be determined using iterative mathematical techniques. This model can consider coulomb friction and roller-flange contact forces and also be coupled with an FE model to determine the contact stress distributions across the roller-raceway contact areas. While this model has capabilities of determining the effects of micro-geometries on stress distributions between rollers and raceways, the multiple co-ordinate systems, iterative loops and coupling with FE models increases the computational power required to determine a solution and limit the model use case for simplified bearing loading conditions. Thus, these types of models are not efficient for examining internal bearing loading from hub loading time histories and hence, cannot be used to investigate realistic wind loading effects on the bearing conditions. They cannot, therefore, be used to explore the load impacts on internal bearing components from varying wind conditions.

This chapter, therefore, seeks to bridge the gap between these two modelling methods by

creating an efficient, open-source bearing model with the capabilities of solving internal load conditions for hub-loading time series in a timely manner on a standard desktop PC. The following sections present the model inputs in the form of hub loading data and bearing geometrical details before outlining the steps taken in the development of the new model. Potential model simplifications are then explored in an attempt to keep the model as efficient as possible before the underlying equations for the model are derived. The model was coded in Matlab as a series of functions, with the analytical model developed in Chapter 3 now acting as the initial function of the numerical model to determine the bearing loads from the hub load inputs. An optimiser is then used to determine the inner race displacements under static equilibrium. The numerical model has non-linear, cross-coupled stiffness capabilities and thus the effects of the constant stiffness estimation used in the analytical model are considered. A new method of developing varying-stiffness capabilities is then presented and the results are compared with the constant stiffness assumptions. The model is then used to explore the effects of the load structure types presented in Chapter 3 on the internal bearing components.

4.1 Model Inputs

The inputs to the model include hub loading, basic drivetrain dimensions and gearbox equivalent spring stiffnesses (as per Chapter 3), and bearing geometries. The hub loading data sets used in this chapter are derived in the same manner to the hub loading data sets previously utilised. The data sets used in Chapter 3 cannot be used in this body of work as the rotational speed data for the rotor was missing; a vital parameter used to track the trajectories of rollers around the bearing circumference.

The hub loading data sets are derived from fully aeroelastic 10-minute simulations of a 1.5MW turbine, performed in realistic 3-dimensional turbulent wind fields in the Bladed software. The wind fields have medium turbulence intensity values as specified by [36] and shear exponents of 0.2. Hub height mean wind speeds were varied between 12, 14, 18 and 24m/s; the parameter used to differentiate between each wind field. As the wind files generated here are predominantly used to assist the development of new

modelling capabilities, only one random seed was generated for each hub-height mean wind speed providing a total of 4 wind fields used in this Chapter.

The input parameters determined for the analytical model in Chapter 3 were adjusted to accommodate specific bearing dimensions in this body of work. More specifically, the diameter of the main shaft and the torsional stiffness values used to represent the bearing and bearing housing were altered. The horizontal and vertical torsional spring stiffness values estimated previously differed in magnitude as the model considered the stiffness of the bearing housing which is asymmetrical. As the bearing housing is not considered for the numerical model, and double row tapered roller bearings are symmetrical about the axis of rotation, the same stiffness value was used to represent the torsional stiffness in both planes. The previously estimated torsional stiffness value (from the vertical plane) of 145MN/rad was used as an initial estimate for both stiffness values here.

The bearing used in this study is the SKF 331555B double inner tapered roller bearing. The appropriate technical data, including some geometries required for input to the model, can be found in Table 4.2. This bearing was selected for study as the dimensions closely matched that of a DSRB used as the main shaft bearing in wind turbines of a similar size.

Table 4.1: Technical data of SKF bearing 331555B.

Variable	**Symbol**	**Value**
Bore diameter	d	635 (mm)
Outer diameter	D	939.8 (mm)
Bearing width over outer rings	T	304.8 (mm)
Bearing width over inner rings	B	304.8 (mm)
Inner race min diameter	d_1	696 (mm)
Outer race min diameter	D_1	789(mm)
Basic dynamic load rating	C	6710 (kN)
Basic static load rating	C_0	16600 (kN)
Fatigue load limit	P_u	1100 (kN)

The new internal bearing model will be created in such a way that standard manufacturer geometries of different DITRBs can be input by the user and the model will automatically adjusts for the new dimensions. The internal model will input time series hub loading parameters F_x, F_y, F_z, M_y, M_z, rotor speed, Ω, and various geometrical bearing and drivetrain data. Various functions determine the loads on the bearing and track the trajectory of the rollers around the two races before the solver balances the forces and moments across the bearing unit to determine the axial, radial and angular displacements on the inner race. The displacement results can then be passed through one of the model functions to determine the distributed bearing and distributed roller loads at each time step.

4.2 Methodology

This section explores what simplifying assumptions may be used in order to develop a model with improved computational efficiency. Underlying equations for a new internal bearing model are then derived before the assumptions and limitations are discussed. The effects of the constant torsional stiffness estimation in the analytical model are then explored and a method to introduce varying-stiffness capabilities in the new model is presented. The loading effects of varying the stiffness are then investigated.

4.2.1 Improving Model Efficiency

As this study sought out to create a fast and efficient internal model of a DTRB, the first step before deriving the model was to determine if the number of degrees of freedom can be reduced. Classically, models of this type have five degrees of freedom accounting for lateral movement and rotation about the z axis (vertical axis), lateral movement and rotation about the y axis (horizontal axis), and lateral movement about the x axis (axial axis) [35, 41, 71, 81]. This involves all bearing movement except for rotational torque and results in 5 components of loading and displacement.

Such models typically use mathematical iterations such as the Newton-Raphson method

to solve for each of the displacement components, where the required computational power is increased with each unknown parameter which must be solved for. It is proposed in this model that the horizontal and vertical axes are combined to create one radial axis, reducing the number of unknowns in the system from 5 to 3 and thus, enhancing the computational performance of the model. As the maximum displacement caused by force loads occurs at the angle of the applied load, and the maximum displacement resulting from moment loads occurs 90 degrees from the angle of the applied moment; the y and z axes can be combined to create one radial axis that separately tracks the angles of applied forces and moments without losing any information. Four displacements, lateral and angular in both the horizontal and vertical axes, are therefore, replaced by one radial displacement, δ_r, and one angular displacement, δ_θ. This modification can only be undertaken when considering on-design bearing loads. That is, combining the horizontal and vertical axes removes the ability of the model to study additional effects such as bearing misalignment. Given that the focus of this work is to explore the effects of applied bearing loads under normal operation, and that the effects of misalignment have been previously studied and are well understood [2, 72, 82], this is deemed a valid simplification for the desired goals of this work.

Highly detailed bearing models ignore bearing rotation during load analyses to simplify simulations and improve the run time. Likewise, Hart solves for internal load distributions in a decoupled manner from load direction and bearing rotation in [28] to simplify the modelling approach. In [28], radial load directions entirely dictated the direction of maximum deflection. This allowed for the rotation of load distribution results, once solved, to account for the load direction. It may be possible to employ the same methods here to simplify and increase the efficiency of the new DTRB internal model. However, unlike the DSRB in [28], DTRBs react moment loads as well as radial force loads and thus, this method would only be feasible if the maximum displacement resulting from force and moment loads are acting in the same direction throughout the hub loading time series.

Therefore, the direction of radial force and moment loads acting on the bearing were

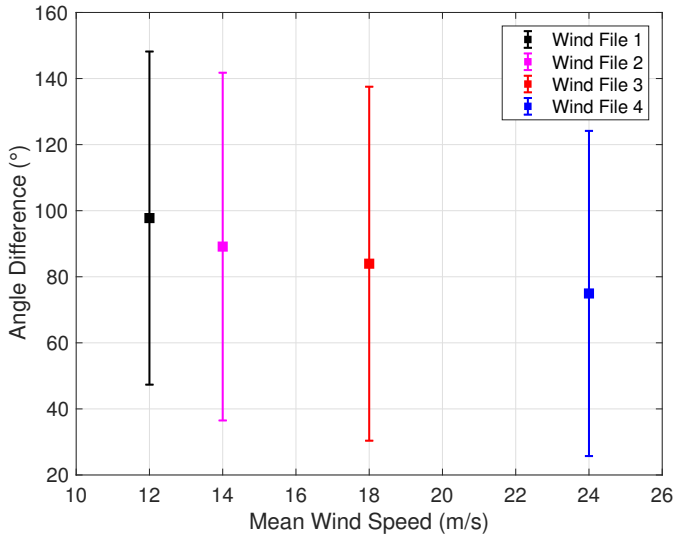

Figure 4.1: Plot displaying the mean and standard deviation of the angle between the applied force and moment to the bearing for all time steps in four different wind files.

analysed using the DTRB analytical model to determine if the numerical model could be simplified further. The angle difference between the force and moment loads at the bearing were determined across the 10 minute time series for each of the four new wind files and the mean and standard deviations of the results are plotted in Figure 4.1. While the mean angle differences between the force and moment loads remains close to 90 degrees across the operating points, the large variations signified by the standard deviation plots show that the model cannot be simplified further by ignoring load directions during model simulation. The direction of both force and moment loads, along with the trajectory of rollers around the raceways must be continually tracked and the combined displacement effects determined at each time step during model simulation.

The results presented in Figure 4.1 echo that of the results presented in Figures 3.17 & 3.18 where moment polar plots were shown to be unconcentrated around the bearing circumference while force loading was concentrated in the direction of rotor mass at 270 degrees. While the rotor mass is the main driver for the direction of force loads on wind turbine main bearings, the results here suggest that the rotor mass is not so influential on the direction of moment loads experienced by the bearing. These results

help to improve our understanding about the relationships between the loads in this system, highlighting that force and moment loads on main shaft bearings are driven by different aspects of wind interactions.

Wind turbine main shaft bearings are typically grease lubricated and therefore more likely to be operating under starved conditions [25]. As such, the pressure distribution across the rollers likely conforms closely to that of dry Hertzian contact [31] and so the model can be simplified further by ignoring the effects of lubrication. It is necessary to include the impacts of lubrication when considering possible metal-to-metal asperity contact and dynamic slip behaviour [14]. However, neither of which are the focus of this work, and thus, ignoring the effects of lubrication is considered valid here.

4.2.2 Deriving the Numerical Model

Having determined a method in which to simplify the model by reducing the number of degrees of freedom and therefore, the number of unknowns in the system, the equations detailing the inner race displacements can now be derived. This section introduces model assumptions before detailing how the horizontal and vertical planes are combined into the one radial plane. The displacement equations are then derived in full.

A number of simplifying approximations were made to further improve the computational speed of the model. As the taper angle of the rollers, and thus the angle difference between the inner and outer raceway, is small, tapering on the rollers is neglected and the mean of the inner and outer contact angles (displayed in Figure 4.4) is used in calculations. This same approximation was used in [80] where model results were validated against FE results and found to be similar. The contact angle is also assumed to remain unchanged during deformation and bearing misalignment, clearance, roller-flange contact forces and rotational friction are all assumed to be zero. Rollers are also distributed uniformly around the circumference of the bearing and assumed to travel with pure rolling, i.e, sliding of rollers is neglected. The effects of cage forces, roller skewing and the preload of rollers is also neglected.

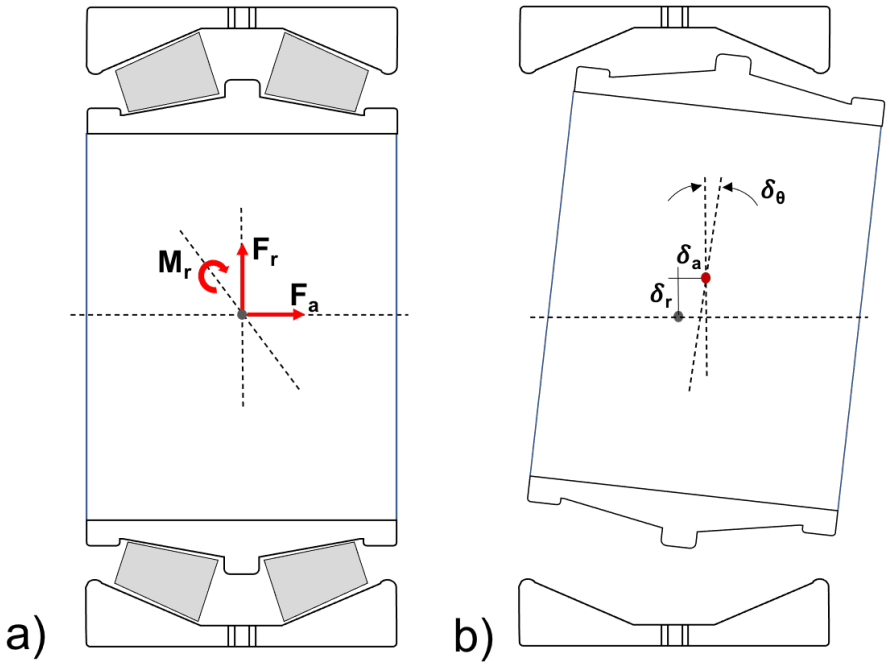

Figure 4.2: a) Image depicting the type of loads that DTRBs can react; radial moment, M_r, radial force, F_r, and axial force, F_a. b) Image displaying the type of displacements resulting from the loads shown in a).

Figure 4.2a) shows a side view of a double-row tapered roller bearing displaying the axial, radial and moment loads at the centre point of the bearing. Figure 4.2b) then displays the appropriate axial, radial and angular displacements occurring from such loading. Figure 4.3 then displays a front view of the bearing, indicating how a radial load resulting from a radial displacement is distributed across the rollers. This plot also shows how displacement varies from the angle of applied displacement. While the slicing technique is commonly used to determine the effects of misalignment, and misalignment cannot be studied using the developed model, there are still benefits to employing the slicing technique here. As applied moments result in angular rotations of the inner race, they essentially cause the same type of loading seen from bearing misalignment. The slicing technique will therefore provide the model with capabilities of determining distributed roller loads and help develop a greater understanding of how the moment loads in the wind turbine system effect the internal components of the main shaft bearing. Figure 4.4 displays a simplistic depiction of the slicing technique, showing

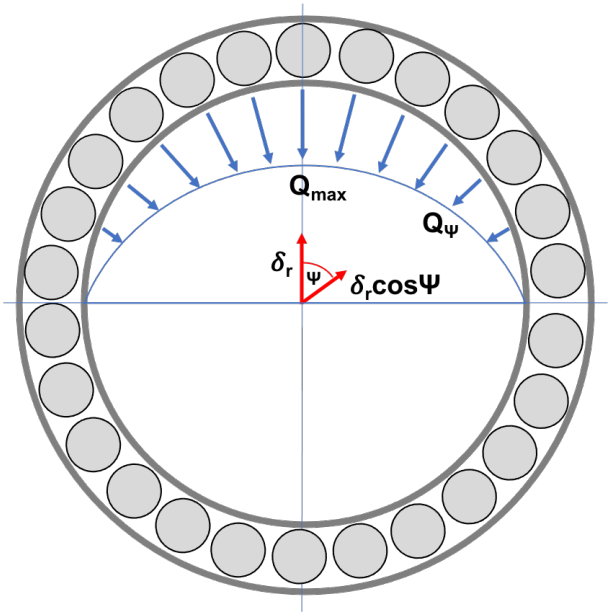

Figure 4.3: Front view of the bearing portraying how the displacement and resulting loads vary around the circumference.

how the roller is 'sliced' in laminae across the roller length, x. Figure 4.4 also displays the mean roller contact angle, α, used in calculations for this model and how the roller lamina load, q_k, may vary across the roller length. The roller was sliced into 30 laminae as per recommendations from [39]. Figure 4.5 displays how an angular displacement of the inner race results in additional axial and radial displacements at the centre of the roller. Different magnitudes of additional axial and radial displacements occur along the roller length due to the varying vertical and horizontal distances at each point along the roller, further highlighting the importance of the slicing technique when analysing the effects of moment loads.

As the horizontal and vertical axes (y and z) were combined to create one radial axis, the method for tracking the direction of the force and moment loads on the bearing, and subsequently determining the location of maximum displacements around the radial axis (circumference of the bearing) must first be distinguished. Figure 4.3 displays how the magnitude of radial load varies around the circumference of the bearing relative to the direction of applied displacement, δ_r. As maximum radial displacement occurs at the angle of applied radial force, ψ_F, the displacement at any given roller at angle ψ_i

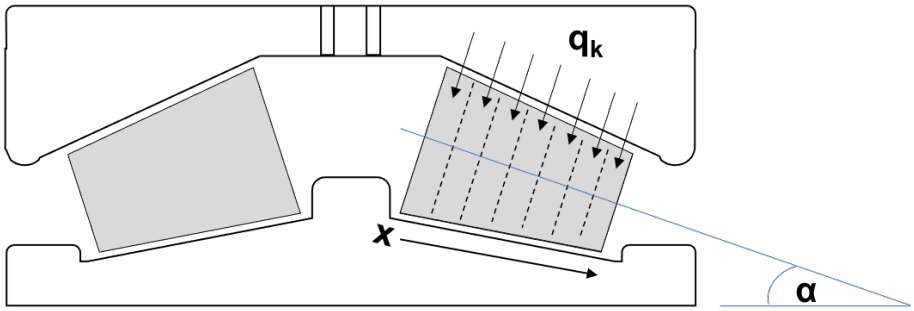

Figure 4.4: Split view image of bearing depicting the mean contact angle, α, and how the roller is divided into laminae/slices.

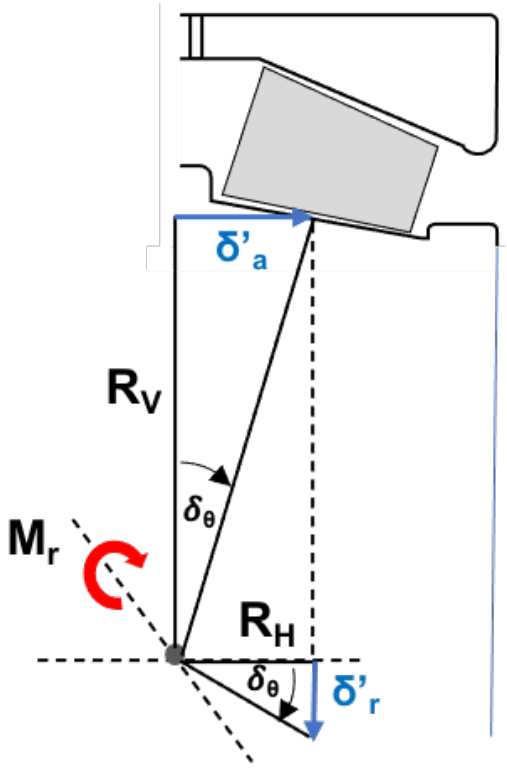

Figure 4.5: Image displaying how an applied moment to the inner race results in additional axial, δ'_a, and radial, δ'_r displacements.

around the circumference can be determined by $\delta(\psi_i) = \delta_r cos(\psi_i - \psi_F)$. This equation holds true for both roller rows as an isolated radial displacement will effect both rows of rollers equally. More care must be taken when determining the maximum angular displacement, δ_θ, induced by a moment load. Firstly, let us consider only roller row 2, that is, the roller row on the right hand side of Figure 4.2a). If a positive angular

rotation is defined as a clockwise rotation of the inner race (and for now, assuming this is the only displacement being applied), the maximum angular displacement will occur at an angle 90 degrees less than the angle of applied moment, ψ_M, and displacement terms resulting from moment loading will be multiplied by $cos(\psi_i - (\psi_M - \frac{\pi}{2}))$. It is important to note that a maximum magnitude angular displacement will also occur at an angle 90 degrees greater than the angle of applied moment. However, this displacement occurs in the opposite direction (i.e has an opposite sign) and, in roller row 2, will not result in loads being reacted by the rollers. In complex load conditions where the inner race has been axially, radially and angularly displaced, this effect will reduce roller loads. Considering a global coordinate system, these effects will be reversed in roller row 1 where the maximum compression causing displacement will occur at an angle 90 degrees greater than the angle of applied load. This effect is accounted for in the model.

When the inner race is displaced by δ_a and δ_r and rotated by δ_θ, displacement occurs at the mid point of the roller. The displacement caused by δ_a and δ_r is

$$\delta(\psi) = \delta_a sin(\alpha_m) + \delta_r cos(\alpha_m) cos(\psi - \psi_F) \tag{4.1}$$

The inner race rotation, δ_θ, causes an additional axial, δ'_a, and radial, δ'_r, displacement, maximum when $\psi_i = (\psi_M - \frac{\pi}{2})$, derived as

$$\delta'_a(x) = R_V(x) tan(\delta_\theta) \tag{4.2}$$

and

$$\delta'_r(x) = R_H(x) tan(\delta_\theta) \tag{4.3}$$

Where R_V and R_H are the vertical and horizontal radii of the inner race which varies across the length of the roller, x. Using small angle approximation we get

$$tan(\delta_\theta) \approx \delta_\theta \tag{4.4}$$

therefore,

$$\delta'_a(x) = R_V(x)\delta_\theta \tag{4.5}$$

and

$$\delta'_r(x) = R_H(x)\delta_\theta \tag{4.6}$$

As R_V varies along length of the roller, x, and maximum displacement caused by rotation will be seen at angle $(\psi_M - \frac{\pi}{2})$

$$\delta'_a(\psi_i, x) = R_V(x)\delta_\theta cos(\psi_i - (\psi_M - \frac{\pi}{2})) \tag{4.7}$$

and since we want to project this onto the mean contact angle, α_m, then

$$\delta'_a(\psi_i, x) = R_V(x)\delta_\theta sin(\alpha_m)cos(\psi_i - (\psi_M - \frac{\pi}{2})) \tag{4.8}$$

Similarly, projecting the additional radial displacement, δ'_r, onto the mean contact angle and distributing about the circumference (where maximum displacement occurs at axis of rotation) gives

$$\delta'_r(\psi_i, x) = R_H(x)\delta_\theta cos(\alpha_m)cos(\psi_i - (\psi_M - \frac{\pi}{2})) \tag{4.9}$$

δ'_a and δ'_r are both functions of x, the length along the roller, and ψ, the angle around the circumference of the bearing. Adding the displacement from axial, radial and angular movement of the inner race gives a total displacement of

$$\delta(\psi, x) = \delta_a sin(\alpha_m) + \delta_r cos(\alpha_m)cos(\psi - \psi_F) + \delta'_a(\psi, x) - \delta'_r(\psi, x) \tag{4.10}$$

or

$$\begin{aligned}\delta(\psi, x) = \delta_a sin(\alpha_m) + \delta_r cos(\alpha_m)cos(\psi - \psi_F) + R_V(x)\delta_\theta sin(\alpha_m)cos(\psi - (\psi_M - \frac{\pi}{2})) \\ - R_H(x)\delta_\theta cos(\alpha_m)cos(\psi - (\psi_M - \frac{\pi}{2}))\end{aligned} \tag{4.11}$$

Collecting like terms gives

$$\delta(\psi, x) = \delta_a sin(\alpha_m) + \delta_r cos(\alpha_m) cos(\psi - \psi_F) + \delta_\theta cos(\psi - (\psi_M - \frac{\pi}{2})[R_V(x) sin(\alpha_m) - R_H(x) cos(\alpha_m)] \tag{4.12}$$

and simplifying the cos term

$$\delta(\psi, x) = \delta_a sin(\alpha_m) + \delta_r cos(\alpha_m) cos(\psi - \psi_F) - \delta_\theta sin(\psi - \psi_M)[R_V(x) sin(\alpha_m) - R_H(x) cos(\alpha_m)] \tag{4.13}$$

Now that the displacement at the roller has been derived, the roller reaction force can be calculated using

$$Q_{\psi_i} = \delta^{1.1} K \tag{4.14}$$

where i indicates the roller number. Equation 4.14 assumes line contact between the roller and raceways and is derived from experimental results [26]. K is the line contact factor which is dependent on bearing geometries and used to represent the contact stiffness between the rollers and raceways and determined by

$$K = 6.39E10 L^{0.991} D^{0.1034} \tag{4.15}$$

where L is the length of the roller and D is the diameter of the roller in meters as defined in [35]. Equation 4.15 was derived empirically and eliminates the need for highly computationally expensive contact pressure analysis [35].

Having derived the reaction force at each roller, the total axial reaction force on the raceway is

$$Q_a = \sum_i Q_{\psi_i} sin(\alpha_m) \tag{4.16}$$

the radial reaction force is

$$Q_r = \sum_i Q_{\psi_i} cos(\alpha_m) cos(\psi_i - \psi_F) \tag{4.17}$$

and the total moment reaction is

$$M_R = \sum_i \sum_x [Q_{a_i} sin(\alpha_m) R_V(x) - Q_{r_i} cos(\alpha_m) R_H(x)] cos(\psi_i - (\psi_M - \frac{\pi}{2})) \tag{4.18}$$

The equations outlined above describe the inner race displacements and resulting reaction forces on the rollers for one raceway only, the downwind race. The equations were duplicated and the axial and angular displacements negated to create a new set of equations that represent the upwind race. As the model developed here is quasi-static, that is, that each time step in the time loading history is treated as individual static load cases, the bearing must be in equilibrium at each time step such that

$$|F_a - (Q_{a2} - Q_{a1})| + |F_r - (Q_{r2} + Q_{r1})| + |M_A - (M_{R2} - M_{R1})| = 0 \tag{4.19}$$

Where F_a is the applied axial load on the bearing unit, F_r is the radial force load applied to the bearing unit, M_A is the moment load applied to the bearing unit and Q_a, Q_r and M_R are the total axial, radial and moment reaction loads of the races, with number 2 representing the downwind race and number 1 representing the upwind race.

A summary of the model process is as follows: hub loads and rotor speed are extracted from aeroelastic simulations and input along with bearing and drivetrain geometries into the numerical model. The hub loads (in horizontal, vertical and axial planes) are passed through the analytical model function which determines the magnitude and direction of loads at the bearing unit (in axial and radial reference frames) and the rotor speed is passed through a roller geometry function which determines the location of the rollers around the raceways at each time step. The loads on the bearing and the roller positions are then passed through the equations outlined above with functions representing each race of the bearing. A final function which represents

the displacements and loads at each race and also the equilibrium equation above is then passed through an optimiser which determines which axial, radial and angular displacements of the inner race balances the loads across the bearing.

4.3 Effects of Model Stiffness

As mentioned in the opening statement of this chapter, the analytical model developed in Chapter 3 acts as the first function within the new model to determine bearing loads from the aeroelastic hub loading outputs. Only then can the inner race displacements be calculated by the solver, which balances the bearing loads across the unit. However, as discussed in Chapter 3, the analytical model has constant torsional stiffness assumptions, whereas the internal model developed here has intrinsic varying stiffness capabilities. As internal components are included here, different numbers of rollers and different roller sections/lamina are engaged in load response under different conditions; ultimately varying the stiffness of the bearing unit depending on the load conditions present. Roller lamina also have non-linear force response behaviour which can be interpreted as a linear response with a deflection dependant stiffness, ie. there is an effective stiffness of $K_{eff} = \delta^{0.1}K$ in Equation 4.14. Solving for the axial, radial and angular displacements simultaneously also ensures that all bearing motion is considered when the forces and moments are balanced across the system. The cross-coupled stiffness components (or off-diagonal stiffness components) are therefore considered at each time step in this model. This disparity between the modelling of bearing stiffness at the drivetrain and bearing unit stages must be investigated to explore the effect of the constant stiffness assumptions. This section aims to do just that. A method for incorporating varying stiffness capabilities within the analytical model function is then explored.

The torsional stiffness of the numerical bearing model was first investigated under various load conditions using the constant stiffness assumption in the analytical model function. The model described in Chapter 3 considered the asymmetrical bearing housing and thus, different torsional stiffnesses were determined for the horizontal and vertical

torsional springs. As the numerical model considers the main shaft bearing without the housing, the horizontal and vertical torsional spring stiffnesses in the analytical model function must be equal as DTRBs are symmetrical. The vertical torsional spring stiffness estimation of 145MN/rad in Chapter 3 was used as an initial guess for the stiffness value of the SKF bearing in both planes. The four example hub loading time series described in this chapter were run through the model and the axial, radial and angular displacement results were stored. The displacement results were then used to gauge approximate minimum, mean and maximum axial and radial displacements and a range of angular displacements. Multiple displacement scenarios, detailed in Table 4.2, were then generated where the axial and radial displacements are fixed and each scenario includes the full range of angular displacement values. Axial and radial displacements are considered in this study as the numerical model has cross dependent stiffness capabilities ie. the off-diagonal values in the stiffness matrix are non-zero and axial and radial displacements will effect the overall stiffness of the bearing.

Table 4.2: Displacement Scenarios

Scenario	δ_a	δ_r
1	0	0
2	min	0
3	max	0
4	0	min
5	0	max
6	min	min
7	max	max
8	mean	mean

Each displacement scenario was applied to the numerical model and the total moment reaction load was determined throughout the range of angular displacement values. Load (moment) vs displacement plots were then generated for each of the different scenarios and are displayed in Figure 4.6a). It is clear from Figure 4.6a) that the varying combinations of displacements can have large effects on the resulting moment

across the bearing. This is especially true for scenario 7 where the axial and radial displacements are held at their maximum values. It can also be seen that a number of the plots somewhat converge as the angular displacement values increase to the maximum end of the range.

Stiffness vs moment plots were then determined for the various load conditions using the load vs displacement plots and Equation 4.20. The operational stiffness can be estimated by linearly interpolating between the relevant values on the correct stiffness vs moment plot under static loads. The stiffness vs moment plots corresponding to the various scenarios described above are displayed in Figure 4.6b) where clear variations can be seen in the results of the different displacement scenarios.

$$K_\theta = \frac{\Delta M}{\Delta \delta_\theta} \tag{4.20}$$

A linear 'best fit' plot of the 8 displacement scenarios was generated and added to the load vs displacement plot in Figure 4.6a). A linear fit was selected as this would provide a 'best fit' constant stiffness estimation (ie. the gradient of the straight line fit) when the coinciding stiffness vs moment plot is determined, which has been added to Figure 4.6b). Initial analysis of the 'best fit' constant stiffness estimation reveals that the initial estimate of 145MN/rad was underestimated by approximately a factor of 10. Such discrepancy between the two determined stiffness values is likely due to the fact that the stiffness value used in the analytical model was determined via the FE model which included bearing housing flexibility, whereas the numerical model only models the stiffness between rollers and raceways. It is also evident from Figure 4.6b) that the varying stiffnesses obtained from the numerical model stray significantly from the constant stiffness trend line. Therefore, the effects of the constant stiffness assumption in the analytical model stage must be explored to determine the effects on bearing loads.

It is important to remember that the 8 displacement scenarios tested here are not indicative of actual bearing conditions during realistic loading and have been artificially created by using minimum, mean and maximum axial and radial displacements seen

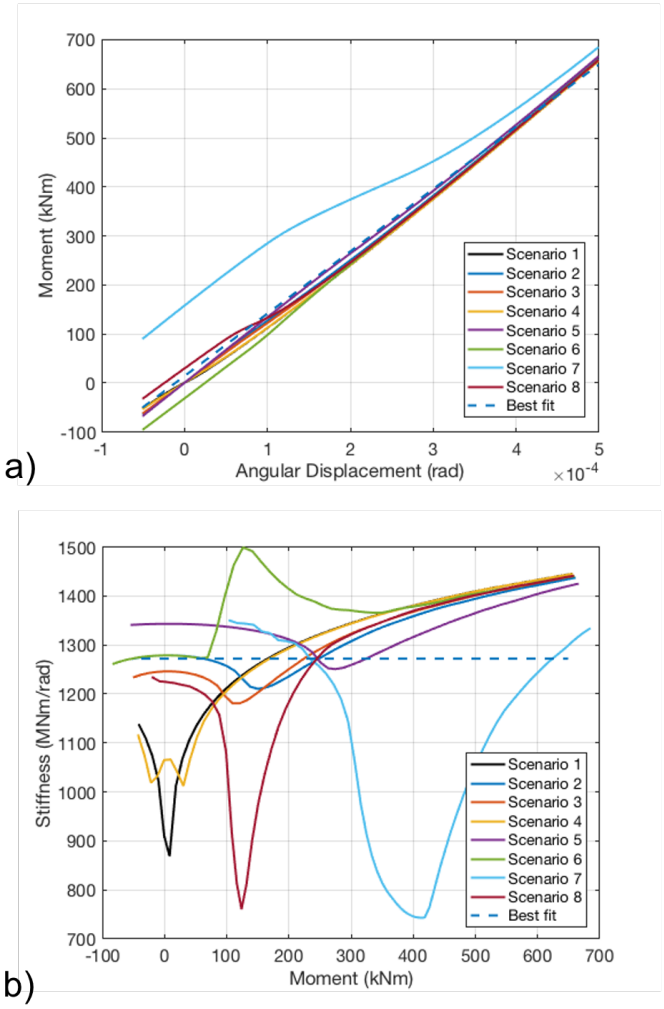

Figure 4.6: a) The moment vs angular displacement plots for varying sets of axial and radial displacement conditions. b) The torsional stiffness vs moment plots for varying sets of axial and radial displacement conditions.

from a variety of operating conditions. In other words, the maximum radial displacement of the inner race may not occur at the same time as it is maximally axially displaced. As these conditions (Scenario 7) have produced almost anomaly-like trend lines when compared to the other scenarios, a study was undertaken to determine if the bearing is likely to experience these conditions under normal operation.

The correlation of axial and radial displacements was therefore investigated for the four realistic hub loading files while the torsional stiffness in the analytical model stage

remained constant, now with the best fit stiffness of 1272MN/rad in both planes. The results from wind files 1 and 2 (12m/s and 14m/s mean wind speeds, respectively) are displayed in Figure 4.7, the other 2 wind files produced similar results. It's clear from Figure 4.7 that axial and radial displacements are well correlated and that maximum axial and radial displacements are likely to occur at the same time. These plots confirm that displacement scenario 7 cannot be neglected when creating a best fit stiffness vs moment plot. As it appears a best fit curve doesn't necessarily accurately represent the full range of displacement scenarios, a method was developed to vary the stiffness in the analytical model function to match that of the numerical model at each time step.

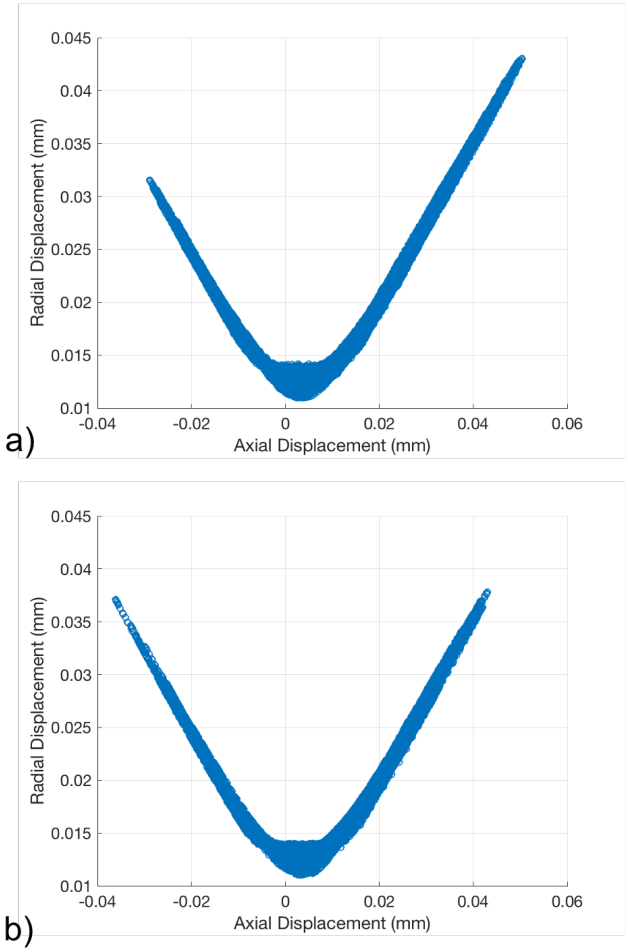

Figure 4.7: The correlation between axial and radial inner race displacement for 10-minute simulated hub loading with a mean hub height wind speed of a)12m/s and b)14m/s.

4.3.1 Incorporating varying stiffness capabilities at the analytical model stage

While the analytical DTRB model was originally equipped with a constant torsional stiffness estimation, the analysis above details how this may not be accurate for use in the numerical model which has varying stiffness capabilities. As displayed above, constant stiffness values may not provide accurate estimations across every load scenario seen by the bearing and could lead to inaccuracies in the resulting forces and moments acting on the bearing. If varying stiffness values in the analytical model is to be achieved, the analytical model function must be incorporated into a loop that runs through each time step in the hub loading history where a new stiffness value is selected at each time step which is representative of the bearings current displacement. An iterative loop was then created within this time step loop using the stiffness determination method detailed in the previous section at each iteration until stiffness values converge. This iterative loop process is outlined in Figure 4.8 which displays the model process.

The hub loading time series from aeroelastic simulations, drivetrain geometries and bearing geometries are input by the user. The geometries and rotor speed data are then passed through a roller positions function which outputs the position of all rollers around the raceway at each time step throughout the loading history. Geometry input data is also passed through a geometry function which determines the horizontal and vertical radii from the centre of the bearing to the inner race, R_H and R_V, which vary along the length of the rollers, the roller to raceway contact stiffness, kc, and the mean contact angle, α_m. The hub loading inputs and outputs of the two functions used thus far are then input to a loop which loops through the analytical model function, the numerical model function, an optimiser and the iterative loop for each time step. An initial torsional stiffness value is assumed and applied to the analytical model along with the hub loading data. The model outputs the magnitude and directions of the axial, radial and moment loads on the bearing unit under these initial torsional stiffness assumptions. The analytical model, roller position function and geometry function

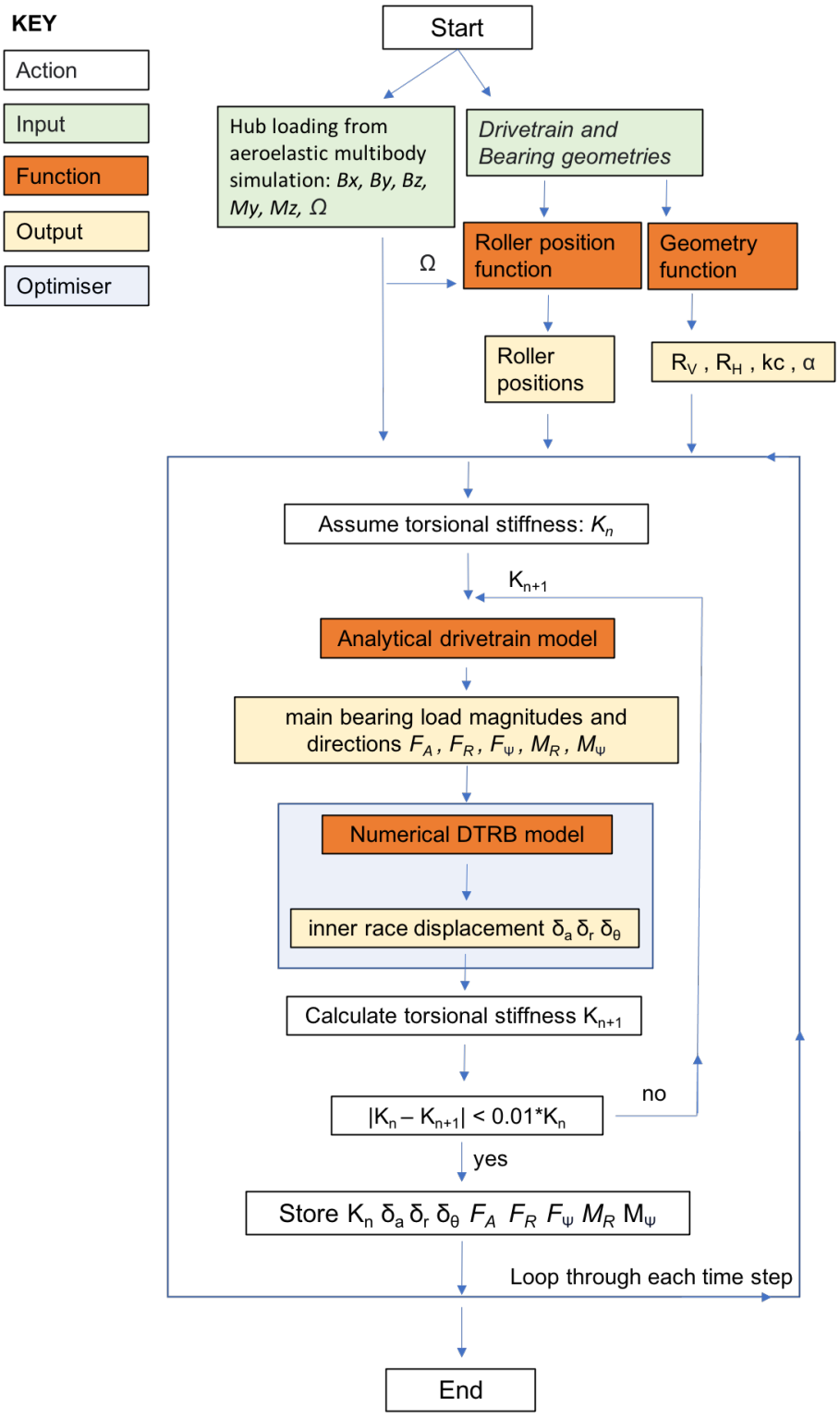

Figure 4.8: Flowchart of the numerical model

outputs are then input to the numerical model function which includes the equations derived in Section 4.2.2 and an optimiser is used to solve for the axial, radial and angular displacements of the inner race. The displacements are then used to determine the torsional stiffness of the bearing under the current load conditions using the methods outlined in Section 4.3 and the new stiffness value is compared with the original estimation. If the new stiffness value is greater than 1% different from the initial estimate then the calculated stiffness is used as the new stiffness guess and the process repeats until the new calculated stiffness has converged within 1% of the previous guess. Once convergence has been achieved the outputs of the two models are stored and the hub loading from the next time step is applied with the previous converged stiffness value being used as the initial estimation.

4.3.2 Load Effects of Varying the Analytical Model Stiffness

With the new model being adapted for varying stiffness capabilities at the TRB analytical model stage, an analysis was undertaken to determine the resultant effects of this adaptation on the bearing unit loads. The four hub loading data sets were passed through the numerical model with a constant analytical-stage torsional stiffness of 1272MN/rad, the 'best-fit' constant stiffness determined in Section 4.3, and with varying stiffness capabilities determined with the iterative loop detailed above. The radial force and moment loads on the bearing unit were determined across the full time histories of the four wind files used in this chapter. A percentage difference method was used to determine the difference in force and moment loads at each time step across the four wind files between the constant and varying stiffness models. The mean and standad deviations between the models was then calculated and the results are plotted in Figure 4.9.

Figure 4.9 shows that the mean difference between the force results of the two models remains less than 1% across the four wind files with low variations indicated by the minimal standard deviations. The standard deviations between the force results indicates that the difference between the constant and varied stiffness models remains

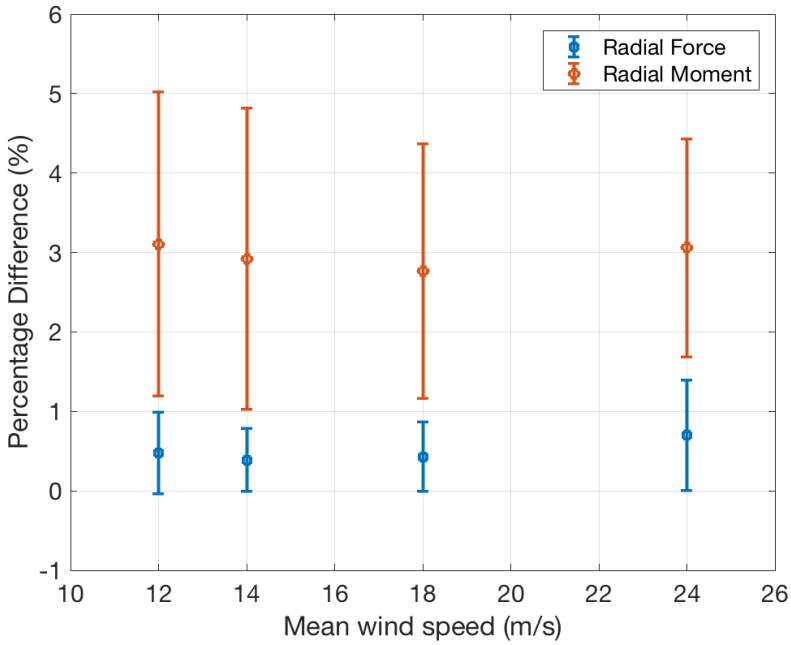

Figure 4.9: Mean and standard deviations of the percentage difference between the force and moment load results of the constant and varied stiffness models.

within 2% across the whole hub loading time histories. The mean difference between the moment results is a bit higher, sitting around 3% across the four wind files. The variation in the moment loads is also greater than that of the force loads with standard deviations indicating that the majority of time steps will fall within 8% of each other.

Example time histories of the radial force and moment results have also been plotted to visually display the discrepancy between the two models. The plots are presented in Figures 4.10a) and 4.10b) and display a period of 14 seconds of loading from wind file 1 (12m/s mean wind speed). The radial force results are displayed in Figure 4.10a) where the best fit model can be seen to match the results of the varying stiffness model quite well. The best fit constant stiffness model slightly overestimates the peak loads within the first few seconds of loading and then slightly underestimates the loads numerous times throughout the rest of the example series. The moment results are plotted in Figure 4.10b) and also show the best fit constant stiffness model underestimating the magnitude multiple times.

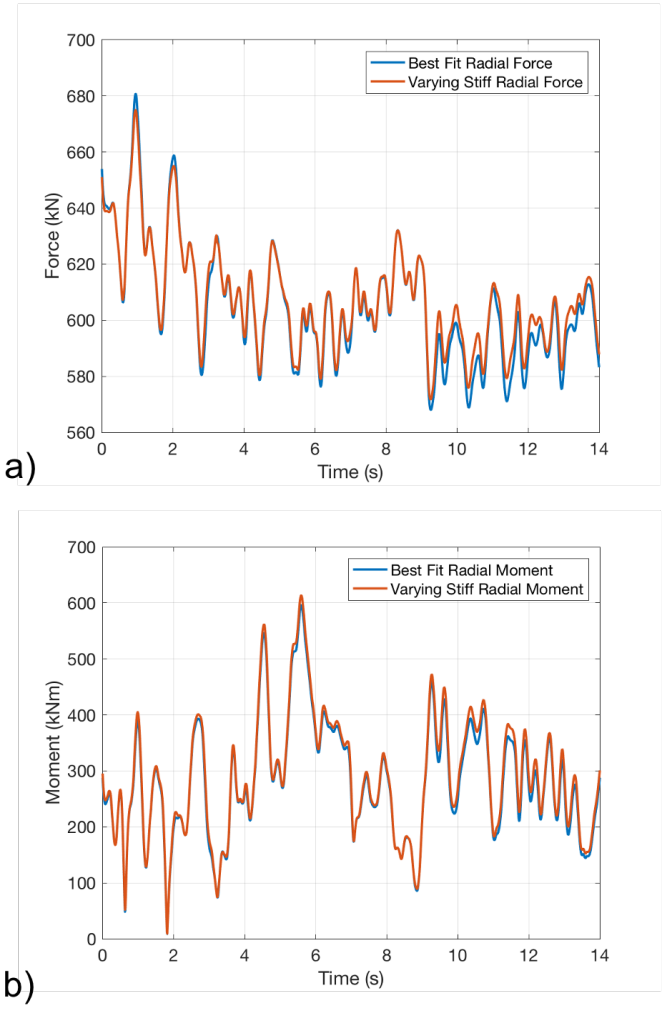

Figure 4.10: Example time series plots displaying the force(a) and moment(b) reaction loads at the bearing unit between the 'best-fit' constant stiffness assumption and the varying stiffness values from the wind file with a hub-height mean wind speed of 12m/s.

This discrepancy between the results of the two models suggests inaccuracies associated with using a constant stiffness estimation for the analytical model stage. It is likely that the constant torsional stiffness assumption will result in both over and underestimations of the loads experienced by the bearing by up to around 8% in the moment loads and 2% in the force loads. However, while the loads may vary by up to 8% at various time steps, the overall trend of results is well matched by the best fit constant stiffness assumption model. The constant stiffness assumption may well prove useful in circumstances where computational time is an important factor or where load trends and cycles are more

important than exact load values. However, it is expected that the difference in load values for individual rollers or slices between the constant and varying stiffness methods may be larger than that of the total bearing loads. For this reason, an example time series plot of the total roller loads on rollers 1 from both races are compared between the best fit constant stiffness and varying stiffness methods and displayed in Figure 4.11.

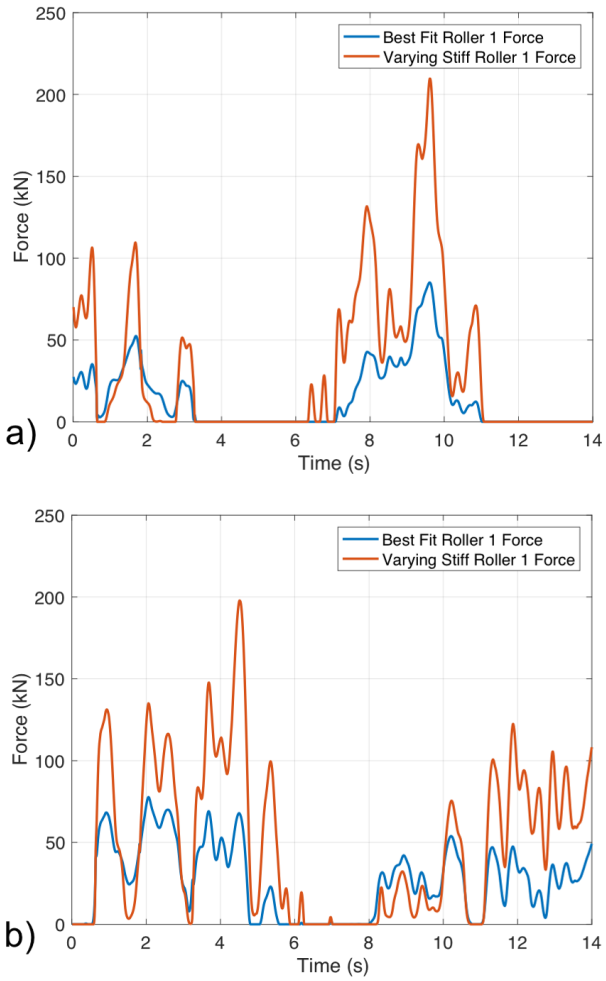

Figure 4.11: Example time series plots displaying the loads on rollers 1 for (a) the upwind and (b) the downwind race between the 'best-fit' constant stiffness assumption and the varying stiffness values from the wind file with a hub-height mean wind speed of 12m/s.

The results displayed in Figure 4.11 show significant disparities between the roller loads

of the constant and varying stiffness methods. These results display the importance of employing the varying stiffness method when performing internal analyses of the bearing as peak roller loads in the varying stiffness results are more than double that of the constant stiffness assumption results. The varying stiffness method is therefore employed throughout the rest of this work when analysing load conditions using the new numerical model.

4.4 Bearing Displacement Drivers

While Figures 4.7a) and 4.7b) provided insight into understanding when the inner race is maximally axially and radially displaced, it is also clear from the plots that the bearing is negatively axially displaced for significant periods of time during operation. This is interesting considering the presence of constant thrust loads on the bearing throughout the hub loading time series. An analysis was therefore undertaken to uncover the drivers for bearing displacement and determine the cause of these unexpected results.

The correlation between axial displacement and the total axial, radial and moment loads on the bearing was first explored in an attempt to find the driver of the negative axial displacements. The results of the correlation assessment between the axial displacement and the axial loads (thrust loads) are displayed in Figure 4.12a) and surprisingly show that no correlation is present. The results between the axial displacement and radial loads is presented in Figure 4.12b) and a clear negative correlation is present. That is, the axial displacement is negative when radial loads are greater and the inner race becomes more positively displaced in the axial direction as the radial loads reduce. The results between the axial displacement and moment loads on the bearing are plotted in Figure 4.12c) and show a slight negative correlation during negative axial displacement and a slight positive correlation during positive axial displacement.

In order to understand these results and why the axial displacement is most correlated to the radial load on the bearing, it is important to first consider what drives the radial loading on the bearing. It was discovered in Chapter 3 that mean radial loads reduced

with increasing wind speed and that high shear profiles resulted in lower radial loads on the bearing. It was hypothesised that higher wind speeds and higher wind speed gradients across the rotor were causing an overturning moment on the rotor, somewhat lifting the weight of the rotor and reducing the radial loads seen by the bearing. If this hypothesis is correct and radial loads are driven by the moments on the rotor, and axial displacement is correlated with the radial load, then the axial displacement itself must be driven by the moments on the rotor. As the correlation between the axial displacement and the total moment load across the bearing were somewhat inconclusive, the correlation between the axial displacement and the direction of the moment loads was investigated and the results are plotted in Figure 4.12d).

The correlation between the moment direction and axial displacement is plotted on a polar plot with positive axial displacement magnitudes plotted in blue and negative axial displacement magnitudes plotted in red for clarity. When analysing this plot it is important to remember that a moment occurring at 180 degrees indicates an overturning moment on the rotor, that is, a blade at the 90 degree position would be moving away from the viewer. Likewise, a moment occurring at an angle of 0 degrees indicates the overhanging moment from the rotor weight, that is, a blade at an upright position of 90 degrees would be moving toward the viewer. The plot clearly shows the correlation between the moment load direction and magnitude of axial displacement as all of the negative axial displacements are occurring when the total moment direction is indicative of the overhang moment due to rotor weight being dominant. It is also visible that the axial displacement is sometimes positive when the moment load is occurring between plus and negative 90 degrees, indicating that radial and moment loads must be of certain magnitudes to overcome the positive axial displacement expected from thrust loads on the bearing.

4.5 Visual Inspection of Loads

Having coupled the analytical drivetrain model developed in Chapter 3 with the internal load model derived above, and developed a methodology to incorporate varying stiffness

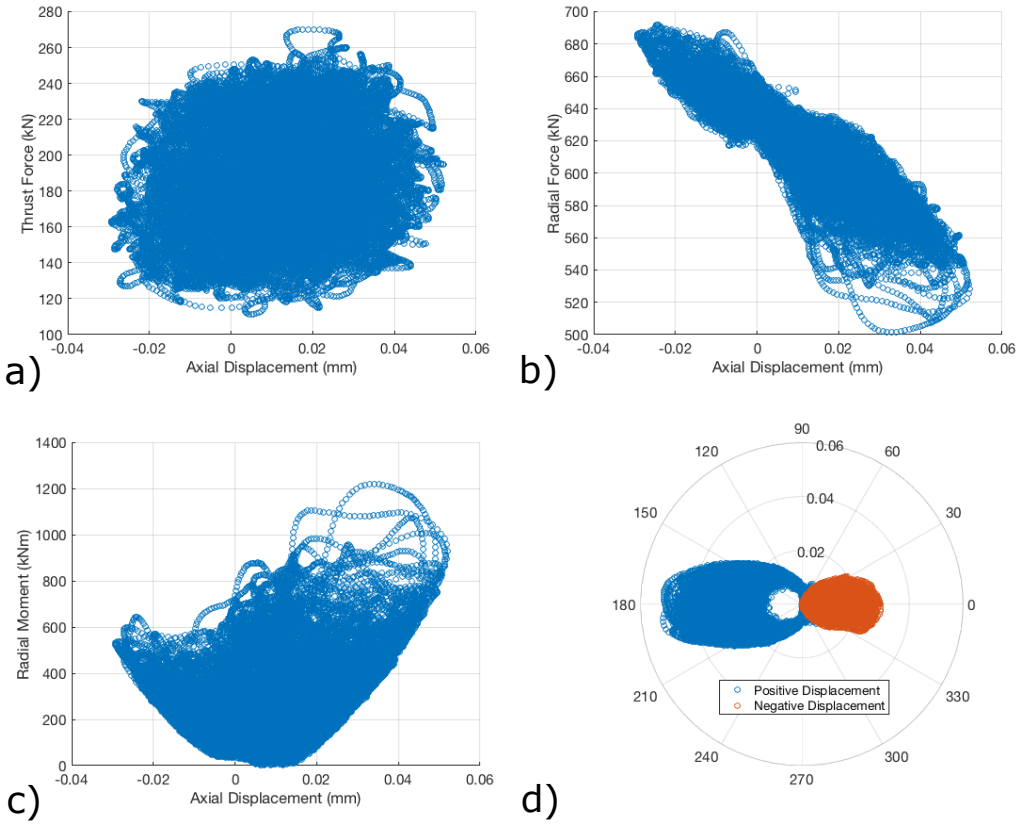

Figure 4.12: a) Correlation between inner race axial displacement and bearing thrust force. b) Correlation between inner race axial displacement and bearing radial load magnitude. c) Correlation between inner race axial displacement and bearing moment load magnitude d) Correlation between inner race axial displacement and bearing moment load direction. All results are taken from simulations in realistic wind conditions with a hub-height mean wind speed of 12m/s.

capabilities at the analytical modelling stage, the models were simulated operating in the 4 10-minute hub loading wind files presented in this chapter. The radial force and moment loads were then investigated visually in order to compare with the results in Section 3.5 and explore the load magnitude and direction effects of the varying stiffness capability.

The results may not be directly compared as the set of wind files used in the previous chapter differs from the wind files presented here. However, the loading results presented in the visual analysis in the previous chapter were determined for wind conditions with a shear exponent of 0.2 and a medium turbulence intensity, the same

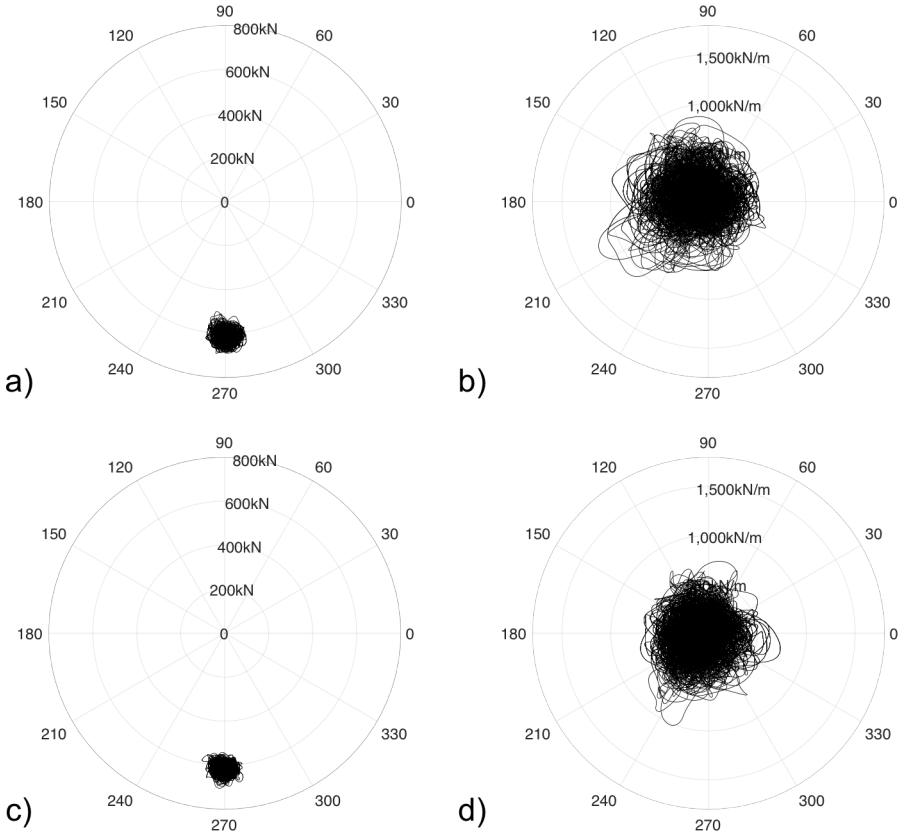

Figure 4.13: a) and b) show 10 minute time series plots of radial force and moment loads for 12m/s mean wind speed, medium turbulence intensity and a shear exponent of 0.2. c) and d) show 10 minute time series plots of radial force and moment loads for 14m/s mean wind speeds, medium turbulence intensity and a shear exponent of 0.2.

parameters used here. The main differences between the two sets of wind files are the mean wind speeds. The wind file set analysed in the previous chapter had mean wind speeds of 10, 12, 16 and 20m/s, where 12, 14, 18 and 24m/s were utilised here. Thus, the overall trends between the two sets of results can be compared.

Figures 4.13 and 4.14 display the magnitude and direction of radial force and moment loads on the DTRB for the 12 and 14m/s mean wind files and the 18 and 24m/s mean wind files, respectively. All plots are presented from the perspective of looking downwind onto the main bearing. It is immediately clear from the results that, although the radial force loads remain concentrated around the downward direction, the variation in the radial force magnitude is significantly reduced in the model with varying stiffness

capabilities. The variations in force magnitude increased with increasing wind speed and remained under 200kN of variation for the highest wind speed (24m/s) using the new model with varying stiffness capabilities. A significant reduction from 800kN of variations seen in the original results at 20m/s. There are also differences in the moment plots for the two models as the density of moment loads appear more circular in shape for the new model results. The moment load densities were more elliptical in the upwards and downwards direction in the initial analysis. The moment loads are still not concentrated in any one direction and evidence of loop structures are still present in both the radial force and moment plots.

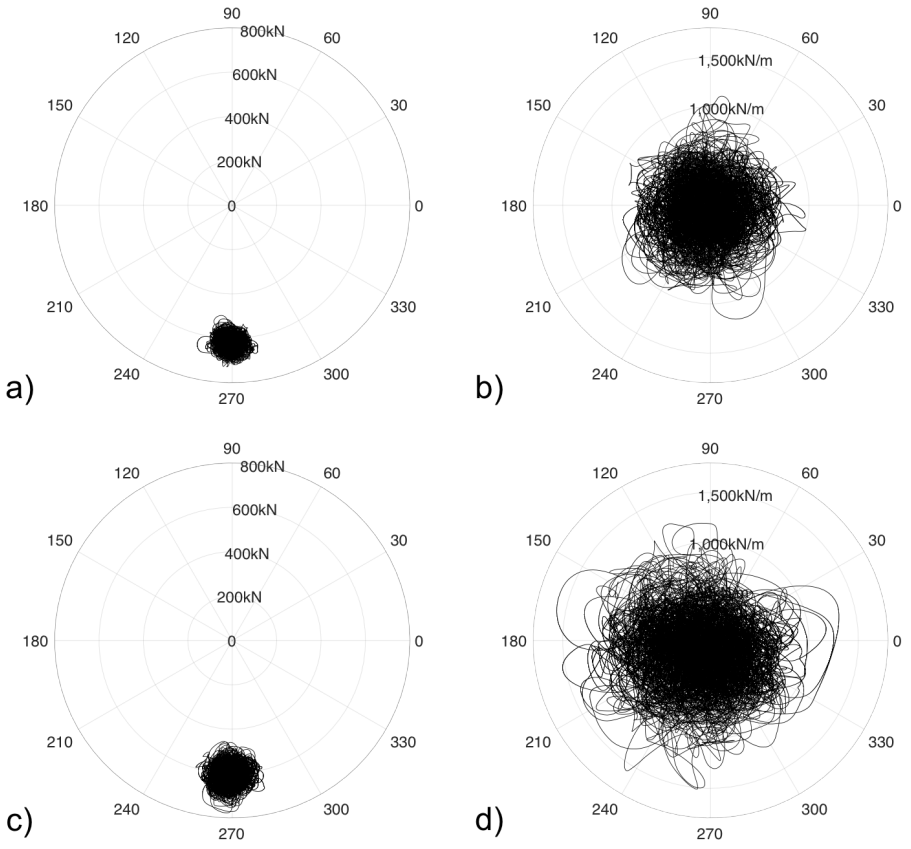

Figure 4.14: a) and b) show 10 minute time series plots of radial force and moment loads for 18m/s mean wind speed, medium turbulence intensity and a shear exponent of 0.2. c) and d) show 10 minute time series plots of radial force and moment loads for 24m/s mean wind speeds, medium turbulence intensity and a shear exponent of 0.2.

4.6 Load Loop Examples

Having developed a method to provide varying stiffness capabilities at the analytical model stage of the new model, shown how this adjustment affects the loading results on the bearing and determined the drivers for negative axial displacements of the inner race, the numerical model with varying stiffness capabilities was used to analyse load structures from the four hub-loading data sets. Following on from the work completed in Chapter 3, the bearing load results for the new model were analysed and a number of example loop structures were selected to explore the effects on internal bearing loads during these load structures. As it has been identified that moment loads appear to be the main driver of the response in the system, this visual analysis will focus on moment loading as opposed to moment and force loading for the sake of brevity. The figures plotted below present information about the bearing load information in two separate plots; plots a) and c) display magnitudes and directions of the moment loads on the bearing and plots b) and d) show the total load on a singular roller in each race as well as the force difference between the end slices of each roller. The moment plots are arranged such that a moment at 0 degrees indicates a moment generated by the overhang of the rotor weight and a moment at 180 degrees indicates an overturning moment on the rotor from high wind speeds. The force difference across the rollers, presented in plots b) and d) is dependent upon the number of 'slices' of the roller, with each roller divided into 30 'slices' here. The magnitude of the force difference across the roller is therefore a somewhat arbitrary number and must be understood in this context. However, it's existence indicates the presence of edge loading of the roller and it's analysis provides useful information of the internal load conditions. The markers 'B', 'C' and 'D' signify time intervals of the load structures across the four plots in each figure. While load loops were also found in the radial force loads for these example sets, their magnitudes and directions varied insignificantly compared to that of the moment loads, thus, they are not discussed here.

Figure 4.15a) displays an example moment load loop structure from the hub-loading data set with a hub-height mean wind speed of 12m/s (wind file 1). The moment

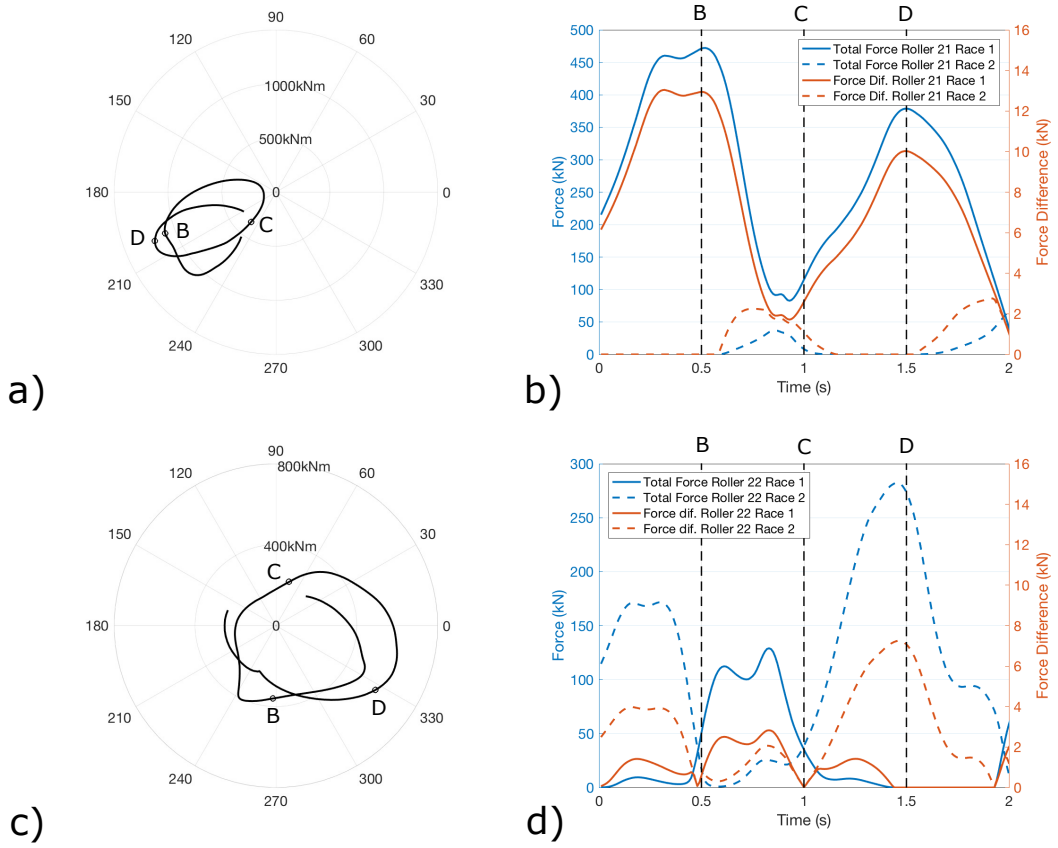

Figure 4.15: a) Moment load loop example from wind file 1 spanning 2 seconds. b) Corresponding loads on roller 21 from race 1 and 2 during the loop structure from wind file 1. c) Moment load loop example from wind file 2 spanning 2 seconds. d) Corresponding loads on roller 22 from race 1 and 2 during the loop structure from wind file 2.

load is seen to double in magnitude from 500kNm to 1000kNm in less than half a second before plummeting below 100kNm while changing direction by approximately 60 degrees. The magnitude then shoots to around 1500kNm in just over half a second before immediately falling back to around 400kNm, changing direction by around 30 degrees in the process.

Plot 4.15b) shows the loading on rollers 21 in both the upwind and downwind races during this load structure, where race 1 represents the upwind race and race 2 the downwind race. The total force and force difference across the roller of roller 21 in race 1 appears to be highly driven by the moment loads seen in Figure 4.15a), peaking when

the moment load peaks at points B and D and reducing significantly when the moment load reduces significantly just before point C. The total force on the roller doubles in magnitude from 220kN to over 450kN in the first half second of loading, drops to 100kN in the next half second at point C, increases again to around 380kN at point D, and then drops below 50kN at the end of the load example. The force difference across the roller in race 1 follows the same trend, peaking at over 12kN and remaining between around 2 and 3% of the total load magnitude throughout the plot. Roller 21 in race 2 remains mainly unloaded in comparison to the race 1 roller, peaking slightly higher than 50kN at the end of the plot. The roller in race 2 becomes loaded during the troughs of the race 1 roller loading indicating that the loaded regions on the two race ways are at opposite ends of the bearing. The force difference across the roller in race 2 increases at the beginning of each load period and could be up to 20% of the total loading on the bearing. The timing and magnitude of the force difference on the roller suggests that the roller loading could be initiated at the edges as it passes into the load region.

Figure 4.15c) displays an example moment load loop structure from wind file 2 (14m/s). The moment can be seen to change direction by 540 degrees within the 2 second time history while the magnitude varies between 200 and 600kNm. The direction of moment load changes by 130 degrees in the first half second while the magnitude varies from around 200 to 400kNm. The direction then changes by another 180 degrees in the next half second as the magnitude reduces back to around 200kNm. The final second of loading sees the moment direction change by 270 degrees while the magnitude increases to around 600kNm then drops back to around 200kNm.

Figure 4.15d) displays the total loading and load difference across rollers 22 in race 1 and 2 during the load loop structure. The total force on roller 22 in race 1 slightly increases and decreases again before increasing dramatically before point B. In the period between points B and C the total load peaks at around 110kN, drops to around 100kN and then increases again to around 130kN before dropping dramatically before point C. The total load then remains low before reaching 0 before point D. The load

difference across the roller follows a similar trend although it can be seen to drop to 0 at point B and point C. Roller 22 in race 2 is highly loaded in periods where the roller in race 1 is slightly loaded and vice versa, indicating that the load zones (or areas of highest load) are at opposite sides of the two races. The roller in race 2 can be seen to peak at around 175kN before becoming rapidly unloaded before point B. The load then increases to around 25kN between points B and C before increasing to over 270kN between points C and D. The load then declines sharply towards the end of the time series. The increase and decrease in roller loading in race 2 coincide with the increase and decrease in moment loads from point C to the end of the time series. The force difference across the roller in race 2 also follows the same trend as the total force of the roller, although interestingly falls to 0 at points B and C when the force difference across the roller in race 1 also falls to 0.

Figure 4.16a) displays an interesting moment load structure from wind file 3 (18m/s mean wind speed) where the moment can be seen to significantly vary in both magnitude and direction over the period of 2 seconds. The moment changes direction by 90 degrees during the first half second of loading while the magnitude varies from 500kNm to around 750kNm and then back to approximately 600kNm. The direction then changes by almost 180 degrees in the next half second while the magnitude drops to less than 250kNm. Between points C and D the direction changes by another 180 degrees while the magnitude drops close to 0 before increasing to 500kNm and then dropping again to approximately 300kNm. The magnitude then increases to 500kNm again and then drops off to around 200kNm at the end of the load structure, while the direction changes by almost another 180 degrees.

The total load and load differences for the sixth roller in each raceway is plotted in Figure 4.16b). The total force on the roller in race 1 can be seen to fall from around 175kN, remain at around 40kN for a fraction of time, and then become unloaded within the first half-second of loading. The roller then becomes slightly loaded again halfway between points B and C before increasing quickly to over 50kN after point C where a small peak is seen in the loading. The load then continues to increase to approximately

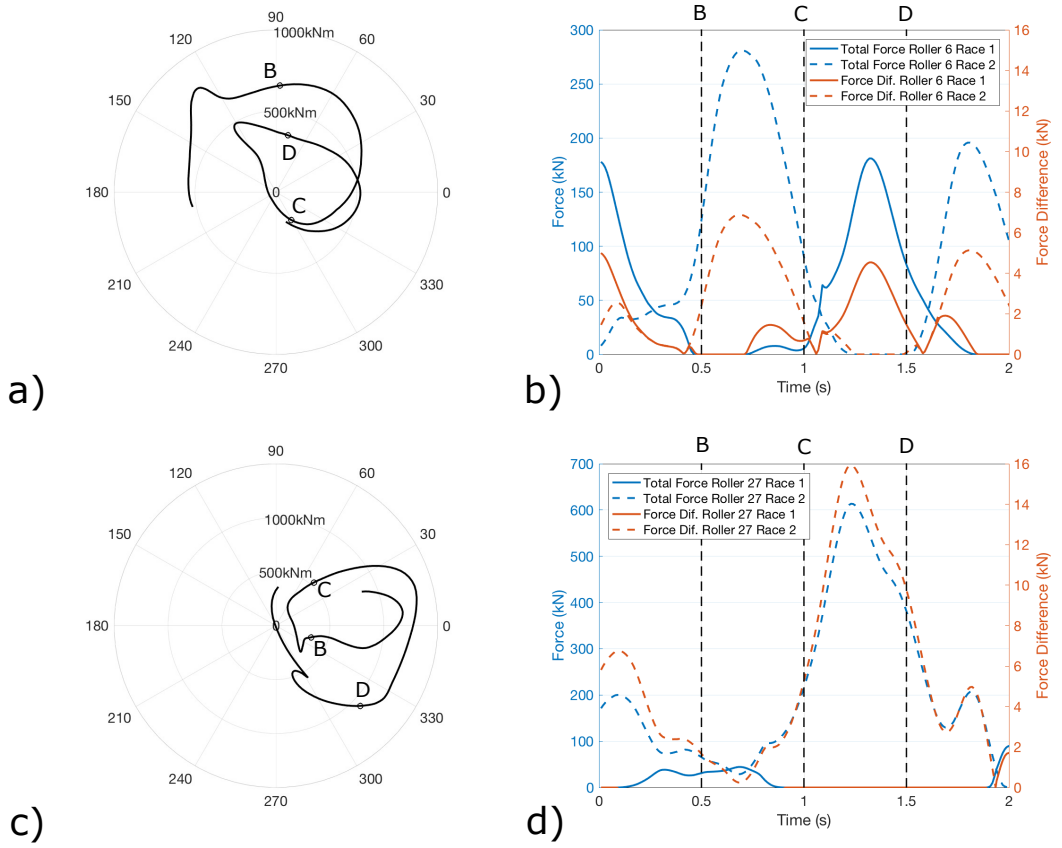

Figure 4.16: a) Moment load loop example from wind file 3 spanning 2 seconds. b) Corresponding loads on roller 21 from race 1 and 2 during the loop structure from wind file 3. c) Moment load loop example from wind file 4 spanning 2 seconds. d) Corresponding loads on roller 22 from race 1 and 2 during the loop structure from wind file 4.

175kN (the same magnitude as the start of the time example) before decreasing and becoming unloaded again within about half of a second. The force difference across the roller is around 5kN at the start of the load example and decreases to 0, following the trend of the total load on the bearing. However, the force difference can be seen to drop to 0, increase slightly and then decrease to 0 again just before point B. Interestingly, this same anomaly is also present in the force difference across the roller in race 2. The force difference across the roller in race 1 increases again when the roller becomes loaded, sharply drops to zero, then rises again to a brief peak in sync with the peak in total roller load after point C. The force difference across the roller in race 2 also drops to zero and rises again in sync with the roller in race 1. After the force difference on

the roller in race 1 briefly peaks, it increases again to over 4kN following the trend of the total force on the roller. It then drops to zero as the total bearing load decreases, increases again to 2kN and then drops to zero as the roller becomes unloaded. The total load on the roller in race 2 starts at around 10kN and increases to 50kN before sharply increasing before point B, when the roller in raxe 2 becomes unloaded. The load increases to 275kN before becoming unloaded within half a second. The load then increases from zero to 200kN after point D where it starts to decrease towards the end of the time sample. The force difference across the roller in race 2 peaks at around 6.5 and 5.5kN, following the same trend as the total load.

Figure 4.16c) displays a moment loading example from wind file 4 (mean wind speed of 24m/s). The moment can be seen to change direction by approximately 30 degrees and drop from over 1000kNm to less than 500kNm in the first half second. The magnitude continues to drop to around 250kNm and then there is a sharp directional change of over 90 degrees before the magnitude increases to 500kNm again at point C. The magnitude continues to rise to around 1400kNm before changing direction by 60 degrees before point D. The magnitude then starts to decrease, has another sharp direction change and then becomes unloaded before rapidly loading again in the opposite direction.

Figure 4.16d) displays the total load and load difference across the rollers during the moment load structure for wind file 4. The total load and force difference across the roller in race 1 follow the same trend. the total load increases to around 40kN where it remains somewhat steady for half a second before falling to zero again. In the same time period the force difference across the roller remains at approximately 1kN before also falling to zero. The total load then quickly increases to almost 100kN at the end of the of the time history as the force difference increases to 2kN. The total force and force difference across the roller in race 2 also follows the same trend and can be seen to fluctuate throughout the time history. The total force starts at around 200kN and gradually falls to around 40kN between points B and C before peaking to 600kN within the next half second and falling again to around 120kN. The load then increases again to around 200kN before sharply become unloaded after point D. This large peak in

roller loading seems to coincide with the peak in moment magnitude between points C and D. The force difference across the roller in race 2 peaks at over 6, 16 and 5kN at the same periods when the total load peaks.

The example loop structures above display some interesting bearing behaviours and provide an insight into the effects of extreme moment loads on the internal components of the bearing. The examples also provide some evidence which strengthens the findings in Section 4.4 that the moment loads on the bearing are the main drivers of roller displacements, and thus roller loads. 3 out of the 4 examples indicate that the loading regions of each race are at opposite ends of the bearing circumference. Considering the axial, radial and angular displacements of the inner race, only dominant angular displacements, resulting from moment loads, can result in the load regions of each raceway being at opposite sides of the bearing. A number of the examples also show that the fluctuation of total roller loads is synchronised with the moment load on the bearing. The consistent presence of force differences across the loaded rollers is also an indication that angular displacements of the race have significant effects on the roller loads and could be causing edge loading of some rollers.

4.7 Discussion

The current chapter has built upon and extended the capabilities of the analytical model developed in Chapter 3, creating a new numerical model which can determine internal load conditions of the bearing. Keeping in line with the aims of this project, multiple optimisation and simplification methods were attempted with the goal of achieving a fast-acting, computationally efficient model that can be utilised to analyse internal bearing conditions from 10-minute hub loading outputs from aeroelastic models. The above sections explored various simplification attempts and methodologies to improve the efficiency of the model before deriving the model equations which detail the relationship between the raceway and roller contacts. The effects of the constant torsional stiffness assumption at the analytical model stage was then investigated when used in conjunction with the numerical model (which has non-linear stiffness capabilities) and

a method of incorporating varying stiffness capabilities at the analytical model stage was developed. The method presented here for coupling the stiffness between the two models does not exist elsewhere in the literature and would be readily adaptable for use in other models which have been proposed. It was also discovered that the inner race becomes negatively displaced, that is, the inner race moves in the direction of the rotor, under certain wind conditions, during normal operation and despite the prevalence of thrust loads. A short study was then completed to determine the relationships between bearing loads and displacements where it was concluded that moment loads are the significant driver of bearing displacement. An analysis was then conducted to explore the effects of load structures, similar to that seen in Chapter 3, on the internal components of the bearing. This analysis provided a greater insight into bearing loading under normal operation and also more evidence that the moment loads on the bearing are the main driver for total bearing displacement.

The angle difference between the radial force and moment loads on the bearing were studied during attempts to improve the efficiency of the model in Section 4.2.1. The results showed a wide variation in the angles of applied loads on the bearing, strengthening the hypothesis derived from Figures 3.17 and 3.18 in the previous chapter, suggesting that force and moment loads on wind turbine main bearings may have different drivers in the wind field. The force loads on the bearing are concentrated around 270 degrees and are highly driven by the weight of the rotor; with the magnitude increasing or decreasing depending on the severity of overturning moment across the rotor. The direction of moment loading, in contrast, is not particularly concentrated in any direction around the bearing and must be driven by other aspects of the rotors interaction with the wind field. The total moment experienced at the hub is a combination of moment loads from each blade on the rotor. Each blade experiences somewhat sinusoidal moment loads as it rotates through the wind field, peaking when at an angle of 90 degrees (pointing to the sky) and troughing when at an angle of 270 degrees (pointing to the ground), assuming the inflow wind field has a vertical shear profile. This effect is obviously more pronounced when the wind field has a greater shear profile and the moment loads on each blade are not perfectly sinusoidal due to wind turbulence. In

any case, these continuously fluctuating moment loads on the blades are aggregated at the hub and subsequently translated, through a cantilevered shaft, to the main bearing. This helps to explain the highly fluctuating direction of moment loads at the bearing and why they are seen to vary around a full 360 degrees. Unlike the radial force loads, where the rotor mass is significant enough to dictate the direction of radial load, the moment on the bearing resulting from the rotor mass and main shaft cantilever is insignificant in regards to the magnitude of moments caused by wind loading and thus, do not dictate the direction of moment loads on the bearing.

Having determined that the force and moment loads have different drivers in the wind field and that moment load directions are not concentrated at any point around the circumference of the bearing, the analysis in Section 4.4 concluded that the moment loads on the bearing are also the main drivers for axial bearing deflections. As referenced above, the rotor weight is the dominant component in the radial force on the bearing and the overall overturning moment on the rotor, dictated by high wind speeds and high vertical speed gradients, is the main contributor to the fluctuations in these loads. It was initially discovered that the axial displacement was correlated with the radial load on the bearing. However, upon further investigation it was discovered that the radial loads and axial displacement are correlated by proxy due to the radial load actually being effected by the overturning moments on the rotor. While the initial attempt to compare the moment loads on the bearing and the axial displacement showed no strong correlations using the magnitude of the moment loads, the axial displacement was then compared with the direction of the moment loads and produced very strong correlations. That is, 100% of the negative axial displacements occurred when the total moment on the bearing was indicative of a dominant overhanging moment of the rotor. A moment load in this direction will increase the downward radial force already present from the weight of the shaft and the rotor and explains the plot in Figure 4.12b) where the inner race can be seen to be negatively displaced during periods of greater radial load magnitudes. It is also noted that the axial displacement of the inner race can also be positive when the moment direction is indicative of a dominant overhang moment on the rotor as seen in Figure 4.12d). It is hypothesised that, under such instances,

the negative axial displacement caused by the overhang moment and radial load on the bearing is not significant enough to negate the positive axial displacement resulting from the thrust loads on the bearing. It is important to understand that an isolated moment load on the bearing will not result in a net axial displacement in either direction as the additional axial displacements caused by the moment are balanced across the two rows of rollers. It is only with the combination of moment and radial and/or axial loads that a net axial displacement will occur. The plots in Figure 4.12 are from the 12m/s hub-height mean wind speed file where the turbine is operating at rated speed and hence, maximum thrust loads. It is, therefore, feasible that periods of net negative axial displacement of the inner race may be more prominent during operation at lower wind speeds or higher wind speeds where lesser thrust forces are present. During these periods, it is possible that rollers in the upwind race may be loaded more than the rollers in the downwind race. If this hypothesis is correct, the behaviour of DTRBs will be in direct contrast with that of DSRBs as studies by [37] and [28] have shown high thrust loading under normal turbine operation results in unloaded upwind rollers in DSRBs. The authors in [70] state that DSRBs could be replaced with DTRBs to improve thrust support capabilities, it appears here that the moment reaction capabilities of the DTRB may also result in more equal loading between the two races.

The radial force and moment loads were visually inspected and the results were compared with that of the analytical model developed in Chapter 3. Less variation in the radial force magnitudes were found when the model with varying stiffness capabilities was employed. The shape of the moment density plots also changed slightly. DTRBs have intrinsically non-linear stiffness, i.e, the more load imparted on the bearing, the greater the stiffness becomes. This effect is due to the increase in contact area within the bearing as loads are increased, due to an increase in the number of rollers under load and/or an increase in the contact area between rollers and raceways. The model developed in this chapter can model this effect and thus the stiffness of the bearing alters depending on the applied load. The analytical model presented in Chapter 3, however, has fixed torsional stiffness values input by the user. The best-fit constant torsional stiffness determined above is also an order of magnitude greater than the

stiffness estimated in the previous chapter. It is hypothesised that this difference in rigidity, and the ability for the internal model to respond to the imparted load is what reduces the variation in radial force loads seen in the results.

The analysis of interesting load cases in Section 4.6 provides an insight into the internal load conditions of the bearing during normal operation. While the study only details a small sample of loading time history, the results provide further evidence to support and strengthen hypotheses previously proposed in this work. The study exploring the inner race displacement drivers showed that the moment loads on the bearing were the main drivers for bearing displacement, with the direction significantly determining axial displacements and the magnitude effecting radial displacements. Moment loads on the bearing are, of course, also the main drivers for angular displacements of the bearing. Intuitively, if the moment loads on the bearing have a strong impact on total race displacement, then they must also considerably effect the individual roller loads around the raceways. This is shown to be the case in Section 4.6 where Figures 4.15 and 4.16 display individual roller loads peaking and troughing simultaneously with the moment load on the bearing. Further to this, in the load examples presented, the roller loads on each race are completely out of sync, indicating that the load regions on each raceway are at opposite sides of the bearing. This effect is a direct result of moment loads being the dominant driver of bearing displacements as they result in maximum displacements at opposite ends of the bearing for each race as detailed in Section 4.2.2. This finding is unexpected as previous studies concerning DSRBs as wind turbine main shaft bearings have shown the bearing to be dominantly loaded at around 270 degrees in the downwind race, with the upwind race remaining unloaded for significant periods of time. The results displayed here provide evidence to the hypothesis proposed in the previous paragraph, that upwind rows are loaded in DTRBs and furthermore, that the loading in the upwind row can be significantly greater than the downwind row. The moment reaction capabilities therefore significantly affect the internal loading behaviour of DTRBs when compared to that of DSRBs.

The results of the moment load loop case study provides further insights to the bearing

loading conditions. The moment load can be seen to significantly change direction (by more than 360 degrees) and magnitude in under 2 seconds for a majority of the load cases presented. Considering the analysis showing the strong correlations between the moment load direction and the displacement direction of the axial race, one must consider if these rapid changes in moment load directions are resulting in swift changes in the direction of axial displacements, and what damage could be caused by such loading events. Could such rapid changes in moment loads also cause the loading regions of each race to flip? If so, it is likely that rollers becoming loaded in such a manner may not be adequately lubricated and damage may occur to roller or raceway surfaces. Sudden and significant increases and decreases of roller loading by approximately 500kN can also be seen to occur in Figure 4.16d) during a period of less than a second. It is possible that such rapid loading and unloading conditions could result in the sliding of rollers. The authors in [45] state that DSRB main shaft bearings are not failing by fatigue but are predominantly failing by micropitting wear caused by poor lubrication and sliding of rollers. If the load cases highlighted here do indeed cause such conditions in the DTRB, then they may also lead to the damage of contact surfaces. The results from the load case studies also showed the presence of consistent force differences across the length of the roller during roller loading. Special care must be taken when interpreting the force difference results as the magnitude is directly dependent on the number of roller laminae, and therefore, the value presented is somewhat arbitrary. However, while the magnitude may be arbitrary, the presence of force differences across the roller is indicative of some degree of edge loading on the rollers. The consistence of force differences across the roller during periods of roller loading suggest that the rollers are constantly operating under some degree of edge loading. Edge loading can result in significant pressure increases at the edge of the roller-raceway contact area and cause increased fatigue on the materials. Edge loading can also cause roller sliding or skewing which could also lead to wear on the contact surfaces.

The load case analyses have provided results which suggest that rollers in DTRB wind turbine main bearings continually experience some degree of edge loading. Studying the effects of the constant stiffness assumption also provided results which showed in-

ner race angular displacement during loading scenarios derived from typical operation, displayed in Figure 4.6. A bearing operating under such conditions, with an angularly displaced inner race and edge loading of the rollers, will experience effects much like a bearing operating under angular misalignment. The effects of misalignment on tapered roller bearings is well understood as detailed in Section 2.5. Previous studies have shown that even slight misalignment of tapered roller bearings can significantly change the contact load distribution across the rollers and raceways, leading to higher localised pressures and loads at roller edges [2, 81, 82]. The localised pressures at roller edges substantially reduces bearing fatigue life and thus, the inclusion of even small misalignment in DTRBs can significantly reduce the fatigue life rating of the bearing regardless of the axial and radial load conditions [2, 72, 81, 82]. As main bearing loading and displacement is mainly driven by moment loads on the bearing which causes similar effects to misalignment, it is important to consider the effect of such loading on bearing damage or fatigue life.

Another important factor to consider here is the preload of DTRBs. DTRBs are typically installed with an interference fit, such that all rollers are deflected/loaded even in the absence of an externally applied load. This engages every roller around both raceways during load response, increasing the load region of each race and helping to share bearing-unit loads between all of the rollers, reducing maximum loads inflicted on any one roller. The inclusion of preload also increases the rigidity of the bearing unit which minimises displacements during operation. The inclusion of preload has been neglected in this study as appropriate values for DTRBs functioning as wind turbine main bearings were not available. Note, DTRB preload is extremely design specific, and so general levels are not easily determined for any particular application. However, similar to a recent study [77], some of the effect of preload was accounted for by the internal model developed in this thesis by setting bearing clearance levels to zero. While the inclusion of preload would be expected to reduce peak roller loads, as loads on the bearing would be shared more evenly between rows and rollers, the qualitative load trends presented here would be expected to remain the same. That is, radial force and moment loop structures are still expected to occur in the presence of preload.

This chapter has presented a derivation for a new numerical model of a DTRB which can determine internal load conditions from full time histories of hub-loading extracted from aeroelastic simulations. Multiple simplification methods were then systematically explored in an attempt to improve the efficiencies of the model. The effects of the constant stiffness assumptions from Chapter 3 were identified and a method to introduce variable stiffness capabilities at this stage was presented. Having determined how best to simply and efficiently model the DTRB main bearing, a number of studies were completed to gain an understanding of the operating conditions, determining that moment loads are the main drivers for displacements and the loading of internal components. As the bearing exhibits behaviours similar to that experienced by bearings operating under misalignment, and misalignment has been shown to significantly reduce the fatigue life rating of bearings, it is important to consider the effect of such loading on the life of wind turbine main bearings. The efficiency of the model developed here allows for fast analysis of multiple inflow wind conditions. The following chapter will use standardised methods along with the model developed here to gauge the impact of varying inflow conditions on bearing fatigue life and build upon the understanding of operational conditions.

The work in this chapter has provided significant insights with respect to all three research questions. Furthermore, the developed model will facilitate more expansive analyses of loading and fatigue in the following chapter.

Chapter 5

Effects of Wind Field Characteristics on Global Response and Internal Loading of a Double-Row Tapered Roller Main Bearing

Having developed a numerical model of a wind turbine main-bearing with capabilities of determining internal loading under complex and realistic inflow wind conditions, this chapter seeks to apply the model in order to better understand load behaviour and internal load distributions, along with impacts of such loading on the expected life of the bearing. In doing so, the results of this chapter will help to strengthen and solidify an answer to the second and third research questions posed in Chapter 2. The body of this chapter contains two analyses in an attempt to answer these questions and quantify the bearing loading and potential damage effects on a DTRB main bearing during normal turbine operation under various inflow wind conditions. The first analysis involves a detailed examination of how the bearing and individual

roller loads are affected by varying inflow wind conditions such as mean wind speed, shear exponent and turbulence intensity. As main bearings do not have application-specific design standards, the second analysis uses the method proposed in the ISO standards (ISO 16281 and 281) for determining bearing fatigue life to study bearing life sensitivities and drivers for each set of wind conditions. The results for each wind condition were compared in order to correlate wind field characteristics with bearing damage. This analysis was supported by the generation of a more extensive aeroelastic simulation data set (see Section 5.1).

Similar to other work in this field, precise micro-geometrical detail is unknown for any specific DTRB, therefore it is necessary that certain assumptions are made during numerical modelling. Simplifications, described in Section 4.2.2, were also used to improve the efficiency of the model and, as such, results should be interpreted with this in mind. Crucially, the undertaken modelling approach will allow for determination of representative life ratings and associated sensitivities. Considered variables go beyond just inflow, also including, lubricant types, lubricant conditions and bearing temperatures. In doing so, the practical operating parameters which are most important as fatigue life drivers can be understood.

The following sections discuss the generation of a new and extensive set of wind field data and aeroelastic hub loading before analysing bearing unit-loads when the numerical model is simulated operating in the new, more comprehensive, set of conditions. The effects of varying inflow characteristics on individual roller loading is then explored. The following sections discuss some limitations of performing fatigue life calculations using the numerical model developed in Chapter 4 before discussing additional factors, such as the stress riser function proposed in the ISO standards. The range of wind files and wind characteristics studied are then detailed. The underlying equations to calculate the basic and modified fatigue life rating of tapered roller bearings are then laid out before a new method to average the bearing loads over time-series and years is presented. Basic and modified fatigue life results are then presented and all results from this chapter are discussed.

5.1 Wind File Input Data

A wide range of wind files were generated with varying inflow wind conditions in order to determine the relationship between the wind field characteristics and the operational conditions of the main bearing. Much like the wind files detailed in previous chapters of this work, Bladed software was used to generate 10-minute, 3-Dimensional turbulent wind files using a Kaimal spectrum to describe the second order wind field statistics. Five sets of wind files were created with different wind flow characteristic parameters and six different wind fields were generated for each combination of parameters using different initial random number seeds to reach statistical significance. All wind file sets contained wind fields with hub-height mean wind speeds in the range of 4 to 24m/s (increasing in 2m/s) to cover the full operational envelope of the turbine. Different complete wind file sets were created with medium turbulence intensity (as defined in the standards [9]) and varying shear exponents of 0.1, 0.2 and 0.4, providing three sets of data to help determine the bearing load effects of wind shear. A further two complete wind file sets were created with high and low turbulence intensities, respectively, each having a fixed shear exponent of 0.2. Altogether, this provided a total of 5 complete sets of wind file data, including three variations in shear and three for turbulence intensity (with one case intersecting both). In each of the cases, six different turbulent wind fields were created at each of the eleven mean wind speeds, with the total number of analysed wind fields therefore 330. A 1.5MW wind turbine was simulated operating in each of these wind conditions and the hub loading was extracted to be injected into the numerical model developed in the previous chapter.

5.2 Bearing Unit and Individual Roller Load Analysis

The model developed in the previous chapter was designed to help bridge the gap between the strengths of the current existing models in the literature. The result is an efficient open-source main bearing model which can determine internal component loading under complex and realistic wind field conditions. As such, the following section

utilises the wind file data sets outlined above and the newly developed model to explore the bearing and roller load effects under varying wind conditions.

5.2.1 Bearing Unit Load Analysis

The mean and peak radial force and moment analysis in Section 3.4 provided insight into DTRB behaviour under varying wind conditions increasing the understanding of how wind field characteristics affects bearing loads. However, this analysis was completed with an incomplete set of operational wind loading data and utilised the analytical model with fixed torsional stiffness estimations. As a much more comprehensive set of wind loading data has been generated in this chapter, and the model has been extended to include varying stiffness capabilities in the previous chapter, a more complete picture of the minimum, mean and maximum loads on the bearing unit are explored in this section. In addition, a supplementary analysis exploring the dominant excitations of the bearing reaction in the frequency domain is presented in Appendix B.

The hub loading data generated by simulating the aero-elastic model operating through all of the wind file data sets was injected into the bearing model (in a quasistatic manner) and the identified axial, radial and moment loading recorded. The minimum, mean and maximum load values were determined across the six wind files at each operating point and the results are plotted in Figure 5.1. The minimum bearing moment was zero across all wind files and wind speeds and so was excluded from the plots.

Plots a), c) and e) in Figure 5.1 display the axial, radial and moment loads, respectively, throughout the full operational envelope of the turbine when the turbulence intensity of the wind is varied between high (A), medium (B) and low (C). Plots b), d) and f) in Figure 5.1 display the axial, radial and moment loads, respectively, throughout the full operational envelope of the turbine when the shear exponent is varied between 0.1, 0.2 and 0.4

Figure 5.1a) displays the bearing axial load results when the turbulence intensity is varied and the mean plots show the loads increasing from 4m/s and peaking at around

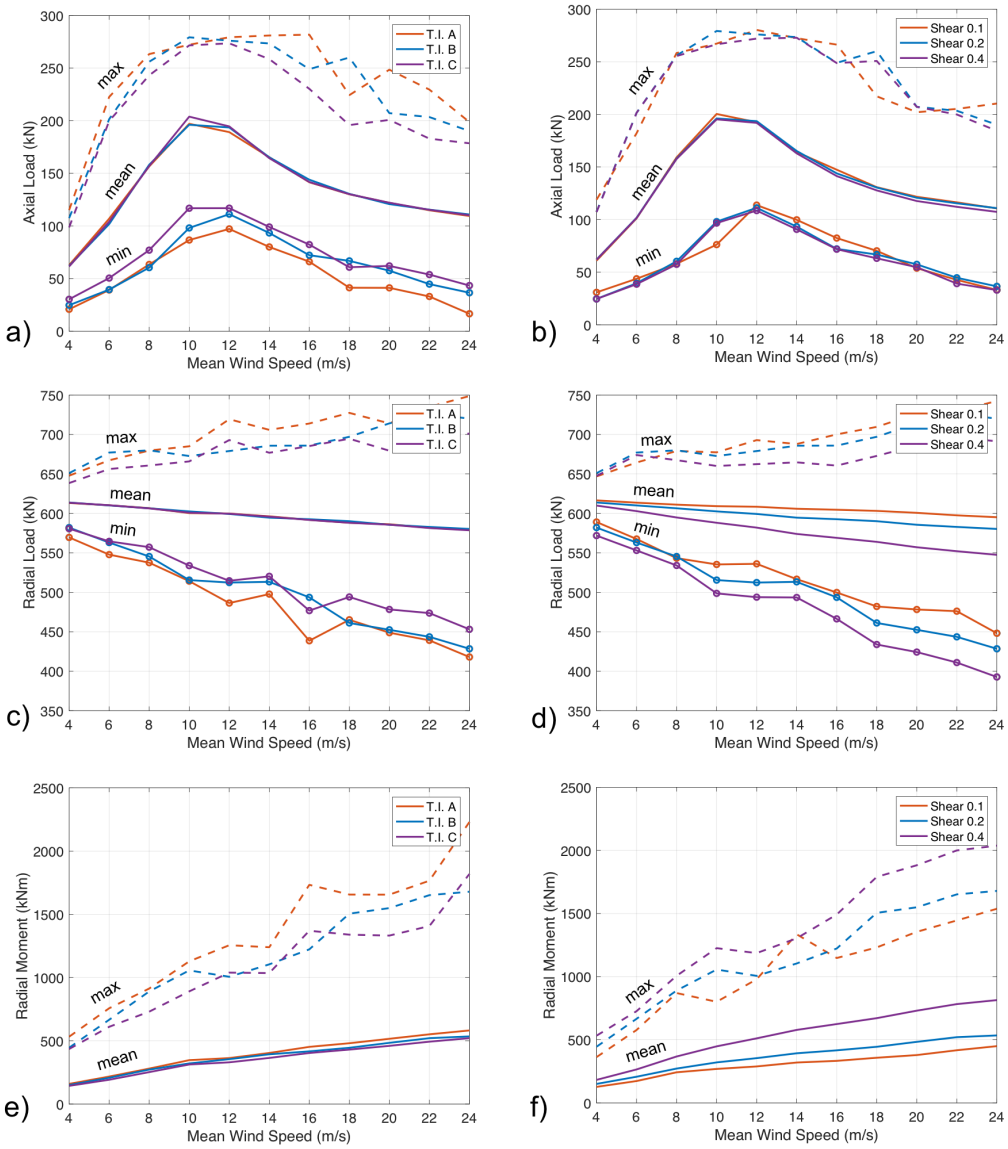

Figure 5.1: Sensitivity study of inflow wind conditions on wind turbine main shaft bearing loads. Plots a), c) and e) display the minimum, maximum and mean axial, radial and moment loads on the bearing throughout the full operational envelope of the turbine as the turbulence intensity is varied. Plots b), d) and f) display the minimum, maximum and mean axial, radial and moment loads on the bearing throughout the full operational envelope of the turbine as the shear exponent is varied. Minimum moment loads on the bearing unit were zero across all scenarios and were, therefore, excluded from the plots.

rated wind speed before falling again as wind speed increases further. This type of plot is expected for the axial load on the bearing as it is almost entirely driven by the thrust on the turbine rotor, and therefore resembles a thrust strategy plot [32]. The mean loads are very similar for the three different turbulence intensities, although there are slight differences around the rated speed where the axial load increases with decreasing turbulence in the wind. The minimum and maximum axial loads follow similar trends to the mean loads and it can be seen that they vary less from the mean as turbulence in the wind is decreased. Given that the axial bearing loads are almost entirely driven by thrust on the rotor, and thrust on the rotor is a spatial averaging of wind across the rotors swept area, one would expect a greater variation in both the maximum and minimum axial (or thrust) loads during higher turbulence intensity wind conditions.

The radial load results for the bearing under various turbulent intensities is displayed in Figure 5.1c) where the mean loads can be seen to steadily reduce from cut-in wind speeds as the mean wind speed is increased. There is negligent variation in the mean radial loads on the bearing throughout the various turbulence intensity conditions. The minimum and maximum radial loads show similar characteristics to the axial minimum and maximum load results in that the lower the turbulence intensity, the less variation from the mean loads. While the minimum radial loads follow the same trend as the mean and reduce with increasing wind speed, interestingly, the maximum radial loads increase with increasing wind speed for each level of turbulence intensity; this is likely due to increased aerodynamic sensitivities at higher wind speeds.

Figure 5.1e) displays the mean and maximum radial moment on the main bearing throughout the operating mean wind speeds and as the turbulence intensity is changed. The mean moments can be seen to increase with increasing wind speed, more than doubling in magnitude as the wind speed is raised from cut-in to cut-out. The mean moment loads can be distinguished by turbulence intensity with higher turbulence intensity wind fields producing higher moment loading on the bearing. The maximum moment loads also increase with increasing wind speed although with greater gradient than the mean loads. The maximum moment is seen to quadruple in magnitude from

cut-in wind speeds to cut-out wind speeds for the high turbulence intensity wind fields. A greater distinction can be made between the turbulence intensity values for the maximum moment loads, with higher turbulence intensity also causing higher maximum moments on the bearing.

The axial load results for the bearing under various wind shear conditions is displayed in Figure 5.1b). The minimum, mean and maximum axial loads again resemble that of a thrust curve, peaking around the rated wind speed. It appears that the lower shear profile in the wind field results in slightly higher axial loads on the bearing. This is likely due to the fact that the wind speed at the bottom of the rotor area will be closer to the hub-height mean wind speed when there is smaller wind speed gradients (parameterised as smaller shear exponents) present.

The radial load results for the bearing under various wind shear conditions is displayed in Figure 5.1d). There is a clear distinction in the radial load results for the various shear conditions with the highest shear exponent resulting in the lowest minimum, mean and maximum loads across the full range of wind speeds. These results match that of the analysis in Chapter 3 where it was hypothesised that larger shear profiles in the wind cause greater overturning moments on the rotor, thus, alleviating some of the gravitational radial loads from the weight of the rotor and shaft. Figure 5.1f) further strengthens this argument, displaying significantly larger mean and maximum moment loads on the bearing when operating in wind fields with higher shear exponents.

5.2.2 Distributed Roller Load Analysis

The internal bearing load model was developed with a rotating inner race (with speed equal to that of the wind turbine rotor) so that the rollers could be tracked around the raceway to provide more accurate loading time series results for each individual roller. However, in the interest of determining distributed loads from the perspective of bearing raceways, rollers were fixed in stationary positions around the bearing circumference for the current analysis. The hub loading data for the five wind file sets were then passed through the model and the mean and maximum roller loads were recorded.

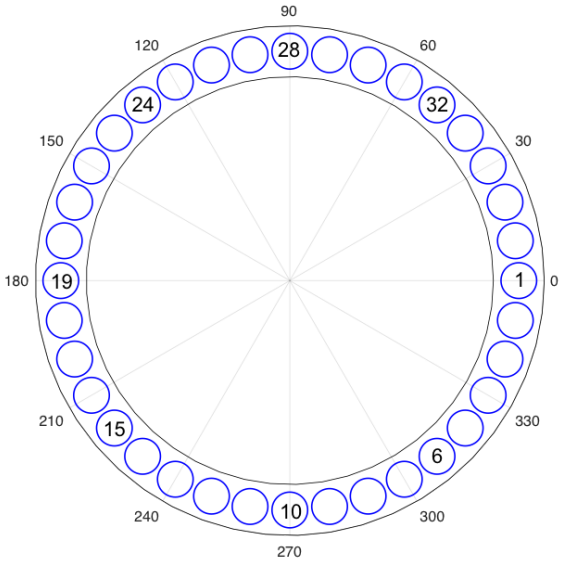

Figure 5.2: Front view (downwind) of a roller race depicting the locations of each roller around the circumference of the raceway.

Figures 5.2 and 5.3 have been created to aid the reader's understanding of the results. Figure 5.2 displays the roller positions around the circumference of the bearing as they were held fixed for the analysis. The image is displayed such that viewer is looking downwind onto the front face of the bearing. The number and position of each roller is the same for both roller rows. Figure 5.3 displays two example plots of the mean fixed-position roller loads for two rows across six wind file seeds plotted in both Cartesian coordinates in a) and polar coordinates in b). The Cartesian co-ordinate format clearly displays which rollers are under load and allows for a clearer presentation of multiple load profiles at the same time. The polar plot helps the viewer more clearly understand the loading regions on the bearing. Due to the number of results to be presented in each plot, below, the Cartesian co-ordinate system was selected for a clearer representation.

Shear Exponent

The following set of plots show the roller load distributions throughout the full range of wind speeds and as the shear profile of the wind is changed from a shear exponent

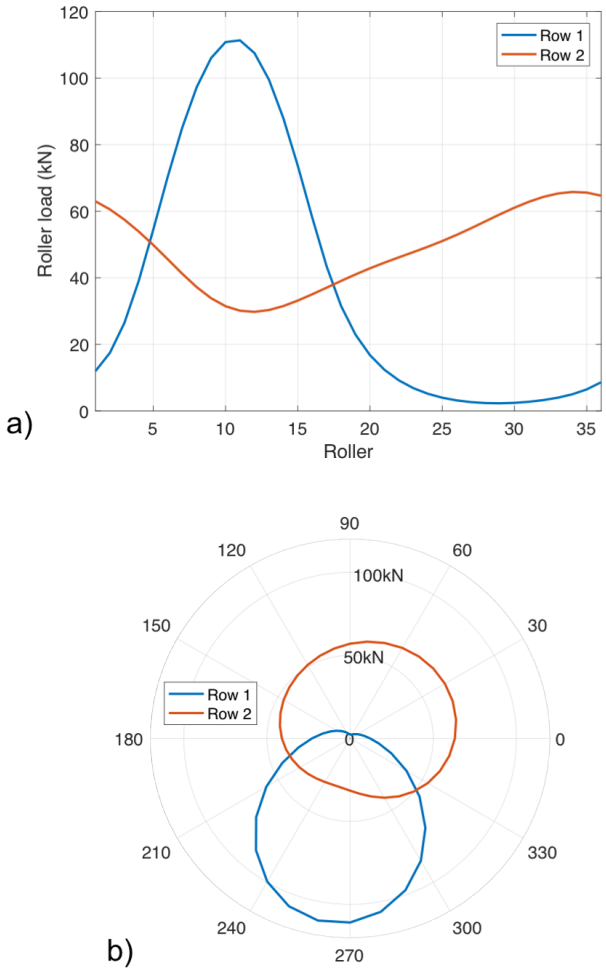

Figure 5.3: a) example distributed roller load plots for the upwind (Row 1) and downwind (Row 2) roller rows plotted in Cartesian format. b)The same example roller load distributions plotted in polarplot format.

of 0.1 to 0.2 and 0.4. The mean roller loads are presented in Figure 5.4 with the 0.1 shear exponent results in plots a) and b), the 0.2 shear exponent results in plots c) and d), and the 0.4 shear exponent results in plots e) and f). The results for row 1 in each scenario are presented in the left hand side plots (i.e plots a), c) and e)) and the results for row 2 in each scenario are presented in the right hand side plots (i.e. plots b), d) and f)).

Figure 5.4a) and b) display the mean roller loads for row 1 and row 2, respectively, for wind conditions with a 0.1 shear exponent and medium turbulence intensity. It is clear

from the results that fixed-position roller loads increase with increasing wind speed in both races. It is also noticeable that the loads are concentrated around roller 10 in row 1, the bottom rollers, and concentrated around roller 28 in row 2, the top rollers in the raceway. It is also clear that the loaded rollers in row 1 are experiencing larger mean load magnitudes than the most loaded rollers in row 2. However, there is a clear difference between the two rows in that there are rollers which remain mostly unloaded in row 1 whereas every roller has a mean load of at least 25kN in row 2. This effect is likely due to the thrust on the rotor causing an axial displacement of the bearing, resulting in all rollers in row 2 (the downwind row) to be engaged with the inner and outer raceways. The engagement of all the rollers in the second row results in the load being distributed across more contact points and leads to the rollers in the downwind row having lower mean loads than seen in the upwind row.

The plots in Figures 5.4c) and d) present the mean load distributions on row 1 and row 2, respectively, during wind conditions with a shear exponent of 0.2. They show similar results to the previous plots with with the loads concentrated around the rollers on the bottom of the bearing in row 1 (roller 10) and around the top of the bearing in row 2 (roller 28). There are also a couple of interesting differences as the shear exponent is increased. The mean loads on the rollers in the load zone have increased by around 10 to 50kN as the shear exponent has increased, with the mean load increasing at greater rates as the mean wind speed is increased. The mean loads of the rollers at the edges of the load region also decrease in value as the shear exponent is increased (i.e. the loaded zone becomes more concentrated at higher shear exponent).

Similar trends are seen again when the shear exponent is increased from 0.2 to 0.4 as displayed in the results in Figures 5.4e) and f). Here, the mean loads of the loaded rollers have increased again and it appears that the load region has shrunk further. The rollers in the bottom position of row 2 now see mean load values close to zero. It is also noticeable that the mean wind speed seems to have a greater effect on the mean load value of rollers under higher shear conditions with a difference of around 250kN between cut-in and cut-out wind speeds for the conditions with a shear exponent of 0.4

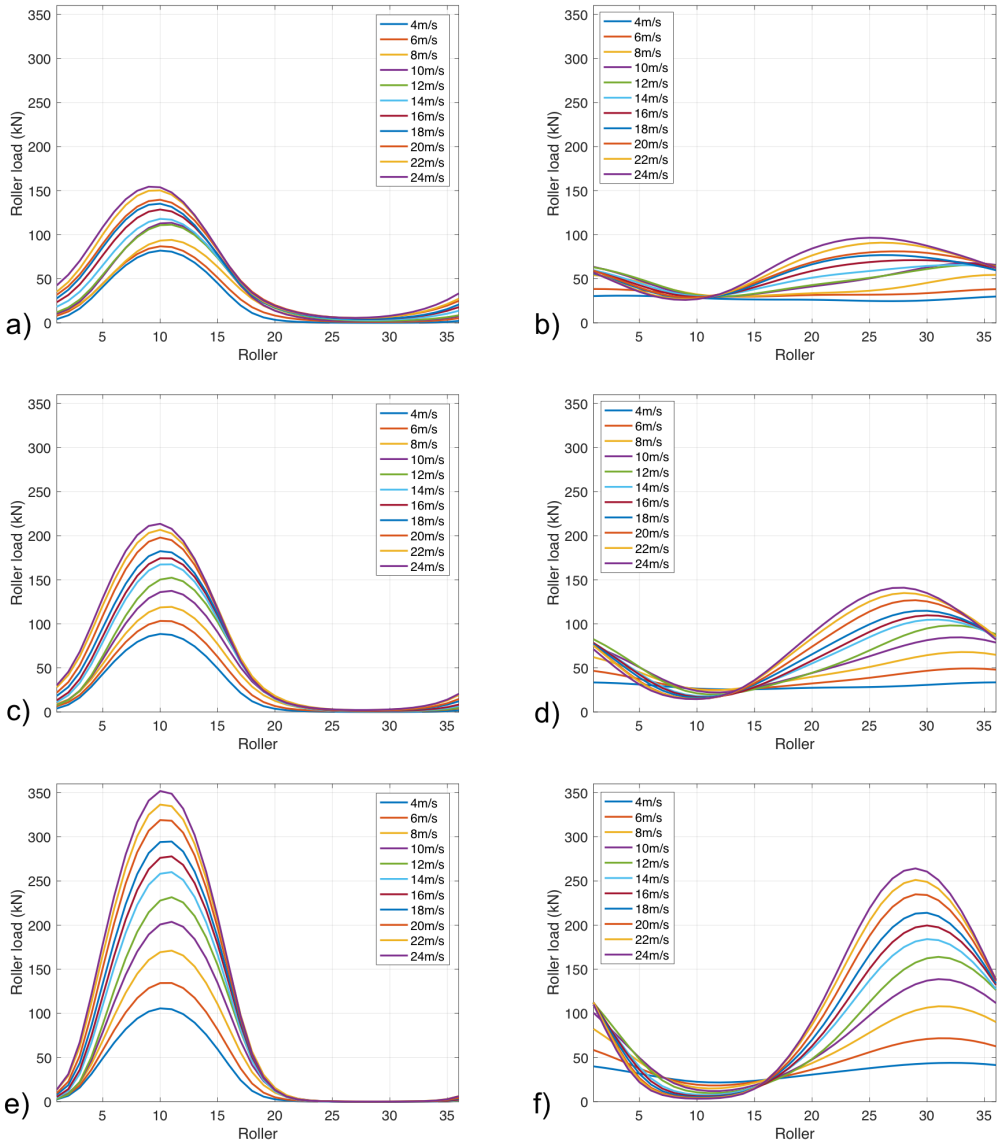

Figure 5.4: Sensitivity study of wind shear on **mean** roller loads. Plots a) and b) display the mean roller loads for the upwind (row 1) and downwind (row 2) roller rows, respectively, for a turbine operating throughout the full range of wind speeds with a wind **wind shear exponent of 0.1** and a medium turbulence intensity. Plots c) and d) display the mean roller loads for the upwind and downwind roller rows, respectively, for a turbine operating throughout the full range of wind speeds with a **wind shear exponent of 0.2** and a medium turbulence intensity. Plots e) and f) display the mean roller loads for the upwind and downwind roller rows, respectively, for a turbine operating throughout the full range of wind speeds with a **wind shear exponent of 0.4** and a medium turbulence intensity.

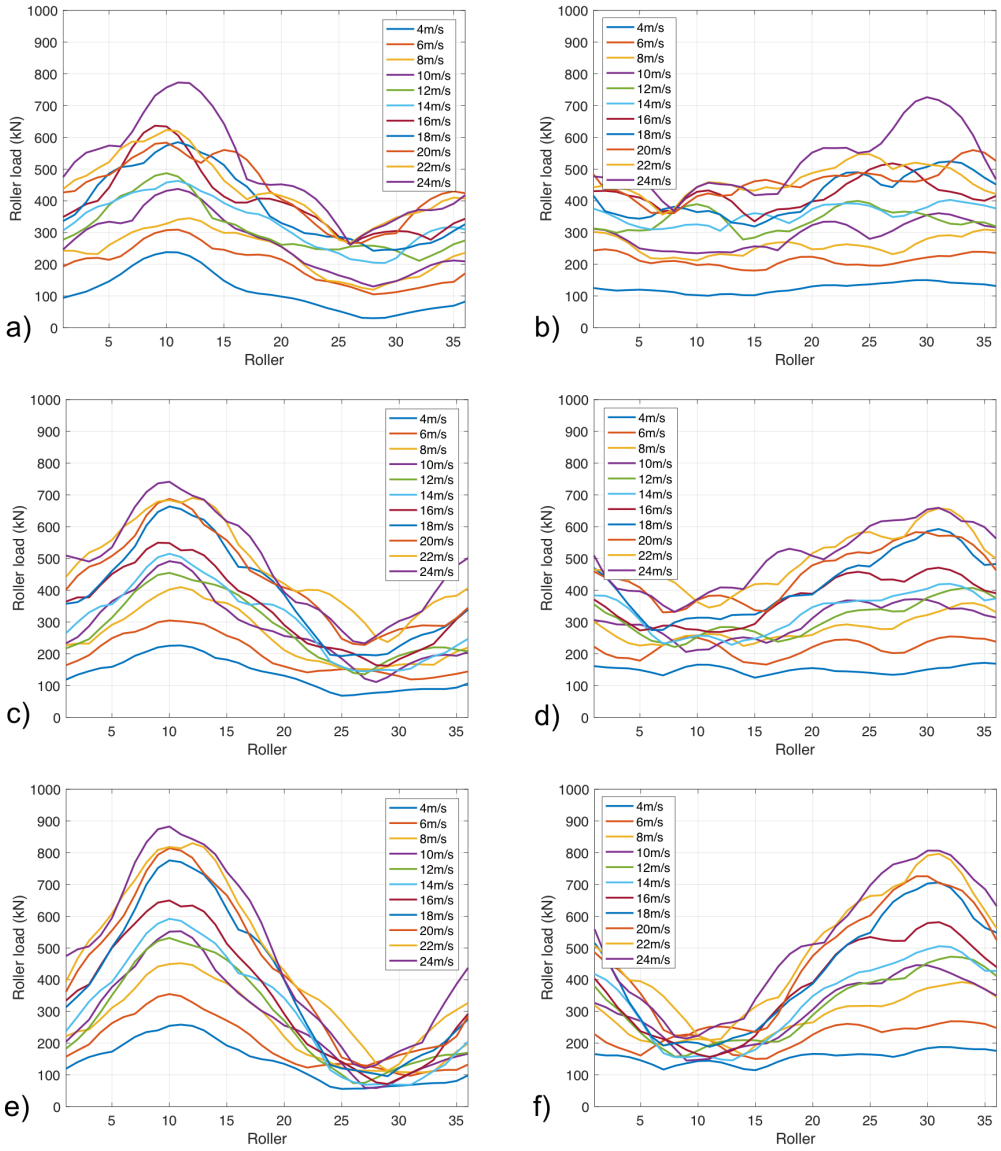

Figure 5.5: Sensitivity study of wind shear on **maximum** roller loads. Plots a) and b) display the max roller loads for the upwind (row 1) and downwind (row 2) roller rows, respectively, for a turbine operating throughout the full range of wind speeds with a wind **wind shear exponent of 0.1** and a medium turbulence intensity. Plots c) and d) display the max roller loads for the upwind and downwind roller rows, respectively, for a turbine operating throughout the full range of wind speeds with a **wind shear exponent of 0.2** and a medium turbulence intensity. Plots e) and f) display the max roller loads for the upwind and downwind roller rows, respectively, for a turbine operating throughout the full range of wind speeds with a **wind shear exponent of 0.4** and a medium turbulence intensity.

compared to that of around 75kN for the conditions with a shear exponent of 0.1

The maximum roller loads across all of the wind files for the varying shear conditions were also recorded and displayed in Figure 5.5. The layout of Figure 5.5 is the same as the previous Figure, with results from wind conditions with a shear exponent of 0.1 presented in plots a) and b), results from wind conditions with a shear exponent of 0.2 plotted in c) and d), and results from wind conditions with a shear exponent of 0.4 presented in plots e) and f). The left hand side plots again represent the rollers in row 1 and the right hand side plots represent the results from row 2.

The results in Figure 5.5 shows that the rollers in the 'unloaded region' in row 1 from the previous Figure do in fact experience periods of loading throughout the time histories, experiencing loads as high as 300kN during the low shear conditions. The overall trend of the maximum roller loads are the same as the mean loads; max loads on rollers at the bottom of the bearing in row 1 and top of the bearing in row 2 increase with increasing wind speed and shear while the opposite is true for rollers on opposite sides of the bearing in both rows. The plots show that individual rollers can experience maximum loads of 800kN in both rows during the high shear cases.

Turbulence Intensity

The mean and maximum roller loads were also determined for all of the wind files during wind conditions with varying turbulence intensity and the results are plotted in Figures 5.6 and 5.7. The results are plotted in a similar fashion as the previous Figures with the left hand plots displaying the results from row 1 and the right side plots displaying results from row 2. However, plots a) and b) now indicate wind files with a high turbulence intensity, plots c) and d) a medium turbulence intensity, and results from wind files with a low turbulence intensity are presented in plots e) and f). All wind files in this study have a wind shear exponent of 0.2.

Minimal effects are seen in the mean roller loads as the turbulence intensity is varied. Hence, the results are described without detailing each individual plot. The mean

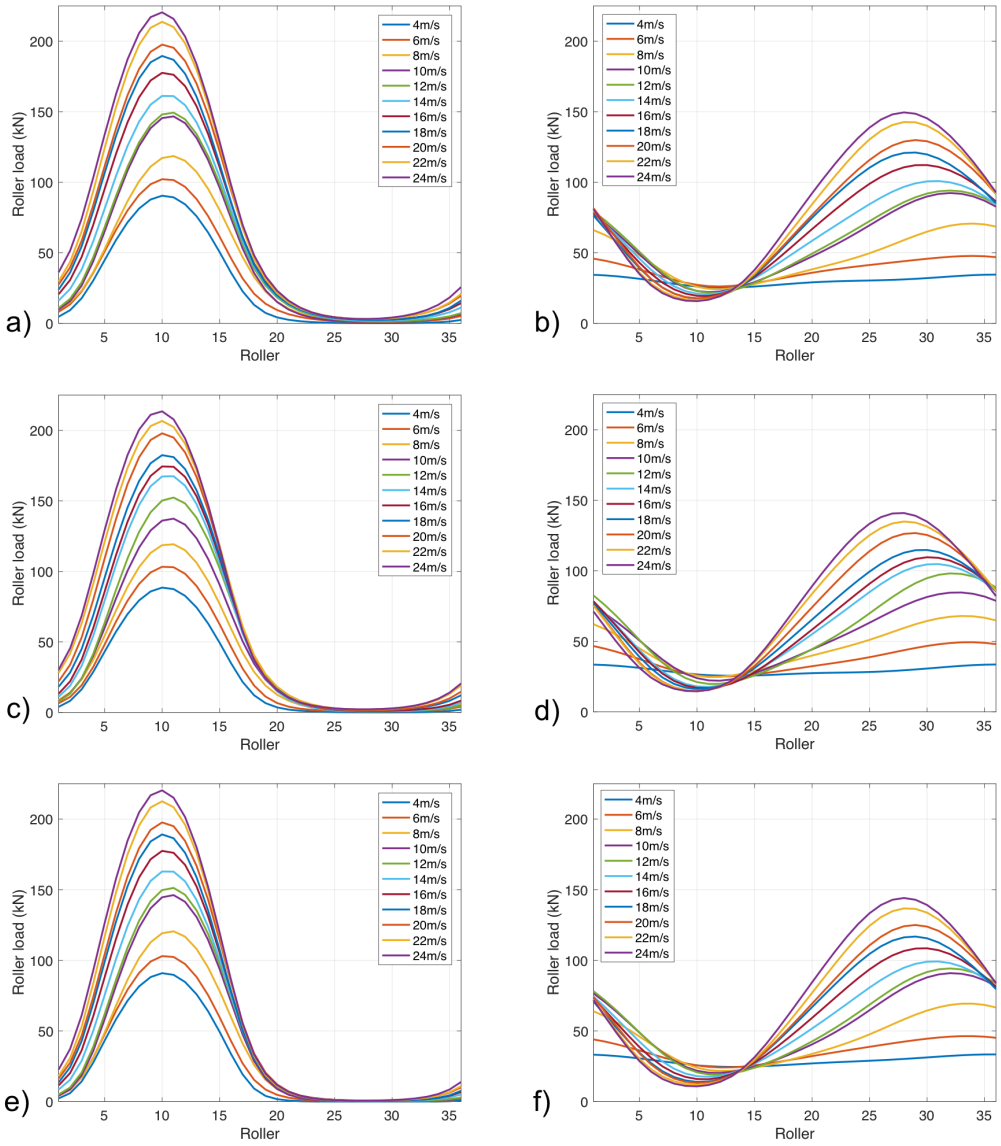

Figure 5.6: Sensitivity study of turbulence intensity on **mean** roller loads. Plots a) and b) display the mean roller loads for the upwind (row 1) and downwind (row 2) roller rows, respectively, for a turbine operating throughout the full range of wind speeds with a wind shear exponent of 0.2 and a **high turbulence intensity (A)**. Plots c) and d) display the mean roller loads for the upwind and downwind roller rows, respectively, for a turbine operating throughout the full range of wind speeds with a wind shear exponent of 0.2 and a **medium turbulence intensity (B)**. Plots e) and f) display the mean roller loads for the upwind and downwind roller rows, respectively, for a turbine operating throughout the full range of wind speeds with a wind shear exponent of 0.2 and a **low turbulence intensity (C)**.

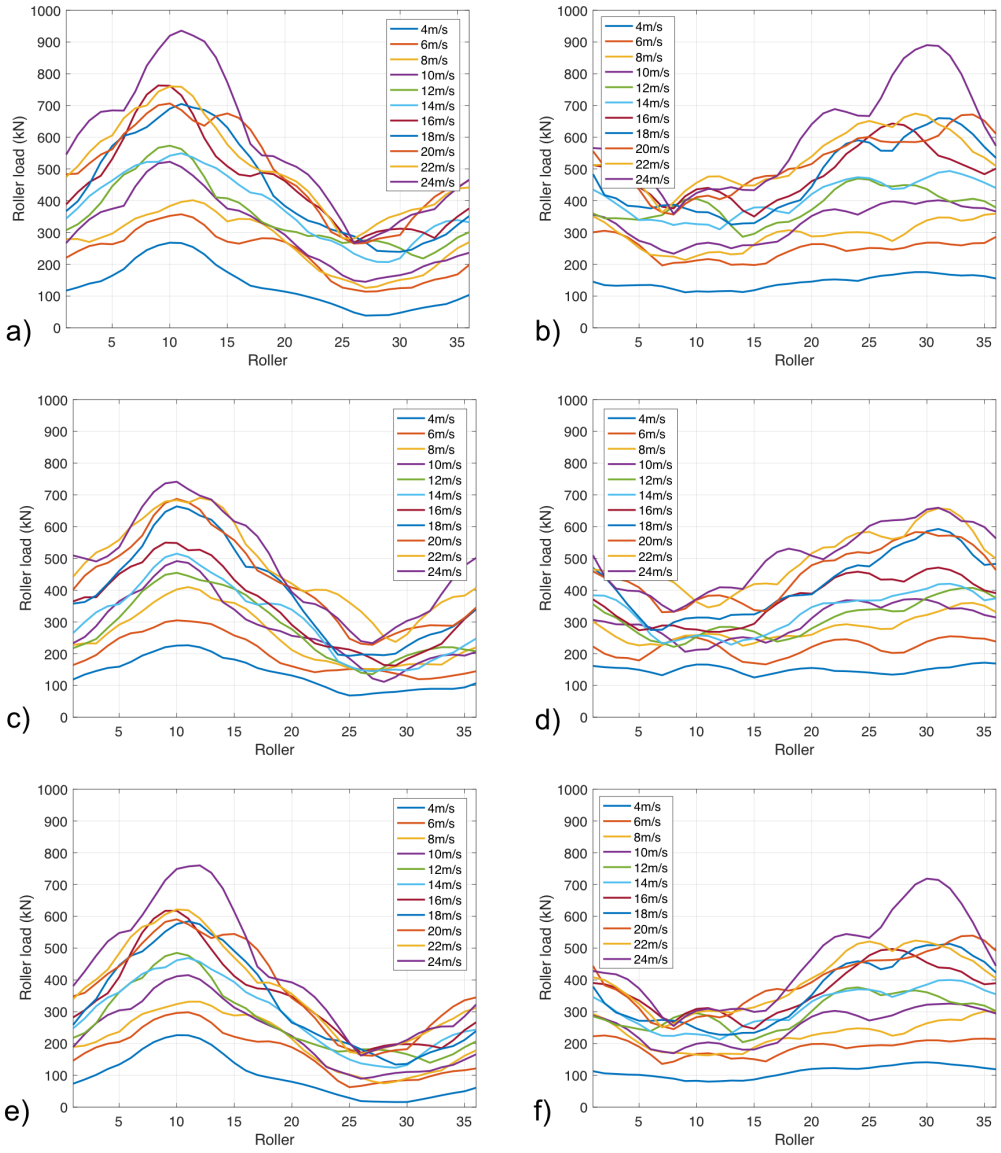

Figure 5.7: Sensitivity study of turbulence intensity on **maximum** roller loads. Plots a) and b) display the max roller loads for the upwind (row 1) and downwind (row 2) roller rows, respectively, for a turbine operating throughout the full range of wind speeds with a wind shear exponent of 0.2 and a **high turbulence intensity (A)**. Plots c) and d) display the max roller loads for the upwind and downwind roller rows, respectively, for a turbine operating throughout the full range of wind speeds with a wind shear exponent of 0.2 and a **medium turbulence intensity (B)**. Plots e) and f) display the max roller loads for the upwind and downwind roller rows, respectively, for a turbine operating throughout the full range of wind speeds with a wind shear exponent of 0.2 and a **low turbulence intensity (C)**

loads in the 'loaded regions' decrease as the turbulence intensity is changed from high to medium and then increase slightly again when the turbulence intensity is changed from medium to low. The loaded regions seem to somewhat shrink with decreasing turbulence intensity. This effect could help explain the slight increase in mean loads from medium to low turbulence, as the load is distributed amongst fewer rollers.

The maximum roller loads recorded as the turbulence intensity varied are presented in Figure 5.7. The overall trend displays the maximum roller loads in both rows increasing with increased turbulence intensity. This is expected when referring back to Figure 5.1 where maximum axial, radial and moment loads were all seen to increase with increasing turbulence intensity.

5.2.3 Bearing Load Analysis in the Frequency Domain

5.3 Fatigue Life Sensitivity Analysis for a Tapered Roller Main Bearing

The following sections detail the fatigue life sensitivity study using the model developed in the previous chapter. Note, for this analysis roller orbital trajectories were evolved at their pure rolling speed as detailed in Section 4.2.2.

5.3.1 Limitations of Fatigue Life Calculations in this Context

The standardised method for determining bearing fatigue life in [39] considers the load on each roller slice within the bearing and will therefore lend itself for use with the numerical model developed previously. The technical specification presented in [39] describes an advanced calculation method which makes it possible to consider the influence of tilt or misalignment on bearing life. Methods are also presented to estimate the influence of lubrication type, lubrication contamination, bearing temperature, and other operational conditions on the life rating of the bearing. While methods presented

in [39] pertain to fatigue life calculations, they do not cover the effects of other bearing failure methods such as wear or spalling.

However, as discussed in Section 2.5, it has been reported that main bearings are failing prematurely to their design life, predominantly with failure modes that are not well-understood or accounted for in turbine design standards [42]. Instead, main bearings are commonly failing by micropitting wear or false brinelling, thought to be initiated by sliding contact of the rollers and raceways, exacerbated by poor lubrication during operation [42, 45]. It is, therefore, pertinent to ask how accurate is the fatigue life rating calculation for predicting the likely operational life of a wind turbine main bearing? While the answer to this question is important, the required work to determine a solution falls outwith the scope of this piece of work. It is important, however, to distinguish between the behaviours of DSRBs and DTRBS as turbine main bearings. Kotzalas and Doll explicitly discuss the off-design failure modes with respect to DSRBs in [45]. They also suggest that a possible solution to reduce sliding and micropitting could be to install DTRBs in place of the DSRBs. While the authors in [42] don't explicitly state what type of bearing is being discussed, it is likely that most main bearings being referred to are DSRBs due to their prominence in the wind fleet at the time of publication. Since less information is known about how DTRBs perform under such loading conditions, it could be possible that the design standards do accurately predict their operational lifetimes.

The analyses have not been fully bottomed out for DTRBs as of yet, with current work in the literature only focusing on sensitivities to roller crowning, bearing misalignment and simplified oscillating loads [72, 82]. Wang et al. determined the fatigue damage of two single TRBs in a four-point-mount drivetrain system in [76] when the turbine is subjected to realistic load conditions. However, bearings were modelled with a linear diagonal stiffness and coupling effects were not considered. Results in the previous Chapter have shown that individual roller loads can more than double in magnitude when the non-linearity of bearing stiffness is considered, raising questions surrounding the validity and accuracy of fatigue life calculations when linear stiffness behaviours are

assumed. There are currently no studies in the literature that seek to determine the fatigue life prediction effects when internal loads are considered, the model employed has non-linear stiffness capabilities, and the DTRB is subject to realistic loading during complex inflow wind conditions.

Further to the uncertainty of these calculations in this context, the method outlined in [39] to calculate the fatigue life of a tapered roller bearing requires the calculation of distributed contact stresses over the roller-raceway contact areas. Determining contact stresses in bearings normally involves the employment of complex and intricate mathematical, numerical or FE models in addition to the model determining contact loads. Precise geometrical details of the roller and race profiles must also be known to provide accurate contact stress results. A single contact stress calculation requires digital computation, and considering that a roller and raceway contact area will require multiple contact stress solutions, and roller bearings have a considerable number of rollers (in this case 72), contact stress relationships for roller bearings can quickly become computationally intensive. Since the exact internal bearing geometries are unknown here, and the main aim of this work is to develop efficient models, no contact stress model is employed or developed here. Instead, the stress riser function presented in [39], which is determined from contact stress calculations and intended for a first approximation, is explored in an attempt to incorporate contact stress results into this work.

Due to the uncertainty surrounding the fatigue life calculations in the context of wind turbine main bearings, and the associated approximations using the numerical model and the stress riser function, the results developed in this chapter must be analysed with caution. Instead of claiming to necessarily be determining accurate fatigue life predictions for the DTRB main bearing, this work seeks to utilise the standardised fatigue life calculation method as a tool with which to explore fatigue life sensitivities and key drivers. More explicitly, the fatigue life results here do not necessarily indicate actual fatigue life ratings of the bearing under the studied wind conditions. The life rating results are instead used to perform a sensitivity analysis of various operational conditions to determine the main drivers in fatigue damage. Irrespective of the approx-

imations used here, the results will be valuable as realistic load conditions have yet to be analysed for DTRB main bearings in the literature. Therefore, the trends seen in this work will provide important insight into this problem.

5.3.2 Stress Riser Function

The stress riser function is presented in [39] as a first approximation to determine the effects of concentrated edge stresses for rollers with unknown profiles. As discussed in Section 2.3.4, straight-edged rollers contacting raceways of a greater length will result in somewhat elliptical contact areas and, hence, higher compressive stresses will occur at the roller edges. The stress riser function considers these effects by multiplying the loads determined at roller edge laminae by factors greater than 1, as can be seen in Figure 5.8 and Equation 5.3.3. However, as also discussed in Section 2.3.4, rollers can be crowned to reduce the stress peaks seen at the roller edges.

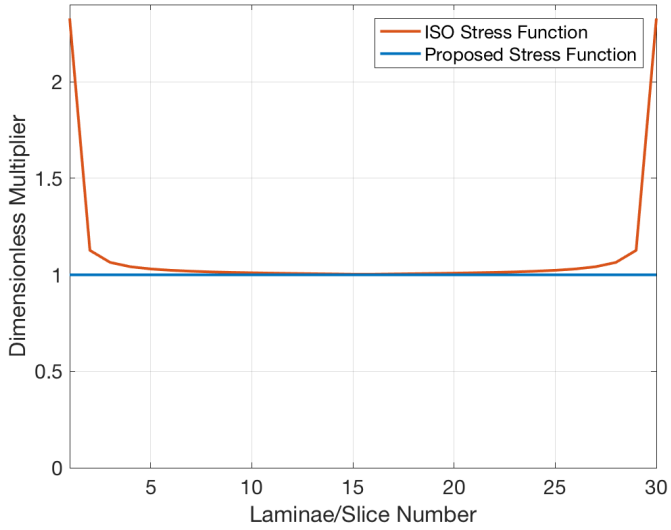

Figure 5.8: Multiplication factor of the standardised and the proposed stress functions.

It was also discussed that optimal crowning profiles vary with the loads experienced by the rollers but that logarithmic profiles can produce fairly uniform stress distributions over a wide range of loading and soften the significant edge stresses produced by other profiles. The life reduction caused by misalignment was shown to be considerably

worse for uncrowned rollers in [2] and the authors in [24] state that crowning can help accommodate minor misalignment but will not prevent damage when subject to considerable misalignment. The authors in [81] found that crowning reduces peak contact pressures seen under slight misalignment, but severe misalignment still results in peak contact pressures seen at roller ends of both crowned and uncrowned rollers. It is proposed here that no stress riser function be included in the fatigue life calculations. In other words, logarithmic profiled rollers are assumed as a first guess. This is equivalent to multiplying all laminae loads by 1 as shown in Figure 5.8 and assuming equal contact stresses across the length of the roller.

5.3.3 Basic Life Rating

The basic life rating of a bearing is the life associated with 90% reliability under the tested load conditions. In other words, if the basic life rating of a bearing is determined as 40 years at load X, then 10 out of 100 bearings would be expected to show evidence of fatigue after 40 years of operation at load X. The fatigue life calculation assumes high quality materials and good manufacturing quality of the components. Basic life ratings are generally used as first approximations for bearing selection or to select bearings for low-risk use cases. The first step of determining the basic life rating of a bearing with moment reacting capabilities is to calculate the basic dynamic load ratings of the inner ring, Q_{ci}, and outer ring, Q_{ce}. Note for symmetrical double-rowed bearings the basic dynamic load ratings of the inner and outer rings will be identical for both rows. The basic dynamic load ratings for the inner and outer races are calculated using the following equations

$$Q_{ci} = \frac{1}{\lambda\nu}\frac{C_r}{0.378Zcos(\alpha)i^{7/9}}\left[1+\left[1.038\left(\frac{1-\gamma}{1+\gamma}\right)^{143/108}\right]^{9/2}\right]^{2/9} \tag{5.1}$$

$$Q_{ce} = \frac{1}{\lambda\nu}\frac{C_r}{0.364Zcos(\alpha)i^{7/9}}\left[1+\left[1.038\left(\frac{1-\gamma}{1+\gamma}\right)^{143/108}\right]^{-9/2}\right]^{2/9} \tag{5.2}$$

where $\lambda\nu = 0.83$ (as indicated in the standards and also used in [72, 82]), C_r is the basic dynamic radial load rating of the unit, provided by the bearing manufacturer, and γ is an auxiliary parameter involving the roller diameter, bearing pitch diameter and roller-race contact angle.

The next step involves determining the basic dynamic load rating of each lamina of the inner and outer races, q_{ci} and q_{ce}, respectively. The equations are as follows

$$q_{ci} = Q_{ci}\left(\frac{1}{n_s}\right)^{7/9} \tag{5.3}$$

$$q_{ce} = Q_{ce}\left(\frac{1}{n_s}\right)^{7/9} \tag{5.4}$$

where n_s represents the number of laminae (or slices).

The next stage would then be to determine the stress riser function with respect to the number of lamina. For a non-crowned profile this would be determined by the following equation. However, the proposed stress function used in this study provides a unity dimensionless multiplier across all roller lamina.

$$f_i[k] = f_e[k] = 1 - \left[0.01 \Big/ ln\left(1.985\left|\frac{2k - n_s - 1}{2n_s - 2}\right|\right)\right] \tag{5.5}$$

The dynamic equivalent load for each lamina on the inner and outer races are then determined. The equations for determining the dynamic equivalent loads on the inner and outer races depend on the race being stationary or rotating relative to the load. In this case, the inner race is rotating and the outer race is stationary relative to the load. The dynamic equivalent load of any given lamina is determined by multiplying the load on the lamina by the corresponding dimensionless value represented by the stress riser function for that lamina and race, and then raising that term to the power of 4 or 4.5 depending on the races relative position to the load (4 for stationary and

4.5 for rotating). This calculation is completed for the given lamina across all of the rollers in the race before the results are summed and then divided by the number of rollers to provide an average value that represents all rollers. This value is then raised to the power of 1/4 or 1/4.5 depending on the races relative position to the load. This process is completed for all lamina of each race and row to provide an average dynamic equivalent load for each lamina and each race which represents the average load across all of the rollers. The equations are presented below.

$$q_{kei} = \left[\frac{1}{Z} \sum_{j=1}^{Z} (f_i[j,k] q_{j,k})^4 \right]^{1/4} \tag{5.6}$$

$$q_{kee} = \left[\frac{1}{Z} \sum_{j=1}^{Z} (f_e[j,k] q_{j,k})^{4.5} \right]^{1/4.5} \tag{5.7}$$

The equation for determining the basic life rating of the bearing, L_{10r}, is presented in the standards as

$$L_{10r} = \left(\sum_{k=1}^{n_s} \left[\left(\frac{q_{kci}}{q_{kei}} \right)^{-4.5} + \left(\frac{q_{kce}}{q_{kee}} \right)^{-4.5} \right] \right)^{-8/9} \tag{5.8}$$

however, Equation 5.8 only considers a single row bearing and thus, an equation to determine the basic life rating of a double row bearing may be derived as

$$L_{10r} = \left(\sum_{k=1}^{n_s} \left[\left(\frac{q_{kci,1}}{q_{kei,1}} \right)^{-4.5} + \left(\frac{q_{kce,1}}{q_{kee,1}} \right)^{-4.5} + \left(\frac{q_{kci,2}}{q_{kei,2}} \right)^{-4.5} + \left(\frac{q_{kce,2}}{q_{kee,2}} \right)^{-4.5} \right] \right)^{-8/9} \tag{5.9}$$

where subscripts 1 and 2 refer to the upwind and downwind rows respectively. This same extension of the standard theory is applied in [82]. The basic life rating equation divides the dynamic load rating of a lamina by the dynamic equivalent load experienced around the circumference of the race at said lamina and this term is raised to the

exponent of -4.5. This is done for both races and rows and the results are summed together to provide one value that represents a lamina on both races and rows. This process is completed for every lamina and the results are summed together and then raised to the power of -8/9 to determine the basic life rating.

5.3.4 Modified Life Rating

Once the basic life rating of the bearing is determined, extra steps can be taken to account for operational conditions of the bearing and calculate the modified life rating, L_{nmr}. The modified life rating is considered a more accurate calculation for determining the life ratings of bearings under specified lubrication and contamination conditions [38]. These extra considerations have proven to significantly extend the life predictions of bearings under favourable conditions or, in contrast, produce life estimates crucially lower than that of the basic life calculation where conditions are unfavourable. The variation and interaction of independent factors on the fatigue life of the bearing is referenced by considering the extra stress on the roller-raceway contacts resulting from the influences [38]. The effects of these influences are characterised by the life modification factor, a_{ISO}, which is a function of the viscosity ratio, κ, the contamination factor, e_C, fatigue load limit of the bearing, C_u, and the dynamic equivalent load of a bearing lamina, P. A modification factor for reliability, a_1, is also included which corresponds to a range of reliability values provided in the standards. As the design standards for wind turbines stipulate that modified life ratings for main bearings must be determined with a 90% reliability, the modification factor a_1 is equal to 1 here. The viscosity ratio, κ, is the ratio of the actual kinematic viscosity to the reference kinematic viscosity and describes the condition of lubricant separation. The reference kinematic viscosity is estimated using the bearings geometry and operational speed. Metal debris or other solid contaminants in the lubricant film can cause permanent indentations in the raceways leading to local stress risers. The contamination factor, e_C, considers the life reduction effects of the stress risers caused by these contaminants.

Before the modified life rating can be calculated, a combined dynamic equivalent load

at each bearing laminae, P_{ks}, is determined. This value accounts for the dynamic equivalent loads of both inner and outer races (q_{kei} and q_{kee}, respectively) as follows:

$$P_{ks} = 0.323Z(\cos\alpha)n_s \left(\left[q_{kei}^{4.5} + \left(1.038 \frac{q_{ci}}{q_{ce}} \right)^{4.5} q_{kee}^{4.5} \right] \Big/ \left[1 + \left(1.038 \frac{q_{ci}}{q_{ce}} \right)^{4.5} q_{kee}^{4.5} \right] \right)^{1/4.5} \tag{5.10}$$

The dynamic equivalent load of bearing lamina, P_{ks}, must be determined for each row. The life modification factor, a_{ISO}, can then be determined for each row using one of the following equations depending on the viscosity ratio, κ.

$$a_{ISO} = 0.1 \left[1 - \left(1.5859 - \frac{1.3993}{\kappa^{0.054381}} \right) \left(\frac{e_c C_u}{P_{ks}} \right)^{0.4} \right]^{-9.185} \tag{5.11}$$

for $0.1 \leq \kappa < 0.4$

$$a_{ISO} = 0.1 \left[1 - \left(1.5859 - \frac{1.2348}{\kappa^{0.19087}} \right) \left(\frac{e_c C_u}{P_{ks}} \right)^{0.4} \right]^{-9.185} \tag{5.12}$$

for $0.4 \leq \kappa < 1$

$$a_{ISO} = 0.1 \left[1 - \left(1.5859 - \frac{1.2348}{\kappa^{0.071739}} \right) \left(\frac{e_c C_u}{P_{ks}} \right)^{0.4} \right]^{-9.185} \tag{5.13}$$

for $1 \leq \kappa \leq 4$

The fatigue load limit of the bearing, C_u, is provided by the bearing manufacturer. However, the viscosity ratio, κ, and contamination factor, e_c, are dependent on the lubrication type, lubrication condition and rotational speed of the bearing. More information about the life modification factor, a_{ISO}, can be found in [38]. The modified life rating equation is then presented in [39] as

$$L_{nmr} = a_1 \left(\sum_{k=1}^{n_s} \left([a_{ISO}]^{-9/8} \left[\left(\frac{q_{kci}}{q_{kei}} \right)^{-4.5} + \left(\frac{q_{kce}}{q_{kee}} \right)^{-4.5} \right] \right) \right)^{-8/9} \tag{5.14}$$

however, much like the basic life rating, the standards only present the modified life rating of a single row bearing. The modified life rating was, therefore, extended in the double row case as,

$$\begin{aligned} L_{nmr} = a_1 \left(\sum_{k=1}^{n_s} \left([a_{ISO,1}]^{-9/8} \left[\left(\frac{q_{kci}}{q_{kei,1}} \right)^{-4.5} + \left(\frac{q_{kce}}{q_{kee,1}} \right)^{-4.5} \right] \right. \right. \\ \left. \left. + [a_{ISO,2}]^{-9/8} \left[\left(\frac{q_{kci}}{q_{kei,2}} \right)^{-4.5} + \left(\frac{q_{kce}}{q_{kee,2}} \right)^{-4.5} \right] \right) \right)^{-8/9} \end{aligned} \tag{5.15}$$

where the life modification factor, a_{ISO}, must be determined for each row. While the viscosity ratio, contamination factor and fatigue load limit for the two rows will be the same, the dynamic equivalent load of the bearing lamina will be different (as determined by the iterative numerical model developed in Chapter 4), hence the need for two different life modification factors.

5.3.5 Determining long-term equivalent life ratings with respect to site conditions

The bearing standards provide basic life and modified life rating results in millions of revolutions. While this unit may be useful for bearings which operate at constant rotational speeds, it is not very useful for bearings which change in rotational speed throughout their lifetime; such as for wind turbine main bearings. The units of the life rating calculations here are, therefore, translated from numbers of revolutions to units of time by using the rotational speed of the bearing. The bearing standards also provide the life rating calculations with respect to only one operational load and fail to express which load averaging methods would provide the most accurate estimation for bearings.

Averaging methods must be used when determining main bearing fatigue life estima-

tions due to the highly fluctuating operational loads and rotational speeds throughout the turbine operating points. An averaging method is proposed here which includes all rotational speed and operational load data from the full aeroelastic simulations. Avoiding the binning of operational loads or taking mean rotational speed values across the operating points ensures that every data point is included in the life rating estimation and no information is lost. The fatigue life is therefore calculated and converted to fatigue life in years at each time step for the 6 wind files with random seeds at each operating point. Miner's rule is then used to determine an equivalent life rating for each operating point using the following method.

Miner's rule assumes that each stress repetition at a given stress level is equal, and that damage accumulates such that operating at a given stress level for a given number of stress repetitions results in the exhaustion of a proportion of the components useful life. The fatigue damage is assumed to be linearly cumulative and Miner's rule is presented in Equation 5.16 where n_i represents the number of cycles or time spent at the i^{th} load level, L_i represents the permissible time or number of cycles to failure at the i^{th} load level, and D represents the proportion of component damage, where $D = 1$ corresponds to failure.

$$\sum_{i=1}^{n_s} \frac{n_i}{L_i} = D \tag{5.16}$$

A bearing operating for n_1 seconds at a load value resulting in a corresponding life rating of L_1 seconds will cause some proportion of damage. Therefore, it can be said that a bearing operating at n_1 seconds at a load with an associated life rating of L_1 seconds and then operating at n_2 seconds with an associated life rating of L_2 seconds will have suffered the same damage as a bearing operating at $n_1 + n_2$ seconds with an equivalent load that results in an equivalent life rating of L_{equiv} seconds. Explicitly,

$$\frac{n_1 + n_2}{L_{equiv}} = \frac{n_1}{L_1} + \frac{n_2}{L_2}. \tag{5.17}$$

Rearranging to determine the equivalent rating life gives,

$$L_{equiv} = \frac{n_1 + n_2}{\frac{n_1}{L_1} + \frac{n_2}{L_2}} \tag{5.18}$$

Multiplying the top and bottom of the fraction by $\frac{1}{n_1 + n_2}$ then gives

$$L_{equiv} = \frac{1}{\frac{1}{L_1} \cdot \frac{n_1}{n_1 + n_2} + \frac{1}{L_2} \cdot \frac{n_2}{n_1 + n_2}} \tag{5.19}$$

If the proportion of time spent at specific load levels is considered then

$$\phi_1 = \frac{n_1}{n_1 + n_2} \qquad \text{or more generally} \qquad \phi_i = \frac{n_i}{\sum n}$$

The equivalent rating life is then simplified to

$$L_{equiv} = \frac{1}{\frac{\phi_1}{L_1} + \frac{\phi_2}{L_2}} = \frac{1}{\sum \frac{\phi_i}{L_i}} \text{(in the general case)} \tag{5.20}$$

If every time-step of loading is weighted equally then each proportion, ϕ, will equal $\frac{1}{\sum n}$ and the equivalent life rating can be determined by

$$L_{equiv} = \frac{n_{tot}}{\sum \frac{1}{L_i}} \tag{5.21}$$

This method can be used to determine the equivalent life rating of the bearing for each value of hub-height mean wind speed, $L_{equiv,v}$. However, the equivalent life ratings

must be averaged again across the operating points of the turbine to consider the site conditions and provide an equivalent life rating that represents the loads experienced throughout 20 years of turbine operation. This can be achieved by using a probability density function which best describes the wind conditions at the turbine site to determine weighted averages for each equivalent life rating across the operating points. In this case, a Weibull function with a shape factor of $\kappa = 2$ and a mean wind speed of 8m/s is used to describe the site conditions. The scale factor, C, can then be determined from κ and the mean wind speed. The proportion of time spent at various wind speeds, W_v, can then be determined by differencing cumulative Weibull distribution values as in Equation 5.22, where $v-1$ and $v+1$ account for the mean wind speeds varying by 2m/s.

$$W_v = exp\left(-\left(\frac{v-1}{C}\right)^{\kappa}\right) - exp\left(-\left(\frac{v+1}{C}\right)^{\kappa}\right) \tag{5.22}$$

As the weighted averages produced by the probability density function provide a proportion of time that certain wind speeds are likely to occur, the method described above can be used to determine the equivalent life rating of the bearing over the turbines operational life such that

$$L_{equiv} = \frac{1}{\sum_v \left(\frac{W_v}{L_{equiv,v}}\right)} \tag{5.23}$$

where W_v is the proportion of time spent at wind speed v and $L_{equiv,v}$ is the equivalent life rating determined at each wind speed v.

5.3.6 Basic Life Results

The basic life rating for the bearing was calculated using both the ISO stress function and the proposed stress function to analyse the difference between the results. For this analysis, the hub loading data from the wind speed files with a medium turbulence intensity and wind shear of 0.1 was used. The site conditions are represented by a Weibull function with a shape parameter of 2, a scale parameter of 11.28 and a mean wind speed of 10m/s. The basic life rating was determined at each time step for each of the 6 wind file seeds and at each operating point as described above. The results were then averaged using the method outlined above and the equivalent life rating at each operating point (representing the 6 10-minute hub loading time series) for the two stress riser functions are plotted in Figure 5.9. The mean life rating (across the 6 turbulent seeds) at each operating point is plotted in Figure 5.9 as solid lines. The overall resultant life rating given the assumed site wind speed distribution is plotted as dashed lines for the two stress riser functions. The results are plotted with a linearly scaled y-axis in Figure 5.9a) and a logarithmic scaled y-axis in Figure 5.9b).

It is immediately clear from the plots in Figure 5.9 that there are significant differences in basic life rating results for the standardised and proposed stress riser functions. The proposed stress riser function outperforms the standardised stress riser function proportionally throughout the operational points of the turbine. This is expected due to the amplification of edge loads on the roller when the standardised stress riser function is employed. The basic life rating for both stress riser functions can be seen to significantly decline from cut-in wind speed to rated wind speeds and then continue to decline (albeit at a more marginal rate) until the cut-out wind speeds. The overall resultant basic life rating, considering the site conditions, is 7.9 years with the proposed stress function and 1.6 years with the standardised stress function. As a logarithmic roller profile is assumed, the proposed stress riser function was used for further study.

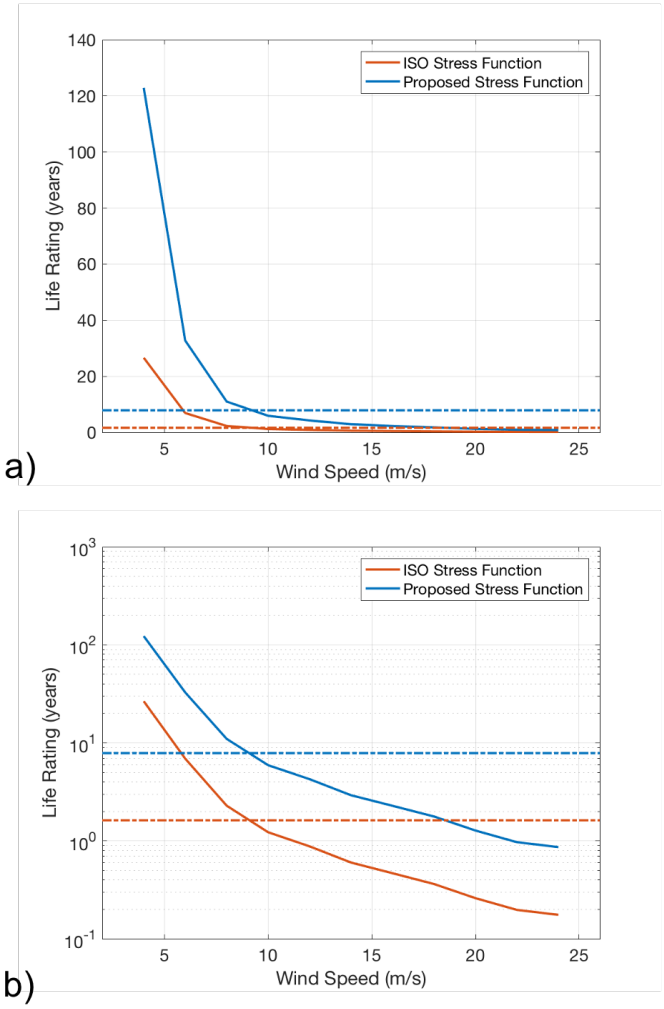

Figure 5.9: The basic life rating results at each turbine operating point for the standardised and proposed stress riser functions with the y-axis scaled a)linearly and b)logarithmically.

5.3.7 Sensitivity Analysis

The modified life rating calculations were used in place of the basic life rating method for the sensitivity analysis in order to analyse the sensitivity of additional conditional parameters on bearing life. This section will outline the various scenarios explored and present the results of the analyses.

Base Conditions

The wind files with a shear exponent of 0.2 and a medium turbulence intensity were taken as the base set of wind conditions. In addition to this, a lubricant with a viscosity grade of 460 at a bearing operational temperature of 40 degrees Celsius was taken as the base operational conditions. Finally, a Weibull distribution with a shape parameter of 2 and a mean wind speed of 8m/s was used as the base site conditions for the study. The sensitivity analysis was then performed by varying each parameter listed above independently to determine the effect on bearing life. All base condition results are plotted in blue for clarity.

Table 5.1: Grease Condition

Scenario	Level of contamination
G1	Normal cleanliness
G2	Slight to typical contamination
G3	Severe contamination
G4	Very severe contamination

Four different levels of grease contamination were analysed for the base conditions and for each set of conditions studied within the sensitivity analysis. The lubricant contamination scenarios and description of contamination levels are presented in Table 5.1 and are defined in accordance with ISO design standards [38]. For the purpose of this study, the contamination level is assumed to remain constant throughout the lifetime of the bearing and is assumed not to impact the viscosity of the lubricant. Therefore, all contamination effects are considered by the contamination factor, e_c.

Sensitivity to Lubricant Viscosity

Figure 5.10a) displays the modified life rating results for the base wind conditions when the lubricant type and lubricant condition is altered. The modified life rating is calculated for three different lubricant types with varying viscosity grades. The base condition lubricant is a grease with a viscosity grade of 460, indicated to be appropriate for wind turbine main bearings in [31], and plotted in blue for the various lubricant

conditions as detailed in Table 5.1. The lubricant is then changed to LGWM 1 grease which has a lower viscosity grade of 200 at 40 degrees Celsius and again to LGWM 2 which has an even lower viscosity grade of 80 at 40 degrees Celsius. Both LGWM 1 and LGWM 2 greases are described as being appropriate for wind turbine main shaft bearings in [61] and are able to withstand extreme pressures, high loads and low to medium rotational speeds. It is also noted in [23] that the DSRB main bearing installed in a specially instrumented turbine is lubricated with LGWM2 grease.

The life rating can be seen to decrease with increasing levels of lubricant contamination across all plots in Figure 5.10a), with very severe contamination scenarios drastically reducing life ratings. The plots also show that the modified life rating decreases significantly with decreasing viscosity grade. Operating with a lubricant viscosity of 200 can be seen to have a greater detriment to bearing life than severely contaminated 460 grade lubricant. Likewise, operating the bearing with the LGWM 2 lubricant (80 viscosity grade) is comparable to operating with very severely contaminated LGWM 1 lubricant. These results indicate that higher viscosity lubricants may increase the life of wind turbine main bearings, however, this would come at the cost of higher friction in the system.

Sensitivity to Operational Temperature

The operating temperature is assumed to remain constant throughout the full operational envelope here and, as such, the effects of rotational speed, friction and lubricant contamination are ignored. Under such assumptions, the modified life rating was calculated when increasing the operational temperature from the base case of 40 degrees Celsius to 60 and 100 degrees Celsius and the results are plotted in Figure 5.10b). Operational temperatures of a healthy main bearing typically vary between 20 and 40 degrees Celsius [23] and higher temperatures can be indicate the development of a fault [5, 13]. While it is unlikely that a bearing would ever operate at 100 degrees Celsius or spend any prolonged periods of time at 60 degrees Celsius (temperatures of 100 degrees would likely trigger turbine safety software procedures to emergency stop the turbine),

extreme temperature values were chosen for the sensitivity study to provide a trend across a wide range of temperatures. The plot displays the modified life rating reducing significantly with increasing temperature. These results are similar to that of the viscosity sensitivity analysis as lubricant viscosity is reduced by increased temperatures. The effect of lubricant contamination seems to reduce as the temperature rises, with no effect seen at 100 degrees Celsius. This could be due to the modified life rating already being extremely low with the cleanliest lubricant condition tested.

Sensitivity to Turbulence Intensity

The sensitivity of the bearing modified life rating to turbulence intensity of the inflow wind field was then assessed. The turbulence intensity was changed from its baseline medium value (B) to high (A) and low (C) as defined by IEC wind turbine design standards [9] throughout the turbines full operational envelope and the modified life rating was determined with the varying levels of lubricant contamination. The varied results are plotted alongside the base condition results in Figure 5.10c). The results show the fatigue life of the bearing increasing with decreasing turbulence intensity. While the mean bearing moments and loads will remain similar throughout the various turbulence intensities in the wind, it is expected that the reduction in fatigue life with increased turbulence intensity is the result of increased peak moments and loads caused by the greater deviations from the mean wind speed experienced with higher turbulence intensities.

Sensitivity to Wind Shear

The sensitivity to inflow wind shear profile was also assessed. The shear exponent was changed from the base condition of 0.2 to 0.1 and 0.4 across the lifetime of the turbine and the modified life rating was determined for the four levels of lubricant contamination. The results are plotted in Figure 5.10d). It is clear from the results that the modified life rating reduces significantly with increased vertical shear gradient in the wind profile. The life rating is seen to fall by approximately 50% for all lubricant

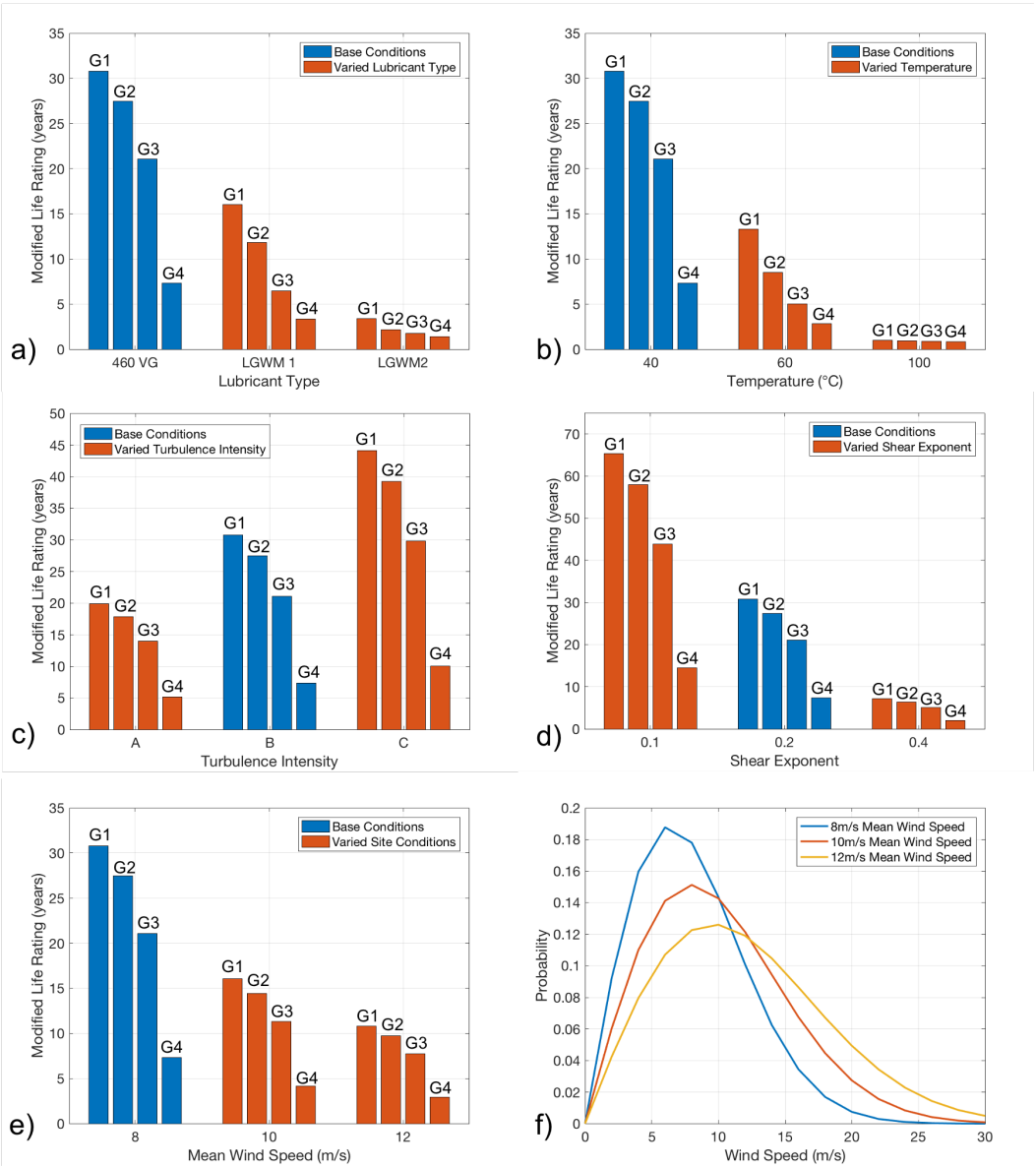

Figure 5.10: The modified life rating results for a range of lubricant contamination levels displaying the sensitivity to a) lubricant type, b) operational temperature, c) turbulence intensity, d)wind shear profile and e) the mean wind speed at the turbine site. f) displays the Weibull distribution for the 3 site conditions tested in e).

contamination levels when the wind shear exponent is doubled from 0.1 to 0.2. The modified life rating results then fall by greater than 50% when the shear exponent is doubled again from 0.2 to 0.4. It is expected that the life rating reduces so drastically with increased wind shear due to the higher wind speed gradients over the rotor re-

sulting in increased moments on the main shaft and, as demonstrated in the previous chapter, the moment loads on the bearing are the main drivers of bearing displacement and roller loads.

It is interesting to note that while higher wind shear profiles are seen to decrease the life rating of DTRBs, it has been found that higher wind shear profiles result in higher life ratings of DSRB main bearings [43]. In the self-aligning DSRB case, large overturning moments on the rotor from high shear acts to lift the rotor, counteracting gravity and so reducing the mean radial load on the bearing. This in turn, increases fatigue life ratings for DSRB main bearings under higher shear values. Results presented here demonstrate that the opposite holds true for tapered roller bearings.

Sensitivity to Mean Wind Speed

The sensitivity of fatigue life rating to the turbine site conditions was also analysed by changing the mean wind speed experienced at the site. The mean wind speed was increased from the base condition of 8m/s to both 10 and 12m/s and the modified fatigue life rating calculated. The results are plotted in Figure 5.10e). The Weibull distribution for the 3 tested site conditions are also displayed in Figure 5.10f). The results show that the modified fatigue life rating is sensitive to the mean wind speed at the turbine site, with the fatigue life decreasing as the mean wind speed increases. The fatigue life can be seen to decrease significantly between the site with 8m/s mean wind speed and the site with 10m/s mean wind speed and continue to decrease, although less significantly, from the 10m/s site to the site with a mean wind speed of 12m/s. Such a significant difference between the base site conditions and the site with 10m/s mean wind speeds is likely due to the increased time operating around the turbines rated speed in the latter scenario, where axial loads are at their peak. The moment loads on the rotor, and therefore translated to the main bearing, also continue to increase with increasing wind speed. The increased moment loads, combined with the increased axial loads will result in much greater roller loads and hence have such an effect on the fatigue life of the bearing. The decline in fatigue life rating between the 10m/s mean

wind speed site and the 12m/s site can be explained by the aforementioned increase in moments across the rotor with increased wind speeds. The reduction in fatigue rating is likely less significant due to the axial loads peaking at rated wind speeds and declining as the wind speed increases further.

5.4 Summary and Discussion

This chapter utilised the numerical model developed in the previous chapter and a vast set of new simulated hub-loading data to perform two studies to explore the effects of wind flow conditions on tapered roller main bearing behaviour and potential damage. The first study focused on how the bearing unit and individual roller loads change with changing wind field conditions and the second study employed methods presented in [39] to explore the sensitivity of main bearing fatigue life estimates to the turbines operational conditions and inflow wind parameters.

The above sections detailed the extensive set of aeroelastic wind turbine simulations before exploring the minimum, mean and maximum bearing unit loads under the varying inflow wind conditions. The effect of wind shear and turbulence intensity on the load distribution and individual roller loads of both the upwind and downwind rows was then investigated. The bearing unit load study was provided to complete the story started in Chapter 3 where the analytical model was utilised to determine the effects of wind speed, turbulence intensity and shear exponent on bearing loads for a small number of sample hub loading time series. In the current chapter the wind file data set was complete, ranging from cut-in to cut-out mean wind speeds and the numerical model with non-linear stiffness capabilities was utilised to provide more accurate results. The main findings were that the axial loads on the bearing follows that of the turbine thrust curve, the mean and minimum radial loads decrease with increasing wind speed as the max loads increase, and that the mean and maximum moment loads increase with increasing wind speed. The variation of bearing loads around the mean values was reduced with a reduction in turbulence intensity, as expected, while the axial

and radial loads reduced with increasing shear exponent. The moment on the bearing also increased with increasing shear exponent as expected.

While the model was developed to track the roller trajectories around the raceways in order to gauge an accurate understanding of how the roller loads vary as they pass in and out of the loaded region, the rollers were held stationary for this study so the loading regions may be determined. The results provided clear evidence that loads are more equally balanced between the two rows for DTRBs, even in the absence of preload. Interestingly this is completely opposite to the behaviour documented for DSRBs, where the upwind row remains unloaded throughout most of the turbines operational envelope. The moment reacting capability of DTRBs is what sets the two bearing types apart here, not only does the natural decoupling of moment and force reactions help share the loads across the two rows of rollers, but it also helps prevents non-torque loads from being translated downstream to other drivetrain components, potentially improving the operational lifetime of both the main bearing and downstream components, such as the gearbox. It was also found that the bearing was predominantly loaded at opposite ends of the two rows, with the upwind row loaded on the bottom and the downwind row loaded at the top of the bearing irrespective of the wind conditions. The downwind row has less of a loading region but more of a concentration of loads at the top of the bearing due to the axial displacements caused by rotor thrust engaging all of the rollers. This effect also resulted in the mean and maximum loads on the downwind race being less of that that the upwind race throughout all of the wind conditions. The inclusion of axial preload, typically employed in DTRBs, would also engage all of the rollers in the upwind row and the distributed loading may look more similar to that of the downwind row in such an instance. However, axial preload is applied equally to both raceways and so it is likely that there would still be some discrepancy between the roller loads of the two races as the axial displacement resulting from thrust would still inflict more loading on the downwind race.

Increasing the shear exponent was found to increase the mean and maximum loads on the rollers in both races and increase the concentration of loads at the bottom of row

1 and at the top of row 2. The mean wind speed also had a greater effect on the roller loads as the shear exponent of the wind profile increased. It is hypothesised that the loading regions are at opposite sides of the bearing for the two races as the rollers must balance the moment across the bearing. As the wind shear increases, subsequently the moment across the bearing increases overcoming the effects of thrust and so the load regions become more concentrated as the rollers counteract this moment.

The mean loads on the rollers were found to remain mostly unchanged as the turbulence intensity was changed. It was noted that the load regions became more concentrated as the turbulence intensity decreased. These results are counter-intuitive to the findings discussed above as a reduction in turbulence intensity was found to result in a reduction in mean moment magnitudes across the bearing in Figure 5.1. These results highlight the complex interdependence's between the radial, axial and moment loads on the bearing and how they translate through to roller loads.

The limitations of calculating the fatigue life ratings using the developed model was then discussed and the inaccuracies present due to model simplifications and the lack of information on the detailed micro-geometries of the rollers and raceways were highlighted. While the calculated fatigue life ratings don't necessarily represent the expected life of the bearing, it was discussed how the results will provide insight into the differing operational conditions that impact the life of tapered roller bearings. Thus, the results here will be helpful in improving the understanding in the literature of how tapered roller bearings behave as wind turbine main bearings and, in doing so, will help solidify an answer to the research questions proposed in Chapter 2.

The stress riser function was then discussed. The stress riser function is presented in [39] and is used as a first approximation to determine the effects of concentrated edge stresses. However, a logarithmic roller profile is assumed here, which limits the effects of edge stresses, and so a new stress riser function is proposed which assumes equal contact stress effects across the length of the roller. The basic and modified life rating equations from [39] are then discussed and presented before being extended for a tapered roller bearing with two rows.

As the bearing standards fail to present best practice methods for averaging bearing loads and rotational speeds, a method for doing so was then proposed. The proposed method involves utilising Miner's rule, the inclusion of all rotational speed and load data extracted from the simulations, and a probabilistic description of the wind conditions at the turbine site to average the operational conditions of the bearing across the full lifetime of the turbine. The basic fatigue life was then determined using both the standard and proposed stress-riser functions under selected wind conditions and the results were compared. As the standard stress-riser function attempts to estimate the effects of edge loading on rollers (where stresses would be concentrated), the roller laminae at each end of the roller are multiplied by a factor greater than one, increasing the damage occurring at any given roller-raceway contact. The comparison, therefore, resulted in a significantly shorter bearing fatigue life rating when the standard stress riser function was applied. The proposed stress function, which does not alter the roller loads from model calculations, was used for further study in an attempt to more accurately present the logarithmic profiled rollers that are assumed here. It is also important to reiterate that the results presented in this thesis are not indicative of actual bearing fatigue life estimates and instead, the important findings here are how the bearing life is altered under different inflow wind and operational conditions. That being said, a stress-riser function which provides a greater basic fatigue life result will lend itself more readily to a sensitivity analysis, in that greater sensitivities may be uncovered.

A set of base operational conditions involving lubricant type, temperature, turbulence intensity, shear exponent and site mean wind speed were then defined using the modified life rating method. Each of the aforementioned parameters were then varied to approximate the fatigue life sensitivity. The first two results, plotted in Figures 5.10a) and 5.10b), display how the fatigue life rating changes when the lubricant type and operational temperature are operated. Both of these results are very similar as varying the lubricant type and the operational temperature is in fact, altering the viscosity of the lubricant. Moving from the origin across the x-axis in both plots represents a reduction in lubricant viscosity. It is clear then, that a reduction in lubricant viscosity

results in a reduction in fatigue life rating if lubricant condition remains constant. This is due to the reduced probability that sufficient lubricant film thicknesses and, hence, hydrodynamic pressure is generated to fully separate the roller and raceway surfaces when viscosity is decreased.

The remaining plots in Figure 5.10 display how the fatigue life results vary when the wind conditions at the turbine site are altered. The results show that lower turbulence intensity, lower shear exponent of the wind profile, and lower mean wind speeds all result in prolonging the life of the main shaft bearing. The most significant variation in results and, hence, greatest fatigue life sensitivity, is seen when the shear profile of the incoming wind is altered. Increasing the wind shear exponent from the base conditions of 0.2 to 0.4 has a greater detriment to the fatigue life of the bearing than operation at 60 degrees Celsius or increasing the mean wind speed at the turbine site by 50%. These results, again, display a complete contrast in the behaviours of DTRBs and DSRBs as an increase in wind shear exponent was found to increase the fatigue life of DSRBs in [43]. Thus, highlighting the importance of the need to understand the characteristics of DTRB loading during its interaction with the wind field and how one cannot simply expect the same behaviours from DTRBs as found in DSRBs. Considering the findings in the previous chapter, that moment loads on the bearing are the main driver of bearing displacement, provides greater insight into these interesting results. Higher wind shear profile exponents will result in greater wind speed gradients across the swept area of the rotor. The significant difference in thrust loads generated on the blades by the wind speed gradient will result in large moment loads on the blade roots and rotor shaft. These moments are translated through to the main bearing and will result in significant bearing displacements which will increase contact loads and reduce expected fatigue life.

While some fatigue life sensitivities to turbulence intensity were expected, it was not expected to have such a large effect. The mean wind speeds and resulting mean bearing loads should remain consistent among the various turbulence intensities, however, it is hypothesised that fatigue rating variations are determined by the maximum loads

(or deviations from the mean). Larger turbulence intensity values will result in greater deviations from the mean wind speed resulting in both increased and decreased wind speeds. It is thought that the higher wind speeds resulting from the larger fluctuations in the high turbulence files are resulting in greater load magnitudes at the roller-raceway contacts and hence reducing the fatigue life of the bearing. The fatigue life sensitivity to mean wind speeds is shown in Figure 5.10e) where a large decrease in fatigue life is seen when the mean wind speed is increased from 8m/s to 10m/s. This significant reduction in fatigue life can be explained by the increased probability of operation at the knee of the power curve when the mean wind speed is 10m/s. The thrust and moment loads will be greater around the rated wind speed of the turbine, resulting in greater bearing loads and, hence, a reduction in fatigue life. Although the thrust loads on the turbine peak at the rated wind speed, the moment loads on the rotor (and therefore bearing) continue to increase with increasing wind speed. This effect explains why the fatigue life rating continues to drop when the mean wind speed is increased further to 12m/s but does not decline as significantly as the initial increased wind speed.

This chapter utilised the previously derived model to further explore the operational behaviour of tapered roller bearings as wind turbine main bearings and investigated their response to varying operating conditions. Thus, further research was undertaken to build upon an answer to the second research question. The sensitivity study provided an insight to the operational conditions which may be more damaging to tapered roller main shaft bearings and the results of investigations undertaken in the previous chapter proved useful in understanding the results here.

All results in this chapter provide detailed and valuable answers to both research questions 2 and 3.

Chapter 6

Conclusions and Future Work

Wind turbine main shaft bearings have two important functions within the drivetrain system; translating the mechanical torque from the rotor to the gearbox (or generator if direct drive design) and structurally supporting the entirety of the weight of the turbine rotor, hub and main shaft. On top of this, they are designed to react the significant non-torque loads imparted by the rotors interactions with stochastic wind fields to prevent translation through to downstream drivetrain components. As such, throughout the lifetime of a wind turbine, the main shaft bearing operates at varying, but slow, rotational speeds while being subject to continuous and stochastic thrust, radial and moment loads of significant magnitude.

These harsh conditions have led to double-row spherical roller bearings predominantly failing prematurely when supporting wind turbine main shafts. While extensive research campaigns are currently seeking to understand the load behaviours of spherical-roller main bearings, one proposed solution to the premature failures is their direct replacement with tapered-roller bearings. However, the behaviour characteristics of DTRBs as wind turbine main shaft supports remains relatively unexplored. In order to improve the understanding of DTRB load behaviour in this context, this thesis set out to answer the following questions:

1) How may tapered-roller main bearings in wind turbines be modelled simply and effi-

ciently, while retaining key aspects of their load response and stiffness characteristics?

2) Applying such models, what may be concluded about the operating conditions of such components, their load drivers in turbulent wind fields, and their sensitivities in relation to fatigue life ratings?

3) How do load behaviours and sensitivities in tapered-roller main bearings compare to those of spherical-roller main bearings?

An analytical model of a wind turbine drivetrain with a main shaft support representative of a DTRB was developed in Chapter 3 and utilised to explore how the mean and peak radial force and moment loads on the bearing vary with wind speed, wind shear and turbulence intensity. These results were also compared with the same results from an analytical model of the same drivetrain with a support representative of a DSRB. An internal load model of a DTRB was then developed in Chapter 4 and coupled with the analytical DTRB model previously developed. This new model was used to understand the main drivers of the displacement of internal bearing components before assessing the effects of time-varying loads during normal operation on the internal bearing components. Finally, the model was used to explore the bearing unit and roller loads under varying inflow wind conditions for the full operational envelope of the turbine, before an extensive analysis of fatigue rating life sensitivities under varying operational conditions, selected grease, contamination and temperature was undertaken.

With respect to research question 1, findings in this thesis concluded that the inclusion of moment reaction capabilities is crucial for even simplistic representations of DTRBs and a method to estimate stiffness magnitudes was proposed. A methodological approach was also used to develop an efficient internal DTRB load model while retaining critical information for the understanding of bearing behaviour. A method of coupling these two models was then proposed, extending variable stiffness capabilities to the analytical model and allowing the analysis of internal tapered roller response to realistic turbulent wind flow conditions.

With respect to research question 2, the moment loads experienced at the bearing were demonstrated to be the main drivers of internal displacements. Looped loading structures in both forces and moments were also identified under normal operating conditions which may have damaging effects on the bearing. Evidence of consistent roller edge-loading during operation was found in the analyses, and it was demonstrated that the two roller rows are generally loaded at opposite ends of the bearing. Beyond this, a detailed exposition of DTRB internal load conditions and their relationship to turbulent inflow characteristics was undertaken, providing a range of valuable insights. A similarly extensive assessment of fatigue drivers was also generated. Importantly, high levels of fatigue life sensitivity to both operational and lubrication conditions was documented.

With respect to research question 3, the findings in this PhD demonstrate that not only are loading behaviours for DTRBs and DSRBs intrinsically different, but in some cases their response behaviour is exactly opposite. The mean radial force loads were found to remain similar between the two bearing types but the inclusion of moment reacting capabilities in the DTRB significantly reduced the peak force moments experienced. While previous studies have shown DSRBs to be nearly entirely supported by the downwind row, results here demonstrate that both DTRB roller rows share in supporting the bearing loads at all times throughout the full range of operation. Finally, while increases in shear have been shown to increase DSRB fatigue life ratings (due to rotor "lift" effects), the opposite was shown to be true for the DTRB case. These results conclusively demonstrate fundamental differences in DSRB versus DTRB load response. This has important implications regarding whether DTRBs will solve DSRB issues (around roller sliding), since the application of tapered rollers in this context leads to new load response behaviours which may bring with them new issues and associated damage modes. In particular, the dominance of moment loads in wind turbine drivetrains suggests that observed edge-loading tendencies for DTRB rollers may present a problem. The above aspects of the main bearing problem have not been highlighted until now.

With respect to future work, it is recommended that the proposed model be extended to include additional effects such as preload and misalignment. In both cases, detailed technical and in-situ information for such bearings would be required. The model might also be extended to account for turbine bed-plate flexibility or to help understand failure modes from load distributions such as cracking due to edge loading. With regards to internal conditions, an analysis should be performed to determine whether roller friction effects on contact stresses should also be modelled. The model presented here should also be utilised to explore the time-varying loads of individual rollers under a significant number of realistic load cases. With regards to wind inflow, additional effects should be studied, including wind veer and impacts from low-level jets. Transient events, such as emergency stops and start-ups, might also be simulated to asses their impacts on bearing loads. The model presented here could also be integrated with dynamic, multi-body drivetrain models to inform bearing stiffness characteristics. An analysis could also be performed to compare the computation time and roller load magnitudes with other models presented in the literature. Finally, work should be undertaken to analyse optimal frameworks and methodologies for on-boarding medium fidelity drivetrain representations, such as that presented here, within wind farm design workflows and digital twin load impact assessments.

Appendix A

Controller tuning effects on bearing unit loading

A visual investigation of the radial force and moment loads was again completed using the internal bearing model and the aero-elastic hub loading data sets generated in Chapter 5. The same aero-elastic turbine model was used to generate all hub loading data sets presented in this thesis. However, the turbine controller was tuned to a higher standard before the generation of the more comprehensive hub loading data set discussed in Chapter 5. In the interest of continuity, the wind files selected for visual study in this instance have the same second order statistics as the wind files generated in Chapter 4. Therefore, the four wind files studied here have a shear exponent of 0.2, medium turbulence intensity and mean wind speeds of 12, 14, 18 and 24m/s.

The radial force and moment loads on the bearing during the 12 and 14m/s mean wind speed files are plotted on polar axes in Figure A.1. The radial force and moment loads on the bearing during the 18 and 24m/s mean wind speed files are plotted on polar axes in Figure A.2. All plots in this section are presented from the perspective of looking downwind onto the main bearing. The location of 270 degrees for the radial force plots represents a radial force in the downwards direction as would be expected from gravity and a moment plot at the 180 direction indicates the axes in which the moment revolves around. More explicitly, if the moment plot signifies a direction of

180 degrees, it indicates an overturning moment on the rotor.

When comparing the results presented here with the results using the more basic turbine controller in Section 4.5, it is clear that the variation in magnitudes of both radial force and moments has slightly reduced across all of the tested wind files when the tuned controller is utilised. It is also clear that the position of the moment loads have shifted to left and the density plot is more focused around 180 degrees for the tuned controller. The moment plots concentrated around the 180 degrees direction indicates prominent overturning moments throughout most of the example time series. These results display that controller tuning can have a considerable effect on the bearing loads and is likely the reason behind the concentration of loads at rollers in the top position of the downwind row as seen in Section 5.2.2.

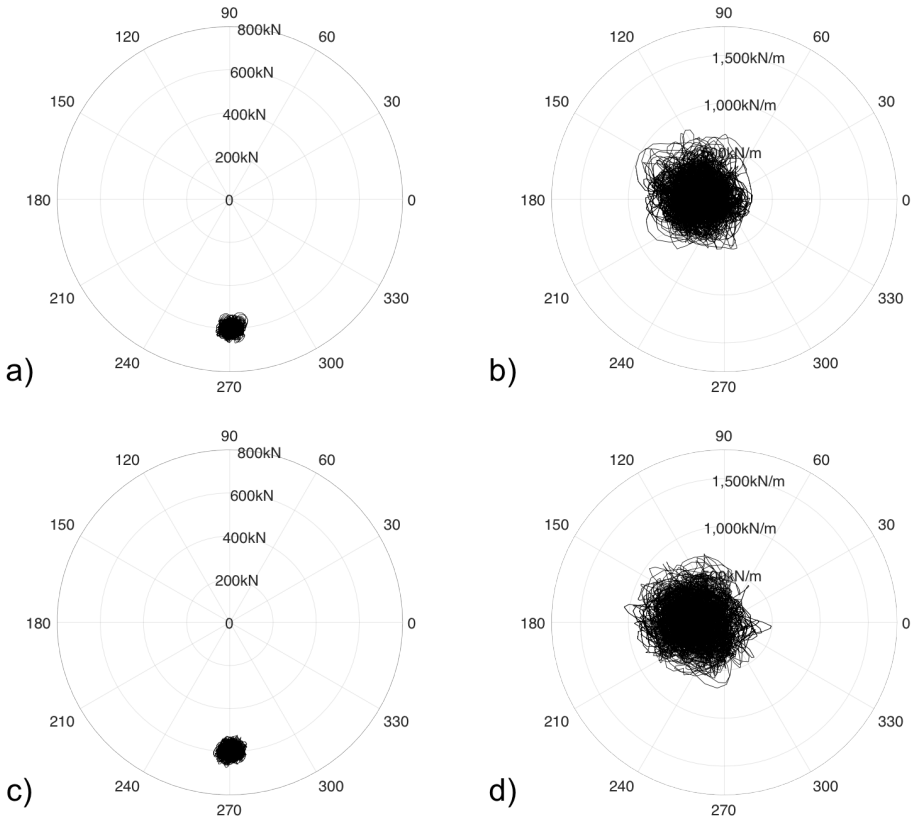

Figure A.1: a) and b) show time series plots of radial force and moment loads for a wind file with mean wind speed of 12m/s, medium turbulence intensity and a shear exponent of 0.2. c) and d) show time series plots of radial force and moment loads for a wind file with mean wind speed of 14m/s, medium turbulence intensity and a shear exponent of 0.2.

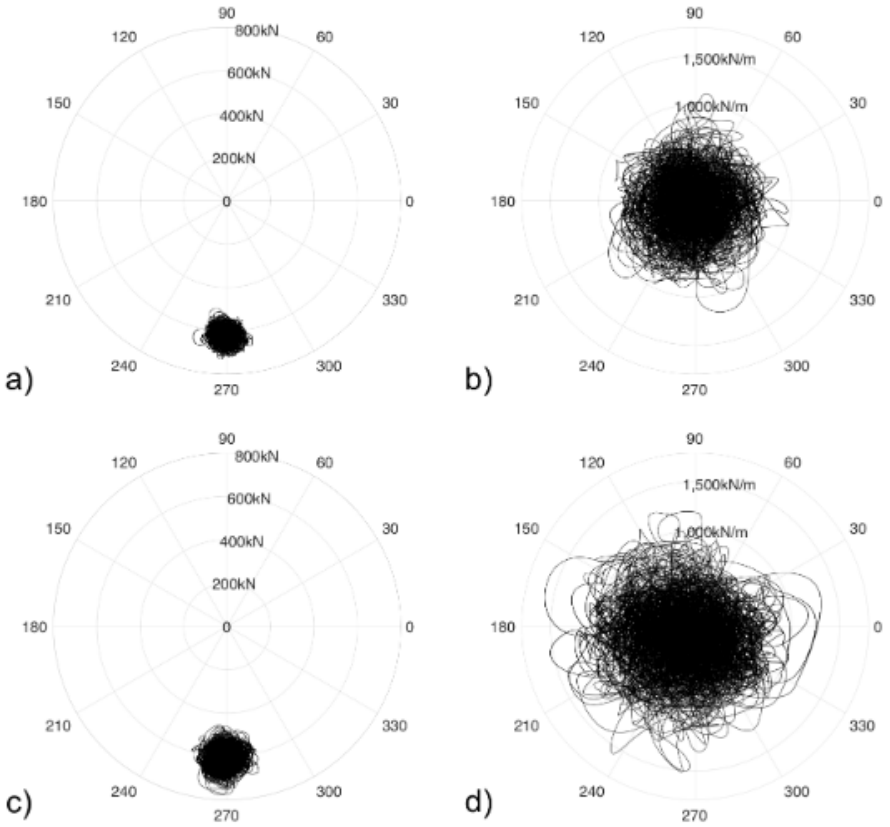

Figure A.2: a) and b) show time series plots of radial force and moment loads for a wind file with mean wind speed of 18m/s, medium turbulence intensity and a shear exponent of 0.2. c) and d) show time series plots of radial force and moment loads for a wind file with mean wind speed of 24m/s, medium turbulence intensity and a shear exponent of 0.2.

Appendix B

Bearing Loads in the Frequency Domain

This section provides a supplementary analysis to the extensive bearing load investigation presented in Chapter 5. The bearing loads are analysed in the frequency domain by taking a fast Fourier transform (FFT) of the time domain signals. This type of analysis identifies the dominant excitations in the bearing reaction loads and can be used to test the new bearing models results as dominant excitations should be deterministic when the turbines operating points and natural modes are known.

Therefore, FFTs were taken of the upwind and downwind inner raceway loads across the wide range of operational conditions outlined in Chapter 5 to explore the dominant excitations on the internal loads of the bearing. As the results for the upwind and downwind rows were similar, only the upwind rows are presented here. The FFT results as the wind shear and turbulence intensity are varied are plotted in Figure B.1a) and Figure B.1b), respectively. The results show peaks at the expected deterministic frequencies with each peak on the two plots labelled appropriately. The 1st peak occurs at the frequency of the rotational speed of the rotor (1P) and the next peak occurs at the blade passing frequency (3P). A small peak then occurs at the 1st blade flap mode frequency, followed by another small peak at a harmonic of the rotational speed/blade passing frequency (6P). A slightly larger peak is then seen at the frequency

of the 1st blade edgewise mode before a final small peak appears at another harmonic of the rotor speed/blade passing frequency (9P). The results in Figure B.1a) show that increasing the shear profile of the wind results in peaks with higher amplitudes while their breadth remains similar. Conversely, the results in Figure B.1b) show that increasing the turbulence intensity increases the overall breadth of each peak while the amplitudes remain similar. The results presented in this section display that the model developed in Chapter 4 is capturing the bearing load response as expected.

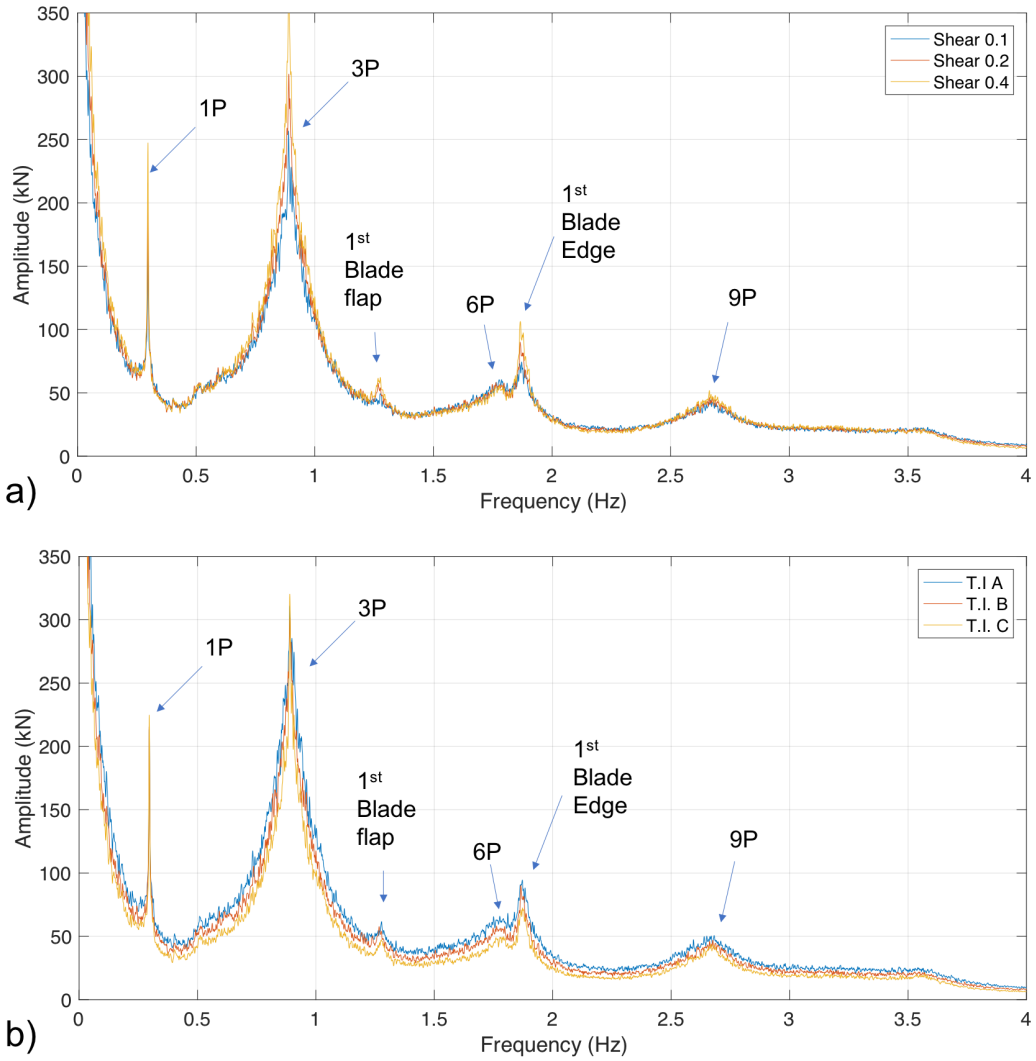

Figure B.1: a) FFT results of the upwind inner race loads under varying shear conditions. b) FFT results of the upwind inner race loads under varying turbulence intensity conditions.

Bibliography

[1] Jesse Agwandas Andrawus. *Maintenance Optimisation for Wind Turbines*. PhD thesis, Robert Gordon University, 2008.

[2] Staffan Andréason. Load distribution in a taper roller bearing arrangement considering misalignment. *Tribology*, 6(3):84–92, 1973. ISSN 00412678. doi: 10.1016/0041-2678(73)90241-8.

[3] Roger Bergua Archeli, Jon Keller, Olle Bankestrom, Mark Dunn, Yi Guo, Alicia Key, Emma Young, Roger Bergua Archeli, Jon Keller, Olle Bankestrom, Mark Dunn, Yi Guo, Alicia Key, and Emma Young. Up-Tower Investigation of Main Bearing Cage Slip and Loads Up-Tower Investigation of Main Bearing Cage Slip and Loads. Technical Report December, National Renewable Energy Laboratory (NREL), 2021. URL `www.nrel.gov/publications.`

[4] A. Baseer, Y. He, R. Schelenz, A. Kari, B. Roscher, and G. Jacobs. Comparison of a Direct Drive Wind Turbine with and without LSS-Coupling Regarding Air Gap Displacement. *Journal of Physics: Conference Series*, 1618(5), 2020. ISSN 17426596. doi: 10.1088/1742-6596/1618/5/052004.

[5] Mattia Beretta, Yolanda Vidal, Jose Sepulveda, Olga Porro, and Jordi Cusidó. Improved Ensemble Learning for Wind Turbine Main Bearing Fault Diagnosis. *Applied Sciences*, 11(16):7523, aug 2021. ISSN 2076-3417. doi: 10.3390/app11167523. URL `https://www.mdpi.com/2076-3417/11/16/7523`.

[6] Roger Bergua, Jordi Jove, and Javier Echarte. Pure torque drivetrain design: A

proven solution for increasing the wind turbine reliability. *Brazil Windpower 2014 conference and exhibition*, (June):15, 2014.

[7] J. Brandlein, P. Eschmann, L. Hasbargen, and K. Weigand. *Ball and Roller Bearings: Theory, Design and Application*. Wiley, Chichester, 3rd editio edition, 1999.

[8] Simon Philippe Breton and Geir Moe. Status, plans and technologies for offshore wind turbines in Europe and North America. *Renewable Energy*, 34(3):646–654, 2009. ISSN 09601481. doi: 10.1016/j.renene.2008.05.040. URL http://dx.doi.org/10.1016/j.renene.2008.05.040.

[9] BSI. Wind energy generation systems - Part 1: Design requirements (IEC 61400-1:2019). Technical Report 1, BSI, 2019. URL http://dx.doi.org/10.1016/j.tej.2017.07.002%250Ahttps://doi.org/10.1016/j.seta.2020.100852%250Ahttps://doi.org/10.1016/j.renene.2019.05.058%250Ahttp://www.wind-power-program.com/Library/Reportsonthenaturalwind/Small-scaleWindEnergy-TechnicalReport.

[10] Tony Burton, Nick Jenkins, David Sharpe, and Ervin Bossanyi. *Wind Energy Handbook*. John Wiley & Sons, Ltd, Chichester, UK, may 2011. ISBN 9781119992714. doi: 10.1002/9781119992714. URL http://doi.wiley.com/10.1002/9781119992714.

[11] Caleb Chovan and Anthony J Fierro. Improving bearing life in wind turbine main shafts and gearboxes. Technical report, Timken, 2021.

[12] J. Coultate. Wind turbine drivetrain technology and cost drivers. Technical report, Romax Technology, 2011.

[13] Elisha De Mello, Georgios Kampolis, Edward Hart, Daryl Hickey, Iain Dinwoodie, James Carroll, Rob Dwyer-Joyce, and Ampea Boateng. Data driven case study of a wind turbine main-bearing failure. *Journal of Physics: Conference Series*, 2018 (1):12011, 2021. ISSN 17426596. doi: 10.1088/1742-6596/2018/1/012011.

[14] Elisha de Mello, Edward Hart, Yi Guo, Jonathan Keller, Rob Dwyer-Joyce, and

Ampea Boateng. Dynamic modelling of slip in a wind turbine spherical roller main bearing. *Forschung im Ingenieurwesen*, 87(1):297–307, mar 2023. ISSN 0015-7899. doi: 10.1007/s10010-023-00652-z. URL https://link.springer.com/10.1007/s10010-023-00652-z.

[15] D Dowson. Elastohydrodynamic and micro-elastohydrodynamic lubrication. *Wear*, 190:125–138, 1995.

[16] Roberto Fernandez Martinez, Ruben Lostado Lorza, Ana A. Santos Delgado, and Nelson O. Piedra Pullaguari. Optimizing presetting attributes by softcomputing techniques to improve tapered roller bearings working conditions. *Advances in Engineering Software*, 123(February):13–24, 2018. ISSN 18735339. doi: 10.1016/j.advengsoft.2018.05.005. URL https://doi.org/10.1016/j.advengsoft.2018.05.005.

[17] Evan Gaertner, Jennifer Rinker, Latha Sethuraman, Frederik Zahle, Benjamin Anderson, Garrett E. Barter, Nikhar J. Abbas, Fanzhong Meng, Pietro Bortolotti, Witold Skrzypinski, George N. Scott, Roland Feil, Henrik Bredmose, Katherine Dykes, Matthew Shields, Christopher Allen, and Anthony Viselli. IEA Wind TCP Task 37: Definition of the IEA 15-Megawatt Offshore Reference Wind Turbine. Technical report, National Renewable Energy Laboratory, 2020. URL www.nrel.gov/publications.https://www.osti.gov/biblio/1603478%0Ahttps://www.osti.gov/servlets/purl/1603478.

[18] Irving P. Girsang, Jaspreet S. Dhupia, Eduard Muljadi, Mohit Singh, and Lucy Y. Pao. Gearbox and drivetrain models to study dynamic effects of modern wind turbines. *IEEE Transactions on Industry Applications*, 50(6):3777–3786, 2014. ISSN 00939994. doi: 10.1109/TIA.2014.2321029.

[19] GOV.UK. Contracts for Difference Allocation Round 3 Results, 2019. URL https://www.gov.uk/government/publications/contracts-for-difference-cfd-allocation-round-3-results/contracts-for-difference-cfd-allocation-round-3-results.

[20] Y. Guo, T. Parsons, K. Dykes, and R.N. King. A systems engineering analysis of three-point and four-point wind turbine drivetrain configurations. *Wind Energy*, 20(3):537–550, mar 2017. ISSN 10954244. doi: 10.1002/we. URL `http://doi.wiley.com/10.1002/we.2022`.

[21] Yi Guo, Roger Bergua, Jeroen van Dam, Jordi Jove, and Jon Campbell. Improving Wind Turbine Drivetrain Reliability Using a Combined Experimental, Computational, and Analytical Approach. In *ASME 2014 International Design Engineering Technical Conference*, Buffalo, 2014. doi: 10.1115/detc2014-35169.

[22] Yi Guo, Olle Bankestrom, Roger Bergua, Jonathan Keller, and Mark Dunn. Investigation of main bearing operating conditions in a three-Point mount wind turbine drivetrain. *Forschung im Ingenieurwesen/Engineering Research*, 85(2):405–415, 2021. ISSN 14340860. doi: 10.1007/s10010-021-00477-8.

[23] Yi Guo, Allan Thomson, Roger Bergua, Joe Erskine, Jonathan Keller, Yi Guo, Allan Thomson, Roger Bergua, Joe Erskine, and Jonathan Keller. Acoustic Emission Measurement of a Wind Turbine Main Bearing Acoustic Emission Measurement of a Wind Turbine Main Bearing. Technical Report October, National Renewable Energy Laboratory, 2022. URL `www.nrel.gov/publications.`

[24] K Gurumoorthy and Arindam Ghosh. Case Studies in Engineering Failure Analysis Failure investigation of a taper roller bearing : A case study. *Biochemical Pharmacology*, 1(2):110–114, 2013. ISSN 2213-2902. doi: 10.1016/j.csefa.2013.05.002. URL `http://dx.doi.org/10.1016/j.csefa.2013.05.002`.

[25] J. Halme and P. Andersson. Rolling contact fatigue and wear fundamentals for rolling bearing diagnostics - State of the art. *Proceedings of the Institution of Mechanical Engineers, Part J: Journal of Engineering Tribology*, 224(4):377–393, 2010. ISSN 13506501. doi: 10.1243/13506501JET656.

[26] Tedric A. Harris. *Essential Concepts of Bearing Technology, FIFTH EDITION*. CRC Press, oct 2006. ISBN 9781420006599. doi: 10.1201/9781420006599. URL `https://www.taylorfrancis.com/books/9781420006599`.

[27] E Hart. *Wind turbine dynamics identification using Gaussian process machine learning*. PhD thesis, University of Strahclyde, 2018.

[28] Edward Hart. Developing a systematic approach to the analysis of time-varying main bearing loads for wind turbines. *Wind Energy*, (February):1–16, 2020. ISSN 10991824. doi: 10.1002/we.2549.

[29] Edward Hart, Alan Turnbull, Julian Feuchtwang, David McMillan, Evgenia Golysheva, and Robin Elliott. Wind turbine mainbearing loading and wind field characteristics. *Wind Energy*, 22(11):1534–1547, nov 2019. ISSN 1095-4244. doi: 10.1002/we.2386. URL `https://onlinelibrary.wiley.com/doi/abs/10.1002/we.2386`.

[30] Edward Hart, Benjamin Clarke, Gary Nicholas, Abbas Kazemi Amiri, James Stirling, James Carroll, Rob Dwyer-Joyce, Alasdair McDonald, and Hui Long. A review of wind turbine main bearings: Design, operation, modelling, damage mechanisms and fault detection, 2020. ISSN 23667451. URL `https://doi.org/10.5194/wes-5-105-2020`.

[31] Edward Hart, Elisha De Mello, and Rob Dwyer-Joyce. Wind turbine main-bearing lubrication - Part 2: Simulation-based results for a double-row spherical roller main bearing in a 1.5MW wind turbine. *Wind Energy Science*, 7(4):1533–1550, 2022. ISSN 23667451. doi: 10.5194/wes-7-1533-2022.

[32] Edward Hart, Adam Stock, George Elderfield, Robin Elliott, James Brasseur, Jonathan Keller, Yi Guo, and Wooyong Song. Impacts of wind field characteristics and non-steady deterministic wind events on time-varying main-bearing loads. *Wind Energy Science*, 7(3):1209–1226, 2022. ISSN 23667451. doi: 10.5194/wes-7-1209-2022.

[33] Zhenzhi He, Xiaodong Xu, Minghui Shao, and Jinhe Wu. Analysis of contact characteristics of tapered roller bearing with crowned rollers. In *AIP Conference Proceedings*, volume 1890, page 40061, 2017. ISBN 9780735415683. doi: 10.1063/1.5005263. URL `https://doi.org/10.1063/1.5005263`.

[34] R.C Hibbeler. *Structural Analysis*. Pearson Education, 2011.

[35] L. Houpert. A uniform analytical approach for ball and roller bearings calculations. *Journal of Tribology*, 119(4):851–858, 1997. ISSN 15288897. doi: 10.1115/1.2833896.

[36] IEC. Wind turbines Part 1: Design requirements. Technical report, IEC, 2005.

[37] L. Ionescu and T. Pontius. Main Shaft Support For Wind Turbine with a Fixed and Floating Bearing Configuration Tapered Double Inner Row Bearing Vs. Spherical Roller Bearing on The Fixed Position. Technical report, Timken, 2009.

[38] ISO. ISO 281:2007 Rolling Bearings - Dynamic load ratings and rating life. Technical report, International Organization of Standards, 2007.

[39] ISO. DD ISO/TS 16281:2008 Rolling bearings Methods for calculating the modified reference rating life for universally loaded bearings. Technical report, International Organization of Standards, 2009. URL `www.sis.se`.

[40] A. Gilbert K. Leet, C. Uang. *Fundamentals of Structural Analysis*. McGraw Hill, 2011.

[41] Simon Kabus, Michael R Hansen, and Ole Ø Mouritsen. A New Quasi-Static Cylindrical Roller Bearing Model to Accurately Consider Non-Hertzian Contact Pressure in Time Domain Simulations. *Journal of Tribology*, 134(4), oct 2012. ISSN 0742-4787. doi: 10.1115/1.4007219. URL `http://asmedigitalcollection.asme.org/tribology/article-pdf/134/4/041401/5603390/041401_1.pdfhttps://asmedigitalcollection.asme.org/tribology/article/doi/10.1115/1.4007219/436478/A-New-QuasiStatic-Cylindrical-Roller-Bearing-Model`.

[42] J Keller, S Sheng, A Cottrell, and A Greco. Wind Turbine Drivetrain Seminar Reliability Tribology Collaborative: A Recap. Technical Report August, National Renewable Energy Laboratory, 2016.

[43] Jarred Kenworthy, Edward Hart, James Stirling, Adam Stock, Jonathan Keller,

Guo James, and Brasseur Rhys. Wind turbine main bearing rating-lives as determined by IEC 61400-1 : 2019 and ISO 281 : 2007. *Not yet submitted*, pages 1–14, 2023.

[44] S Kock, G Jacobs, and D Bosse. Determination of Wind Turbine Main Bearing Load Distribution. *Journal of Physics: Conference Series*, 1222(1), may 2019. ISSN 1742-6588. doi: 10.1088/1742-6596/1222/1/012030. URL `https://iopscience.iop.org/article/10.1088/1742-6596/1222/1/012030`.

[45] Michael N. Kotzalas and Gary L. Doll. Tribological advancements for reliable wind turbine performance, oct 2010. ISSN 1364503X.

[46] J. Lee and F. Zhao. Global Wind Report 2021. Technical report, Global Wind Energy Council, 2021. URL `http://www.gwec.net/global-figures/wind-energy-global-status/`.

[47] Amin Loriemi, Georg Jacobs, Sebastian Reisch, Dennis Bosse, and Tim Schröder. Experimental and simulation-based analysis of asymmetrical spherical roller bearings as main bearings for wind turbines. *Forschung im Ingenieurwesen/Engineering Research*, 85(2):189–197, jun 2021. ISSN 14340860. doi: 10.1007/S10010-021-00462-1.

[48] Ruben Lostado, Roberto Fernandez Martinez, and Bryan J. Mac Donald. Determination of the contact stresses in double-row tapered roller bearings using the finite element method, experimental analysis and analytical models. *Journal of Mechanical Science and Technology 2015 29:11*, 29(11):4645–4656, dec 2015. ISSN 1976-3824. doi: 10.1007/S12206-015-1010-4. URL `https://link-springer-com.proxy.lib.strath.ac.uk/article/10.1007/s12206-015-1010-4`.

[49] Amir R. Nejad and Jone Torsvik. Drivetrains on floating offshore wind turbines: lessons learned over the last 10 years. *Forschung im Ingenieurwesen/Engineering Research*, 85(2):335–343, 2021. ISSN 14340860. doi: 10.1007/s10010-021-00469-8.

[50] Amir R Nejad, Jonathan Keller, Yi Guo, Shawn Sheng, Henk Polinder, Simon Watson, Jianning Dong, Zian Qin, Amir Ebrahimi, Ralf Schelenz, Francisco Gutiérrez

Guzmán, Daniel Cornel, Reza Golafshan, Georg Jacobs, Bart Blockmans, Jelle Bosmans, Bert Pluymers, James Carroll, Sofia Koukoura, Edward Hart, Alasdair McDonald, Anand Natarajan, Jone Torsvik, Farid K. Moghadam, Pieter-Jan Daems, Timothy Verstraeten, Cédric Peeters, and Jan Helsen. Wind turbine drivetrains: state-of-the-art technologies and future development trends. *Wind Energy Science*, 7(1):387–411, feb 2022. ISSN 2366-7451. doi: 10.5194/wes-7-387-2022. URL `https://wes.copernicus.org/articles/7/387/2022/`.

[51] Amir Rasekhi Nejad, Zhiyu Jiang, Zhen Gao, and Torgeir Moan. Drivetrain load effects in a 5-MW bottom-fixed wind turbine under blade-pitch fault condition and emergency shutdown. In *Journal of Physics: Conference Series*, volume 753, 2016. doi: 10.1088/1742-6596/753/11/112011.

[52] Henk Polinder, Frank F.A. Van Der Pijl, Gert Jan De Vilder, and Peter J. Tavner. Comparison of direct-drive and geared generator concepts for wind turbines. *IEEE Transactions on Energy Conversion*, 21(3):725–733, 2006. ISSN 08858969. doi: 10.1109/TEC.2006.875476.

[53] Egor P. Popov. *Engineering Mechanics of solids*. Prentice-Hall Inc., 1990.

[54] Amir Rasekhi Nejad, Yihan Xing, and Torgeir Moan. Gear Train Internal Dynamics in Large Offshore Wind Turbines. In *Volume 3: Advanced Composite Materials and Processing; Robotics; Information Management and PLM; Design Engineering*, number 1, pages 823–831. American Society of Mechanical Engineers, jul 2012. ISBN 978-0-7918-4486-1. doi: 10.1115/ESDA2012-83004. URL `https://asmedigitalcollection.asme.org/ESDA/proceedings/ESDA2012/44861/823/231531`.

[55] REN21. Renewables 2021 Global Status Report. Technical report, REN21, Paris, 2021.

[56] Amadeus Rolink, Tim Schröder, Georg Jacobs, Dennis Bosse, Johannes Hölzl, and Philipp Bergmann. Feasibility study for the use of hydrodynamic plain bearings with balancing support characteristics as main bearing in wind turbines. *Journal*

of Physics: Conference Series, 1618(5), 2020. ISSN 17426596. doi: 10.1088/1742-6596/1618/5/052002.

[57] Amadeus Rolink, Georg Jacobs, Tim Schröder, Dennis Keller, Timm Jakobs, Dennis Bosse, Jochen Lang, and Gunter Knoll. Methodology for the systematic design of conical plain bearings for use as main bearings in wind turbines. *Forschung im Ingenieurwesen/Engineering Research*, 85(2):629–637, 2021. ISSN 14340860. doi: 10.1007/s10010-021-00452-3.

[58] Tim Schröder, Georg Jacobs, Amadeus Rolink, and Dennis Bosse. "flexPad" - Innovative conical sliding bearing for the main shaft of wind turbines. *Journal of Physics: Conference Series*, 1222(1), 2019. ISSN 17426596. doi: 10.1088/1742-6596/1222/1/012026.

[59] Latha Sethuraman, Yi Guo, and Shuangwen Sheng. Main Bearing Dynamics in Three-Point Suspension Drivetrains for Wind Turbines. *American wind energy association windpower*, pages 18–21, 2015.

[60] Latha Sethuraman, Yihan Xing, Vengatesan Venugopal, Zhen Gao, Markus Mueller, and Torgeir Moan. A 5 MW direct-drive generator for floating spar-buoy wind turbine: Drive-train dynamics. *Proceedings of the Institution of Mechanical Engineers, Part C: Journal of Mechanical Engineering Science*, 231(4):744–763, feb 2017. ISSN 20412983. doi: 10.1177/0954406215623306. URL `http://journals.sagepub.com/doi/10.1177/0954406215623306`.

[61] SKF. Rolling bearings. Technical report, SKF, 2018. URL `skf.com/go/17000`.

[62] Joshua Smalley. Turbine components: bearings, 2015. URL `http://www.windpowerengineering.com/design/mechanical/turbine-components-bearings-brakes-generators-hydraulics-seals-towers/`.

[63] Johan N. Stander, Gerhard Venter, and Maarten J. Kamper. Review of direct-drive radial flux wind turbine generator mechanical design. *Wind Energy*, 15(3):459–472, apr 2012. ISSN 10954244. doi: 10.1002/we.484. URL `https://onlinelibrary.wiley.com/doi/10.1002/we.484`.

[64] Ewoud Stehouwer and Gerrit Jan van Zinderen. Conceptual nacelle designs of 10-20 MW wind turbines. Technical report, Innwind, 2016.

[65] Yun-Shuai Su, Shu-Rong Yu, Shu-Xin Li, and Yan-Ni He. Review of the damage mechanism in wind turbine gearbox bearings under rolling contact fatigue. *Frontiers of Mechanical Engineering*, pages 1–8, dec 2017. ISSN 2095-0233. doi: 10.1007/s11465-018-0474-1. URL `http://link.springer.com/10.1007/s11465-018-0474-1`.

[66] I Sugiura, S Ito, N Tsushima, and H Muro. Investigation of Optimum Crowning in a Line Contact Cylinder-to-Cylinder Rolling Contact Fatigue Test Rig. *Rolling Contact Fatigue Testing of Bearing Steels*, pages 136–136–14, mar 2009. doi: 10.1520/STP36137S.

[67] Elon J. Terrell, William M. Needelman, and Jonathan P. Kyle. Wind turbine tribology. In *Green Energy and Technology*, chapter 18, pages 483–530. Springer-Verlag, Berlin, 2012. ISBN 9783642236808. doi: 10.1007/978-3-642-23681-5.

[68] Roman Teutsch and Bernd Sauer. An Alternative Slicing Technique to Consider Pressure Concentrations in Non-Hertzian Line Contacts. *Journal of Tribology*, 126(3):436–442, jul 2004. ISSN 0742-4787. doi: 10.1115/1.1739244. URL `https://asmedigitalcollection-asme-org.proxy.lib.strath.ac.uk/tribology/article/126/3/436/464310/An-Alternative-Slicing-Technique-to-Consider`.

[69] Patrick A. Tibbits. Fem simulation and life optimization of tandem roller thrust bearing. *Proceedings of the ASME International Design Engineering Technical Conferences and Computers and Information in Engineering Conference - DETC2005*, 3 A(December):79–88, 2005. doi: 10.1115/detc2005-84234.

[70] Timken, Brüel & Kjær Vibro, and Delom. Wind Turbine Common Failures and Solutions. *Wind O&M Canada 2017*, pages 1–8, 2017.

[71] Van Canh Tong and Seong Wook Hong. Characteristics of tapered roller bearing subjected to combined radial and moment loads. *International Journal*

of Precision Engineering and Manufacturing-Green Technology 2014 1:4, 1(4): 323–328, oct 2014. ISSN 2198-0810. doi: 10.1007/S40684-014-0040-1. URL https://link.springer.com/article/10.1007/s40684-014-0040-1.

[72] Van Canh Tong and Seong Wook Hong. Fatigue life of tapered roller bearing subject to angular misalignment. *Proceedings of the Institution of Mechanical Engineers, Part C: Journal of Mechanical Engineering Science*, 230(2):147–158, 2016. ISSN 20412983. doi: 10.1177/0954406215578706.

[73] Van Canh Tong and Seong Wook Hong. Optimization of partially crowned roller profiles for tapered roller bearings. *Journal of Mechanical Science and Technology 2017 31:2*, 31(2):641–650, feb 2017. ISSN 1976-3824. doi: 10.1007/S12206-017-0117-1. URL https://link-springer-com.proxy.lib.strath.ac.uk/article/10.1007/s12206-017-0117-1.

[74] Bo Torstenfelt and Billy Fredriksson. Pressure distribution in crowned roller contacts. *Engineering Analysis*, 1(1):32–39, 1984. ISSN 0264682X. doi: 10.1016/0264-682X(84)90007-8.

[75] Shuaishuai Wang, Amir R. Nejad, Erin E. Bachynski, and Torgeir Moan. Effects of bedplate flexibility on drivetrain dynamics: Case study of a 10 MW spar type floating wind turbine. *Renewable Energy*, 161:808–824, dec 2020. ISSN 18790682. doi: 10.1016/j.renene.2020.07.148. URL https://linkinghub.elsevier.com/retrieve/pii/S0960148120312246.

[76] Shuaishuai Wang, Amir R. Nejad, and Torgeir Moan. On design, modelling, and analysis of a 10-MW medium-speed drivetrain for offshore wind turbines. *Wind Energy*, 23(4):1099–1117, apr 2020. ISSN 10991824. doi: 10.1002/we.2476. URL https://onlinelibrary.wiley.com/doi/abs/10.1002/we.2476.

[77] Shuaishuai Wang, Amir Nejad, Erin E. Bachynski, and Torgeir Moan. A comparative study on the dynamic behaviour of 10 MW conventional and compact gearboxes for offshore wind turbines. *Wind Energy*, 24(7):770–789, 2021. ISSN 10991824. doi: 10.1002/we.2602.

[78] Tengfei Xu, Lihua Yang, and Yao Wu. Friction torque study on double-row tapered roller bearing. *I2MTC 2019 - 2019 IEEE International Instrumentation and Measurement Technology Conference, Proceedings*, 2019-May, 2019. doi: 10.1109/I2MTC.2019.8827169.

[79] Souichi Yagi. Bearings for Wind Turbine. *NTN Technical review*, 71(71):40–47, 2004.

[80] Henghai Zhang, Wenku Shi, Guozheng Liu, and Zhiyong Chen. A Method to Solve the Stiffness of Double-Row Tapered Roller Bearing, 2019. ISSN 15635147.

[81] Jingyang Zheng, Jinchen Ji, Shan Yin, and Van-Canh Tong. Internal loads and contact pressure distributions on the main shaft bearing in a modern gearless wind turbine. *Tribology International*, 141:105960, jan 2020. ISSN 0301679X. doi: 10.1016/j.triboint.2019.105960. URL `https://linkinghub.elsevier.com/retrieve/pii/S0301679X19304797`.

[82] Jingyang Zheng, Jinchen Ji, Shan Yin, and Van Canh Tong. Fatigue life analysis of double-row tapered roller bearing in a modern wind turbine under oscillating external load and speed. *Proceedings of the Institution of Mechanical Engineers, Part C: Journal of Mechanical Engineering Science*, 234(15):3116–3130, 2020. ISSN 20412983. doi: 10.1177/0954406220911966.